Title
Electron-Lattice Dynamics of Solid-State Materials Relevant for Solar Energy Conversion Studied by Femtosecond Extreme Ultraviolet Absorption Spectroscopy

Author
Carneiro, Lucas Machado

Publication Date
2018

Peer reviewed|Thesis/dissertation

Electron-Lattice Dynamics of Solid-State Materials Relevant for Solar Energy Conversion Studied by Femtosecond Extreme Ultraviolet Absorption Spectroscopy

By

Lucas Machado Carneiro

A dissertation submitted in partial satisfaction of the

requirements for the degree of

Doctor of Philosophy

in

Chemistry

in the

Graduate Division

of the

University of California, Berkeley

Committee in charge:

Professor Stephen R. Leone, Chair

Professor Richard J. Saykally

Professor James G. Analytis

Fall 2018

Electron-Lattice Dynamics of Solid-State Materials Relevant for Solar Energy Conversion Studied by Femtosecond Extreme Ultraviolet Absorption Spectroscopy

Lucas Machado Carneiro

Abstract

Electron-Lattice Dynamics of Solid-State Materials Relevant for Solar Energy Conversion Studied by Femtosecond Extreme Ultraviolet Absorption Spectroscopy

by

Lucas Machado Carneiro

Doctor of Philosophy in Chemistry

University of California, Berkeley

Professor Stephen R. Leone, Chair

For many decades, electron dynamics and lattice dynamics have been studied by performing separate experiments, requiring different instrumentation. In general, electronic dynamics are most often studied by using visible pump probe spectroscopy, while lattice dynamics can be followed by core level spectroscopy performed at synchrotrons. With the advent of high harmonic generation (HHG), it became possible to generate femtosecond to attosecond bursts of extreme ultraviolet (XUV) radiation that are both spatially and temporally coherent. Since high harmonic generation can be performed on a table-top setup, it has become possible to follow both electronic and lattice dynamics concurrently, without the need for a synchrotron. In this dissertation, visible pump-XUV probe transient absorption spectroscopy is used to elucidate the excited state electronic and lattice dynamics of two materials relevant for solar energy conversion, namely α-Fe_2O_3 and single crystalline Si thin films.

In this dissertation, the first chapter deals with the pertinent information necessary to understand both the core-level spectroscopy that can be used to glean information about the electronic and lattice dynamics of solids, and the solid-state physics which govern the electronic and lattice dynamics, with special focus on the theoretical models used in these fields. The second chapter outlines the experimental apparatus that is used to perform the pump probe experiments on solid state samples, as well as several upgrades made to it during the course of this thesis. The third chapter details experiments performed on α-Fe_2O_3 that provide insights into its excited state dynamics following photoexcitation by multiple pump wavelengths (400 nm, 480 nm, 520 nm, 560 nm), including polaron formation and its impact on the photoconversion efficiency of photoelectrochemical cells. The fourth chapter details experiments performed on single crystalline Si thin films following photoexcitation with 800 nm pump pulses. This experiment highlights the strengths of HHG pump probe spectroscopy by giving insights into the electron-phonon scattering mechanisms that follow photoexcitation across the bandgap.

To my family

List of Figures

List of Tables

Acknowledgements

First and foremost, I would like to express my deepest gratitude to my advisor, Professor Stephen Leone. Throughout my time at Berkeley, I found that his dedication to his students' success was unparalleled, as far as I could gather from conversations with my colleagues in other research groups. Without his financial, scientific, and personal support, I would not have succeeded in accomplishing the work performed herein. He believed that I could succeed even when I didn't, and was patient when I struggled. His dedication to scientific truth and rigor resonates very strongly with me, and was a source of inspiration to become a better scientist. Also, thank you, Chang-Ming for being my mentor and entrusting me the apparatus you built.

I have met many people throughout my time at Berkeley, but being extremely introverted, I struggled to maintain friendships. Especially after I experienced significant trauma, leading to severe depression, after which I became completely alone. To all those who I slowly lost touch with, I hope we can rekindle our friendships soon. Throughout it all, however, I could always count on the support of my dear friend, Desiré Whitmore, who recruited me into the Leone group 5 years ago, and who today I consider family. I am not sure she understands how important she is to me or the countless other people who she supports and encourages every day (in fact, I know she doesn't!), but without exaggeration I can say that if not for her, I might not be here today to write these words. Her selflessness, empathy, positivity, and vigor for life are something to be admired and aspire towards. For supporting me in every possible way (literally, it is pointless to even try to list them), thank you from the bottom of my heart. I'll be with you, when the deal goes down.

I must also thank my dear friend and group member Natalie Gibson. We went through all the ups and downs of grad school, and life in general, together these past 5 years. You were the only friend here who didn't completely give up on me during my depression. Your loyalty and kindness was unexpected but extremely appreciated.

I would also like to thank my entire family for always supporting me, and being patient with me, when I was silent. Nick and Daniel, you are too young today, but one day I hope you can understand how much I love you both and how important you were to my success. The completion of this Ph.D. was in large part so that you could one day know that even in your darkest hour, you should never give up. Remember that if you're going through Hell, *keep going*. I will always be here for you. Pai, obrigado pelo apoio durante tudo isso. Apoio moral, financeiro, emocional. Saiba que eu aprecio tudo profundamente. Obrigado por ter amadurecido ao longo da minha vida, e por sempre ter se preocupado comigo. Muitos pais não ligam pros seus filhos. Eu sei que eu não sou o filho mais fácil com quem se conviver, então obrigado. Eu te amo. Maria, obrigado por ter me apoiado também. As suas vitórias na vida são extremamente inspiradoras, não só pra mim, mas pra todos que acabam lhe conhecendo, força sempre. Rodrigo, você é o meu mais velho e melhor amigo. Dois truta, mil treta. A nossa amizade não cabe aqui, talvez tenhamos que escrever um livro um dia. Mãe, obrigado pelo amor incondicional. Muito na vida é incerto, mas o seu amor por mim não. Sem você eu não teria chegado aqui também.

Chapter 1

Introduction

With the invention of the internal combustion engine came the industrial evolution, and humans have relied on fossil fuels to power the economy and their homes ever since. Unfortunately, not only is this resource finite, its unmitigated consumption has led to potentially dangerous anthropogenic climate change[1–3]. However, with the advent of quantum mechanics, humans are now poised to efficiently harness the energy of the Sun instead, either by converting sunlight directly into usable electricity, as in the case of photovoltaics (PVs), or by splitting water in order to store the energy in the form of $H_{2(g)}$, as in the case of photoelectrochemical cells (PECs). In the case of PVs, crystalline silicon has long been used due to its high photon to electron conversion efficiency[4], but nearly all of the silicon on Earth is found in its oxidized form, SiO_2. Unfortunately, the Si-O bond is so strong that unlocking the Si can become fairly expensive[5,6]. In the case of PECs, most candidate materials are also fairly expensive, or suffer from corrosion issues due to contact with water[7–9]. Thus, it is highly desirable to find an alternative material, or set of materials, that can be used instead, but with comparable or better conversion efficiencies and high stability. Towards this effort, many solar cell architectures have been developed, with an increasing focus on nanostructuring and multi-junction cells.

In order to intelligently design efficient solar cells, it is important to understand the fundamental physics that drives solar energy conversion. Several parameters determine the conversion efficiency of solar cells, energy carrier transport and recombination being key ones. However, since the energy carriers can interact both amongst themselves and with the crystalline lattice at timescales spanning several orders of magnitude (10^{-18} s – 10^{-6} s), fully understanding the energy carrier dynamics has been challenging, to say the least. With the advent of the laser, especially pulsed lasers, many time-resolved techniques have been devised to study these dynamics, the most prominent among them being pump-probe spectroscopy.

For the most part, both the pump and probe pulses have been in the visible or infrared range since these energies are accessible with commercial laser systems. Since this photon energy range can only probe the valence electronic structure (VES), it is difficult to distinguish between the electronic and the lattice dynamics that contribute to the transient signals. On the other hand, synchrotron radiation has long been used in core-level spectroscopy to probe the structural dynamics of solids. For example, transient electron and x-ray diffraction experiments allow for direct measurements of the lattice dynamics following photoexcitation[10–12], but the electronic contribution must often be inferred. With the development of high harmonic generation (HHG) in the late 80s[13,14], it became possible to generate laser pulses in the extreme ultraviolet (XUV) energy range with femtosecond to attosecond time resolution on a table top setup. Thus, it became possible

to combine the strengths of ultrafast pump-probe spectroscopy with those of core-level spectroscopy, using commercial laser systems. In this thesis, tunable visible pump, broadband XUV probe spectroscopy is used to elucidate the ultrafast electronic and lattice dynamics of materials relevant for solar energy conversion.

This chapter details the aspects of both x-ray absorption spectroscopy as well as solid-state physics that are important to the work performed in this thesis. The first subsection deals with x-ray absorption spectroscopy and how it can be used to understand solid-state dynamics in solids. The next section deals with carrier and lattice interactions. The last section discusses high harmonic generation.

1.1 Core Level Spectroscopy of Solids

1.1.1 Advantages of Transient Core Level Spectroscopy

Although single junction crystalline silicon solar cells already operate close to their theoretical Shockley-Queisser efficiency limit[4,15], it would be beneficial to either push past this limit, by using multijunction configurations[16,17] or multiple carrier generation[18], or to use an absorbing material with comparable efficiency that is much cheaper to produce. Unfortunately, no other single material has been shown to be comparable to Si in terms of efficiency versus cost. The increased complexity in these cases requires precise control of carrier relaxation and transport properties, which are mediated by carrier-carrier, carrier-phonon and phonon-phonon scattering processes. Since these processes occur across a wide range of timescales and energy ranges, studying them generally requires different techniques involving multiple types of instrumentation. This quickly becomes both time and cost prohibitive. For example, carrier-carrier scattering has been studied with several pump probe methods such as infrared to visible transient absorption[18], time-resolved two-photon photoemission[19], and terahertz spectroscopy[20]. As for the carrier-phonon interactions following photoexcitation, they have been studied by directly measuring the lattice dynamics through transient electron and x-ray diffraction[10–12]. A single table top method to study both carrier and lattice dynamics is thus desirable, and x-ray transient absorption spectroscopy (XTAS) has this unique capability.

The properties of a material are generally determined by their valence electronic structure, since these are the electrons participating in bonding. The core shells of electrons on the other hand are generally isolated and do not participate in bonding. These core electrons are tightly bound to their atomic nucleus and thus behave very similarly whether they are in an isolated atom or, in the extreme case, a solid. Nonetheless, the Coulomb interaction still affects core-electrons and so they are still sensitive to their electronic environment. For example, the binding energy of the 3*p* electron in the first-row transition metals increases monotonically across the row reflecting the increasing nuclear charge of each atom[21]. There is also an observed 1.5 eV blueshift in the L-edge absorption of an element with each increase in oxidation state[22]. This trend is not limited to the L-edge. What was unknown for a long time was whether this trend is also true in the case of excited states of the same compound. This is where the capabilities of ultrafast XTAS become uniquely useful. This technique has been able to show that when Fe_2O_3 is excited with 400 nm light, a charge transfer occurs between the O atom and the Fe atom[23], leading to a change in oxidation state of

Fe^{3+} → Fe^{2+}. This decrease in oxidation state leads to about a 1.5 eV redshift in the M-edge absorption of Fe as shown in Fig 1-1. Lastly, even within the oxidation state of the same element, the way in which the electrons arrange themselves within the atom can lead to clear changes in the x-ray absorption. This spin-state selectivity has been shown both theoretically and experimentally. For example, simulated spectra of the Fe^{3+} $^4T_1$ state and the Fe^{3+} $^6A_1$ state are also shown in Fig. 1-1. Experimentally this has been shown by exciting the $[Fe(tren(py)_3)]^{2+}$ complex from its low spin $^1A_{1g}$ state to its high spin $^5T_{2g}$.[24] Furthermore, structural information can be gleaned from x-ray absorption spectroscopy because once a core-electron is excited, it still interferes with electrons in neighboring atoms. By doing so, it is possible to measure the coordination environment of the parent atom, even small deviations from it, as well as interatomic distances between the parent atom and its nearest neighbors.

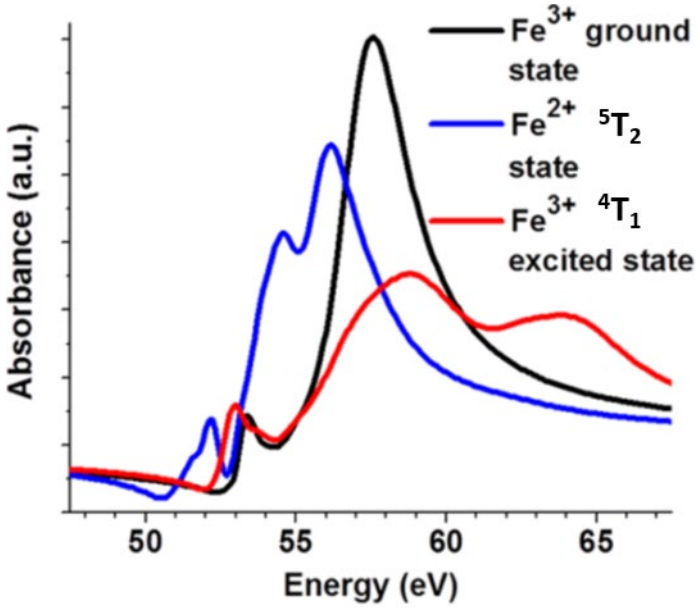

Figure 1-1: Each x-ray absorption spectrum is vastly different, depending on the electronic configuration of the iron atom. The black line represents the Fe^{3+} $^6A_1$ electronic configuration, which is the ground state for Fe_2O_3. The blue line is the Fe^{2+} $^5T_2$ configuration, which can be occur when Fe_2O_3 is optically excited, and shows a 1.5 eV redshift of the absorption edge, and a distinctly different shape. The red line is the Fe^{3+} $^4T_1$ configuration, again demonstrating how x-ray absorption is sensitive to the local environment. Adapted from Ref 23.

1.1.2 X-ray absorption spectroscopy

X-ray absorption spectroscopy (XAS) is one of the many different types of spectroscopy that can be performed by exciting a core electron above the Fermi level of a material, as seen in Fig. 1-2. The XAS process occurs when the incident photon has enough energy to promote a core electron into a bound state above the Fermi level, but not enough energy to eject the electron into the continuum. In this case, the excitation leaves behind a vacancy called a core-hole, whose charge is screened by the photoexcited electron. The core hole can then decay either through radiative recombination, leading to x-ray fluorescence, or non-radiative decay in the form of Auger decay, wherein an electron from a higher energy level fills the core hole, and the energy given off is used

to excite another electron up to an unoccupied level. These processes can take place multiple times, in turn leading to multiple core-holes being created and filled, until the system returns to its ground state. A core-hole is very unstable and thus very short lived, with deeper core-holes decaying faster than shallow ones, generally with lifetimes on the order of 1 fs (10^{-15} s). Thus, given time-energy uncertainty relation,

$$\Delta E \Delta t \sim \hbar \cong 10^{-16}\, eV \cdot s, \tag{1.1}$$

the lifetime broadening of a core-excitation is generally on the order of 0.1 eV. Despite being short-lived, the core-hole potential still has a significant effect on its surroundings and must be taken into account when calculating transition probabilities for XAS spectra.

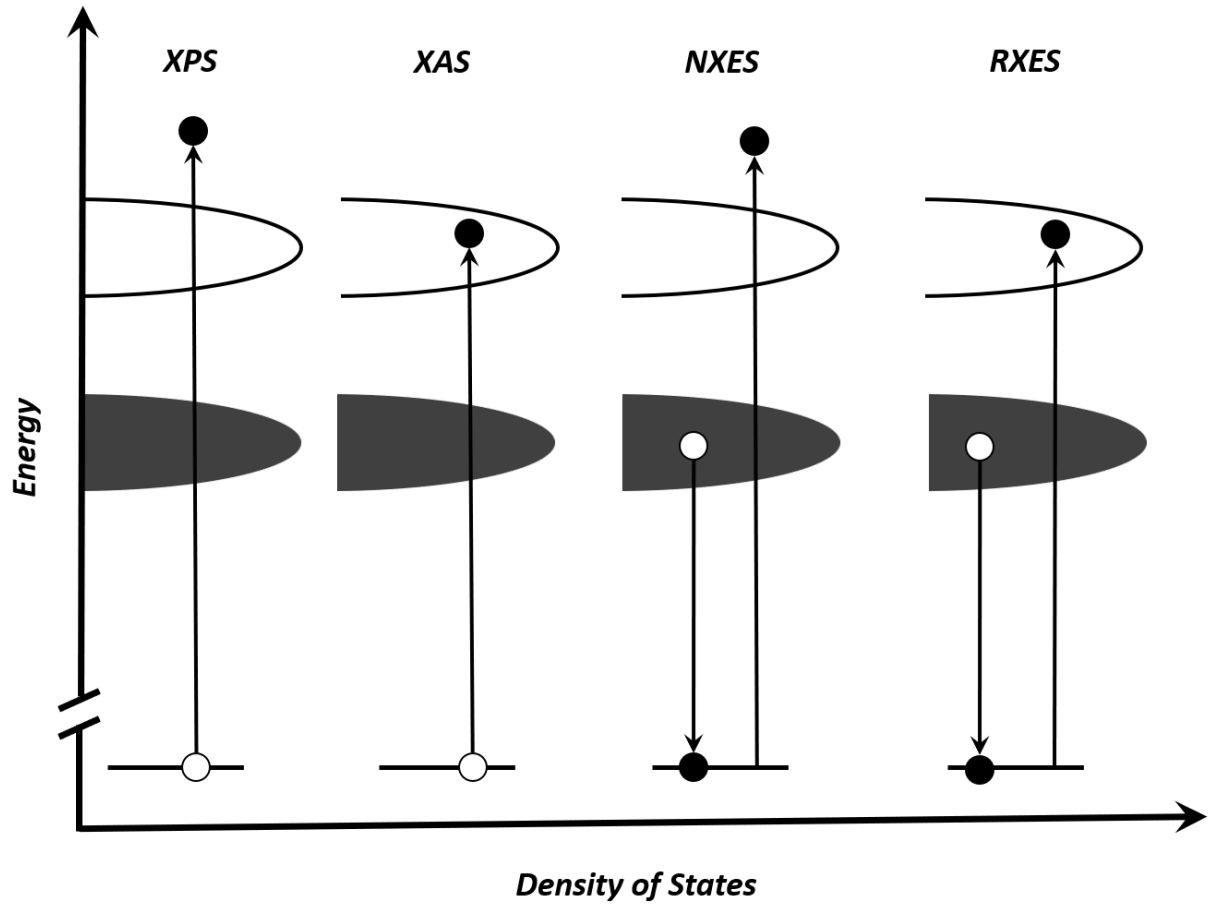

Figure 1-2: There are many possible types of spectroscopy available by exciting a core electron. All of these techniques give information about the local electronic environment of the absorbing atom. In x-ray photoelectron spectroscopy (XPS) a core electron is ejected into the continuum and its kinetic energy is measured. In x-ray absorption spectroscopy (XAS) a core electron is excited above the Fermi level into a vacant bound state. In normal x-ray emission spectroscopy (NXES) a core electron is ejected into the continuum and a valence electron fills the created core-hole, emitting an x-ray. In resonant x-ray emission spectroscopy (RXES) a core electron is excited above the Fermi level into an empty bound state and a valence electron fills the created core-hole, emitting an x-ray.

Like other absorption processes, x-ray absorption is governed by Fermi's Golden Rule, where the transition probability W_{fi} of going from an initial state Φ_i to a final state Φ_f (with energies E_i and E_f), and is mediated by the transition operator $\hat{T}$, is given by,

$$W_{fi} = \frac{2\pi}{\hbar}\left|\langle\Phi_f|\hat{T}|\Phi_i\rangle\right|^2 \delta(E_f - E_i - \hbar\omega), \tag{1.2}$$

where $\hbar$ is the reduced Planck's constant, ω is the angular frequency of the incident photon, and δ is the delta-function. X-ray absorption is a single photon process and the transition operator is often approximated to only include the electric dipole transition since the electric quadrupole term is two orders of magnitude smaller for elements with atomic number Z up to 30. Thus, the transition probability becomes,

$$W_{fi} = \frac{e^2}{\hbar c}\frac{4\omega^3}{3c^2} n \sum_q \left|\langle\Phi_f|\boldsymbol{e_q}\cdot\boldsymbol{r}|\Phi_i\rangle\right|^2 \delta(E_f - E_i - \hbar\omega), \tag{1.3}$$

where e is the electronic charge, c is the speed of light in a vacuum, n is the number of photons, and $\boldsymbol{e_q}$ is the photon polarization vector. It follows that the usual selection rules under the dipole approximation apply, where the change in angular momentum is $\Delta l = \pm 1$ and the change in spin is $\Delta s = 0$. In general, the form of the wavefunctions Φ_i and Φ_f are unknown, and certain approximations can be made in order to calculate the transition probabilities.

Furthermore, the delta function in Eq. 1.2 implies that what is actually observed in the case of a solid is the empty density of states (DOS), ρ. It is found then that the x-ray absorption process can be approximated as,

$$I_{XAS} \propto M^2 \rho, \tag{1.4}$$

where M is the matrix element from Eq. 1.3. It then becomes clear that the XAS process is described by the empty DOS modified by the matrix element. Since the core electrons are tightly bound to the nucleus, the initial state is usually well approximated by an atomic-like state, with well-defined quantum numbers, l, m and s. The final state and the DOS however, are both complicated by the existence of the core-hole. Therefore, in order to accurately describe the XAS spectra, it is important to take into account both the highly localized nature of the core-hole and the delocalized nature of the entire condensed matter system. Thus, in a solid, the net effect of the core-hole on the XAS spectrum is to modify the observed empty DOS, as seen in Fig. 1-3, in the case of Fe_2O_3.

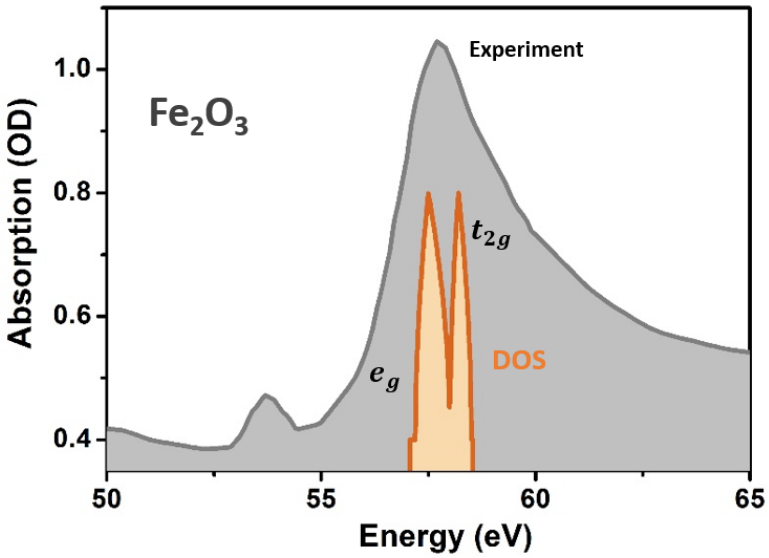

Figure 1-3: The majority of the empty density of states for Fe2O3 only spans about 5 eV and is composed of two main bands coming from the degeneracy split eg and t2g d-orbitals. In the presence of the core-hole generated by x-ray absorption, the density of states can be seen as being modified, broadening the observed spectrum.

Theoretical approaches of varying degrees of sophistication exist to calculate these parameters, taking into account the core-hole and the extended crystalline system in different ways. These approaches generally fall under two different categories. The first is a localized, molecular cluster picture, which deals more exactly with multi-electron effects, such as atomic multiplets and charge-transfer, but is coupled to the larger system empirically. The second, deals with the extended nature of the system more exactly, dealing with the excitation of hundreds of atoms, but approximates the electron-electron and electron-hole interactions by considering the core-level excitation as a single electron process. Since condensed matter can have free electron densities on the order of 10^{28}, accurately describing the possible interactions between all of them from a first principles approach is computationally prohibitive. However, this is not so much of a problem when the VES of interest is composed of all paired electrons, such as in Si, thus the single electron approximation is mostly valid. On the other hand, when the VES contains unpaired electrons, such as in transition metals (TM) with partially filled *d*-shells, the electron-electron interactions become significant and the single electron approximation breaks down. A brief explanation of both approaches will be given in the following subsections.

1.1.3 Charge Transfer Multiplet Theory

As previously mentioned, transition metals (TM) have partially filled *d*-shells. This, along with the fact that a core-excitation leads to a partially filled core-shell (e.g. a $3p^5$ configuration), means that the core wavefunctions and the 3*d* wavefunctions will strongly overlap. This wavefunction overlap creates final states that are much different than what would be expected in the single electron picture. This is known in atomic physics as the multiplet effect, and can also

have a strong effect in the solid-state case[25]. In the XAS of TM solids this effect is hardly screened and it often dominates the spectrum. The starting point of the charge transfer multiplet (CTM) theory then is the localized, atomic picture. Subsequently, the symmetry of the lattice is taken into account using ligand-field multiplet theory (LFM) and lastly, the charge-transfer effects due to the screening of the core-hole by the ligands is taken into account, although this is a much weaker effect in XAS since the excited core-electron (now part of the VES) screens its own core-hole.

The starting point for the atomic multiplet theory is to determine the initial and final states that will be used in Eq. 1.3. To do so, the Schrödinger equation must be solved using an atomic Hamiltonian. When multiple electrons are involved, the atomic Hamiltonian is given by,

$$H_{ATOM} = T + V + H_{ee} + H_{ls}, \tag{1.5}$$

where T is the usual kinetic energy term, V is the Coulomb potential between the electron and nucleus, and the last two terms account for the electron-electron repulsion (H_{ee}) and the spin-orbit coupling of each electron (H_{ls}). The electron-electron interactions of Coulombic repulsion and exchange are taken into account in the H_{ee} term, which are calculated using the Slater-Condon rules. The spin-orbit coupling scheme will depend on the element in question and it is well known that for light elements[26], the spin-orbit interaction is small such that pure *LS*-coupling can be used. On the other hand, for heavy elements, the spin-orbit interaction of individual electrons becomes stronger than the electrostatic interactions between electrons and thus *jj*-coupling must be used, however this is rare.

When multiple electrons are involved in an open shell, there are many ways to organize the electrons in the available orbitals. The initial state configuration for the core-excitation of a TM ion is $3d^n$, while the final state configuration is considered to be $3p^5 3d^{n+1}$ where an electron from the 3*p* core level has been excited into the 3*d* shell (the principal quantum number does not matter). Since these configurations give rise to multi-electron states, in general they will have total orbital angular momentum *L*, total spin angular momentum *S*, and total angular momentum *J*, with term symbols ${}^{2S+1}L_J$. For example, even in the simple case of a $3p^2$ configuration, there are 15 possible states available, with term symbols ${}^1S_0$, ${}^3P_0$, ${}^3P_1$, ${}^3P_2$, and ${}^1D_2$, where the *P* states are each triply degenerate and the *D* state is five times degenerate[26].

Once the relevant states are known, the next step is to use the atomic Hamiltonian given in Eq. 1.5 in order to calculate the matrix elements for Eq. 1.3. Calculating multiple electron wavefunctions is complicated, and some approximations must be made involving the Slater-Condon rules, especially for configurations with 3 or more electrons. The details for this can be found in Ref. 25. The important results are as follows: First, under the *LS* coupling scheme, and given Eq. 1.3, the usual dipole selection rules apply, $\Delta L = 1$, $\Delta S = 0$, and $\Delta J = +1, 0, -1$ but not $J' = J = 0$, significantly reducing the total number of states that need to be considered in the calculation. Second, the spin-orbit interaction mixes each state such that they become mixtures of the pure states. Core-level spin-orbit splitting usually is a much stronger effect (typically several eV) compared to the valence level split, but if the 3*d* shell is partially filled in the ground state, the valence-level splitting can become significant also. Third, the Slater-Condon parameters essentially shift the energy levels of each state and are diagonal to the *LS*-terms, such that each

state would remain pure if no spin-orbit splitting is included in the calculation. Whether the Slater-Condon parameters or the spin-orbit splitting dominate the spectrum will depend on the electronic configuration.

The next layer of the CTM theory aims to take the crystal lattice into account, thus incorporating the extended nature of the solid. However, due to the highly localized nature of the TM core-level excitations (again due to the partially filled *d*-shell), it is sufficient to only take into account the symmetry of the ligand field surrounding the metal atom. In other words, by simply considering a single atom and how its orbitals are affected by the ligand field around it, the correct spectrum can be obtained. This can be understood by considering a TM ion and its orbitals. In isolation, all 5 of its *d* orbitals will be degenerate in energy, however if the TM is bonded to ligands (e.g. 6 ligands in octahedral symmetry) each set of orbitals will experience a slightly different field, thus losing their degeneracy. The simplicity of this model is strengthened by the fact that it can take advantage of the results from group theory, taking the results from the atomic, spherically symmetric case (with point group SO_3) and branching them to point groups of lower symmetry (e.g. cubic, and octahedral).

Now, the Hamiltonian of interest includes not only the atomic multiplet Hamiltonian from Eq. 1.5, but also the crystal (or ligand) field Hamiltonian,

$$H_{LFM} = H_{ATOM} + H_{CF}, \tag{1.6}$$

$$H_{CF} = -e\phi(\boldsymbol{r}), \tag{1.7}$$

where $\phi(\boldsymbol{r})$ is the potential describing the surroundings of the TM ion. The potential $\phi(\boldsymbol{r})$ is given to be a series expansion of spherical harmonics and is treated as a perturbation to the atomic multiplet Hamiltonian. Once again, the details can be found in Ref. 25.

Other than this small perturbation, the main difference in the case of LFM theory is that the system is branched from atomic symmetry, SO_3, to a subgroup of it. By and large, most TM compounds bond to 6 or 8 neighbors. In the case of 6 ligands, the atoms can be seen to lie in the faces of a cube, forming an octahedral field. In the case of 8 ligands, the atoms can be considered to lie in the corners of the cube, forming a cubic field. Both of these systems belong to the O_h point group, which is a subgroup of SO_3, and the branching for this is given in Table 1-1. It can be seen that a state with *S* symmetry only branches to one other state, namely A_1, but a state with *D* symmetry can branch to multiple states, namely *E* and T_2. The dipole operator has *p* symmetry and thus it will branch into T_1 symmetry. In essence, the ligand field opens up new states that can contribute to the XAS spectrum. Furthermore, when the *d* orbitals are split by the ligand field, the energy difference between the different symmetry orbitals (e_g and t_{2g}) is often referred to as 10 *Dq* (also known as Δ), and this energy difference will clearly depend on the strength of the ligand field. However, the Slater-Condon parameters are also relevant in determining the energy of the split states, accounting for the electronic Coulomb and exchange interactions. In the case of TMs, for convenience the Slater-Condon parameters are often summarized using the Racah parameters[27]. Tanabe and Sugano[28] empirically derived a relationship between the crystal field parameter and Racah's parameters for the different electronic configurations of the d^n orbitals.

This relationship is often summarized in the form of the Tanabe-Sugano diagrams, exemplified for the case of a d^5 configuration in Fig. 1-4. It can be seen that at a crystal field strength of 0, there is no splitting of the atomic states, while as the 10 Dq value increases, the atomic states continuously split. The solid line represents the point at which the crystal field splitting energy surpasses the energy required to pair electrons, suddenly making it so a low-spin configuration is lower in energy than a high-spin configuration.

SO_3		O_h (Butler)	O_h (Mulliken)
S	0	0	A_1
P	1	1	T_1
D	2	$2 + \hat{1}$	$E + T_2$
F	3	$\hat{0} + 1 + \hat{1}$	$A_2 + T_1 + T_2$
G	4	$0 + 2 + 1 + \hat{1}$	$A_1 + E + T_1 + T_2$

Table 1-1: Branching Rules for the symmetry elements going from atomic symmetry (SO_3) to octahedral symmetry (O_h) in both Butler and Mulliken notation.

Finally, the charge transfer effects to the XAS spectrum can be included, completing the CTM theory. In a TM complex, the positively charged TM ion can sometimes strongly attract the electron density of the ligands. This is crucial in the case of x-ray photoemission spectroscopy, where the core-hole is not screened by the photoexcited electron, and must be screened instead by the valence electrons (which in the molecular cluster picture must come from the ligands). The main aspect of the CTM theory then, is to include other configurations in the calculation. For example, instead of having a single initial and final configuration like $3d^n \rightarrow 3p^5 3d^{n+1}$, charge transfer configurations, $3d^{n+1}\underline{L} \rightarrow 3p^5 3d^{n+2}\underline{L}$, can also be considered, and in fact higher order configurations can be included. Here $\underline{L}$ represents a hole in the ligand, with the electron being transferred to the 3d shell. The multiplet effect will also be incorporated for each of these extra configurations, leading to many more available states. For the most part, this effect is not very important for XAS since the core-hole that is created is screened by the photoexcited electron, making it a neutral process. If the CTM theory is used in the case of XAS, it usually just leads to small satellite peaks and a contraction of the multiplet structures. On the other hand, in the case of x-ray photoemission spectroscopy, which has a neutral initial state but a positively charged final state, the charge-transfer effect is crucial for predicting spectra. Lastly, it is important to note that efforts are being made to incorporate multiplet effects from a first principles approach[29,30]. These theories generally use DFT to calculate the DOS and use this directly with the multiplet.

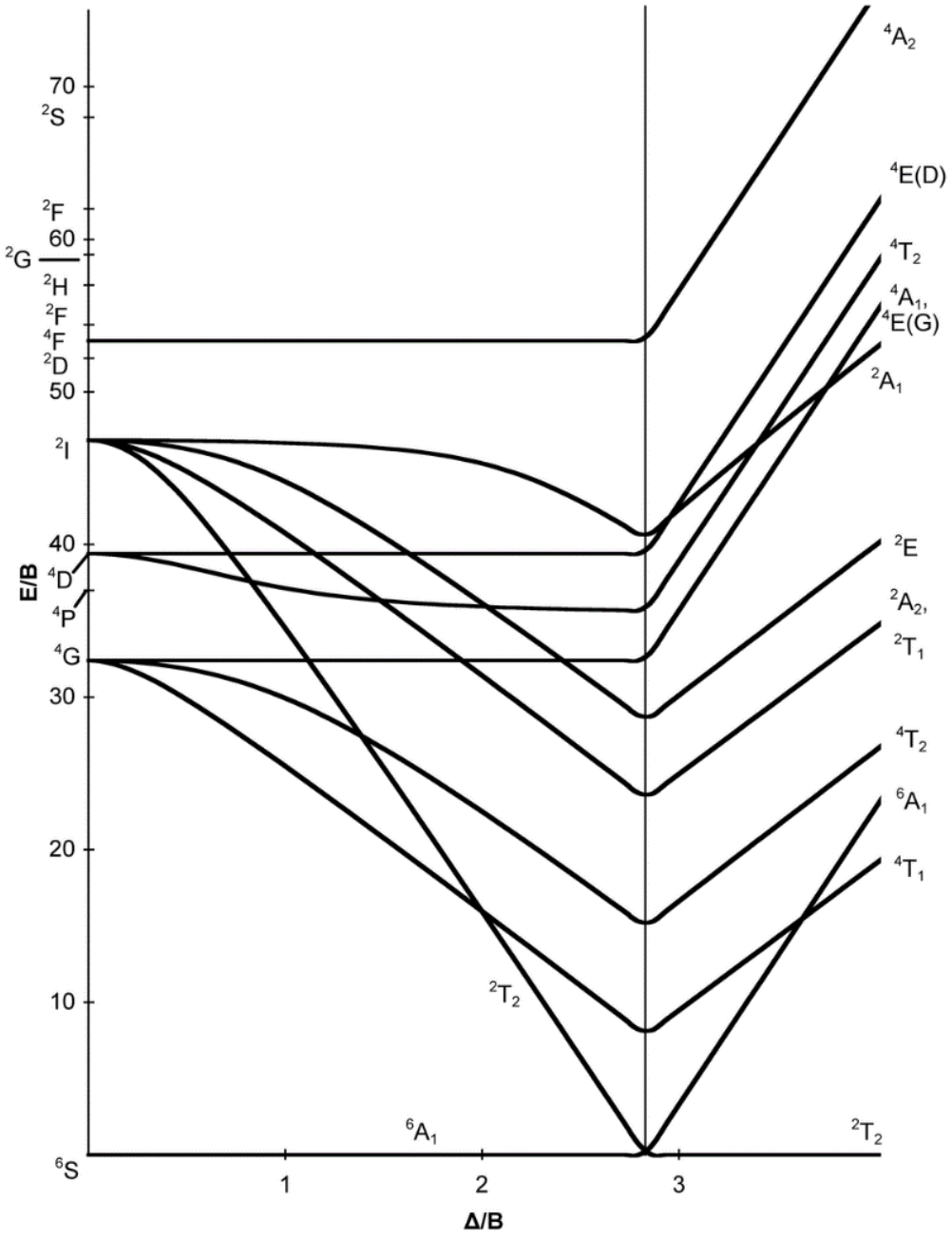

Figure 1-4: The Tanabe-Sugano diagram for a d^5 configuration. The x-axis represents the crystal field splitting energy scaled by the Racah B parameter. The y-axis gives the energy of a state, also scaled by the Racah B parameter. At a Δ value of 0, each state is still in spherical symmetry, with many configurations being degenerate in energy. As the Δ value increases, each state is branched into octahedral symmetry, splitting the degeneracy of the *d* orbitals. The ground state configuration as determined by Hund's rules is placed at 0 energy. The vertical line represents the point at which the crystal field energy surpasses the spin pairing energy, and the ground state configuration shifts from an $^6A_1$ to a $^3T_2$ configuration, representing a shift of the ground state from high spin to low spin.

1.1.4 Bethe-Salpeter Equation Method for Predicting XAS Spectra

The semi-empirical method described above is extremely useful in describing the XAS spectra of TM compounds, specifically the near edge structure, in many cases giving the best match between theory and experiment to date. However, different assumptions must be made to describe the XAS spectra of other classes of materials, for example semiconductors, or simple metals. First-principles approaches have typically excelled at describing the extended region of XAS[31–33], based on the scattering of a single electron with neighboring atoms, using a real-space Green's function method. On the other hand, the XANES region of the x-ray absorption process is not as well described by this method, especially when the spherical approximation for the core-potential breaks down, as in the case of semi-core levels (for details about semi-core level see section 1.1.5). More recently, first-principle theoretical approaches focusing on addressing the many-body effects in XAS have been developed. In this approach, density functional theory (DFT) is used to calculate the ground state electronic density of states and wave-functions, while the Bethe-Salpeter equation (BSE) is used to calculate the electron-hole states, including the electron and hole self-energies. Unfortunately, this BSE method has been fairly computationally expensive, limiting its use to a few tens of atoms, as opposed to the hundreds of atoms used in simpler approaches mentioned above. In an effort to reduce the computational cost to using this method, the OCEAN code (Obtaining Core-level Excitations using *Ab-initio* methods and the NIST BSE solver) was developed[34,35]. This code is freely available for download from the University of Washington, through the FEFF Project, with the only requirement being that the user must register online.

In contrast to the theory in section 1.1.2, which focuses on calculating the transition probabilities between initial and final multiplet states, the BSE based theory begins with the fact that the x-ray absorption process can be described in terms of the energy loss function,

$$\sigma(\boldsymbol{q},\omega) = -Im\epsilon^{-1}(\boldsymbol{q},\omega), \tag{1.8}$$

where the dielectric function ϵ depends on both the photon energy ω, and momentum transfer, $\boldsymbol{q}$. More formally, a many-body description of the energy loss function can be given by,

$$\sigma(\boldsymbol{q},\omega) \propto -\frac{1}{\pi} Im\langle 0|\hat{O}^{\dagger} G(\omega)\hat{O}|0\rangle, \tag{1.9}$$

where $|0\rangle$ is the many-body ground-state wavefunction, $\hat{O}$ is the operator describing the interaction between the photon field and the system, and $G(\omega)$ is the Green's function for the many-body excited state. The transition operator will depend on the process of interest, but in the case of XAS it is given by the expansion,

$$\hat{O} = (\boldsymbol{e}\cdot\boldsymbol{r}) + (i/2)(\boldsymbol{e}\cdot\boldsymbol{r})(\boldsymbol{q}\cdot\boldsymbol{r}) + \cdots \tag{1.10}$$

where $\boldsymbol{e}$ is the photon polarization vector. Lastly, the Green's function is used in combination with the Bethe-Salpeter Hamiltonian H_{BSE} as,

$$G(\omega) = [\omega - H_{BSE}]^{-1}, \tag{1.11}$$

where the Bethe-Salpeter Hamiltonian is usually given by,

$$H_{BSE} = H_e - H_h - V_D + V_X, \tag{1.12}$$

with the core-hole term given by,

$$H_h = \varepsilon_c + \chi - i\Gamma, \tag{1.13}$$

where ε_c is the average core-level energy, χ is the spin-orbit interaction, and Γ is the core-hole lifetime. The other Hamiltonian term describes the excited electron,

$$H_e = H_{KS} + \Sigma^{GW} - V_{XC}, \tag{1.14}$$

where H_{KS} is the Kohn-Sham Hamiltonian, corrected by the GW self-correction Σ^{GW}, and the exchange-correlation term V_{XC} is subtracted to prevent double counting. The next two terms in the BSE Hamiltonian describe the interaction between the excited electron and the core-hole, which interact in the presence of the mean field of the remaining electrons. The first term is the direct Coulomb attraction term,

$$V_D = \hat{a}_c(\boldsymbol{r}', \sigma')\hat{a}_V^\dagger(\boldsymbol{r}, \sigma)W(\boldsymbol{r}, \boldsymbol{r}', \omega)\hat{a}_V(\boldsymbol{r}, \sigma)\hat{a}_c^\dagger(\boldsymbol{r}', \sigma'), \tag{1.15}$$

where $W(\boldsymbol{r}, \boldsymbol{r}', \omega)$ is the screening due to the mean field of the remaining electrons in the system. The last term in the BSE Hamiltonian is the repulsive exchange term,

$$V_X = \hat{a}_c(\boldsymbol{r}, \sigma)\hat{a}_V^\dagger(\boldsymbol{r}, \sigma)\frac{1}{|\boldsymbol{r} - \boldsymbol{r}'|}\hat{a}_V(\boldsymbol{r}', \sigma')\hat{a}_c^\dagger(\boldsymbol{r}', \sigma'), \tag{1.16}$$

and it is treated as a bare interaction. In both of these interaction terms, $\hat{a}_c^\dagger(\hat{a}_c)$ and $\hat{a}_V^\dagger(\hat{a}_V)$ are the creation (annihilation) operators for the core-levels and the valence-levels, respectively.

One of the biggest advantages of the OCEAN code is its efficiency in solving for these parameters, opening up the possibility to use the BSE method for solids. Several approximations are made in order reduce the computational cost of this method. First, a projector augmented wave (PAW) approach is used to solve for the Kohn-Sham equations. The PAW approach uses pseudopotentials to reduce the total number of electrons and the size of the plane-wave basis. Next, the GW self-energy is approximated using an efficient many-pole model. Also, the dielectric screening term in Eq. 1.15 is found by using a real-space random phase approximation inside a sphere localized around the absorbing atom along with a Levine-Louie model dielectric function outside the sphere to model the long-range dynamics.

Taking all of these approximations into account, the OCEAN code can be used to calculate the XAS spectra of solid-state materials from a first-principles approach, as can be seen in the example of the $SrTiO_3$ spectrum in Fig. 1-5. Previous iterations of the code were only able to simulate clusters of tens of atoms, but the latest version can accurately model up to 500 atoms with 3200 valence electrons in around 12.5 hours[34]. The advantages of using an *ab-initio* method are many, including the possibility of incorporating defects, impurities/dopants, as well as

incorporating band structure effects. Despite these advantages, the computational cost remains high compared to semi-empirical models, and the fact that the many-body interactions are approximated by a two-particle interaction means that the trade-offs between this method and localized cluster methods must be considered depending on the application of interest. Nevertheless, what has been shown in these sections is that the theoretical approaches for predicting the notoriously difficult XANES region of XAS are already excellent in some respects and will continue to improve.

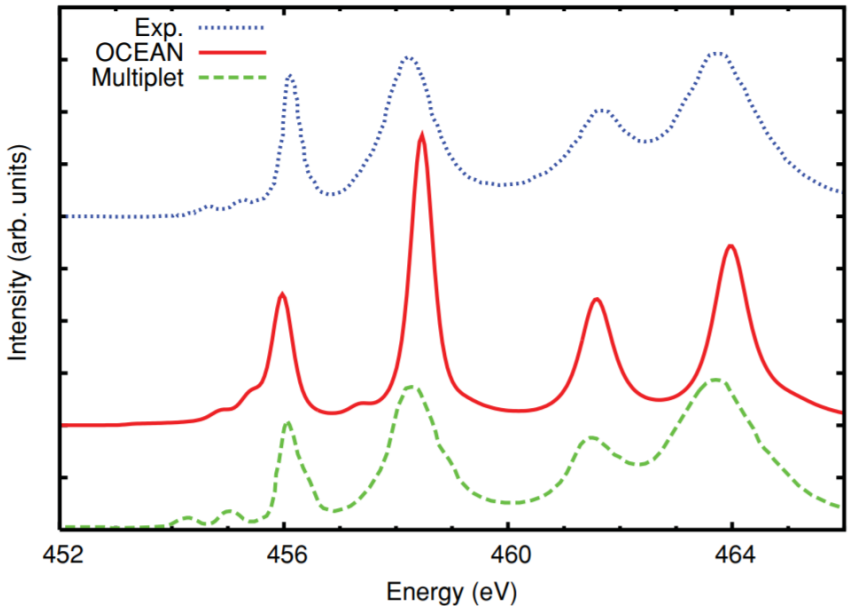

Figure 1-5: The calculated XANES spectra for the Ti $L_{2,3}$ edge of $SrTiO_3$ (red, solid line) compared to experimental data (blue, dotted line) and a multiplet calculation (green, dashed line). Clearly, the semi-empirical CTM calculation still has the best match to the experimental data in the case of TM compounds. On the other hand, the OCEAN code is a full *ab-initio* calculation done on a 5 × 5 × 3 supercluster, which takes into account the interactions between electrons, can also closely match the experimental data. However, the computational cost for the OCEAN code is still large compared to the CTM code. Reprinted from Ref. 35.

1.1.5 Importance of semi-core level

In the case of solids, electrons are generally separated into core electrons, which are seen as being atomic-like and do not participate in bonding, and valence electrons, which do participate in bonding between atoms and are thus delocalized. However, as might be expected, in reality this distinction is not infinitely sharp. In fact, another class of electron exists, called the semi-core electron[36,37], which shares properties both with the deep core levels and with the shallow valence levels of a solid. For many types of materials, this distinction is not as important and the core states are approximated with a simple pseudopotential, essentially freezing the core-electrons in place along with the ionic, nonpolarizable nucleus. However, as explained in section 1.1.3, transition metals exhibit a strong overlap between the 3*p* core levels and the 3*d* valence levels due to a partial

occupancy of both shells. Therefore, it can be expected that the 3*p* electrons will have a strong semi-core character.

The importance of the semi-core then, lies in the fact that it carries both delocalized band structure information as well as localized atomic information. This becomes especially important when the dynamics of the solid come into play. For example, many transition metal compounds are known to exhibit polaronic conduction[38] (described in more detail in section 1.2.3), which may occur in the form of polaron hopping. In this interpretation, a conduction electron must overcome a potential energy barrier to hop from one atom to the next, polarizing the ionic lattice itself, modifying bond-lengths wherever it goes. This nuclear reorganization in turn will lead to a valence electronic reorganization. If all core-electrons are assumed to be frozen throughout this process, then there should be no change to the XAS spectrum during it. Of course, it should be expected that the core-levels are somewhat sensitive to polaronic conduction, however it is not clear what the extent of this sensitivity should be, especially for the case of semi-core levels. The use of x-ray transient absorption spectroscopy is uniquely poised to tackle this question and is in fact used to answer it in chapter 3 of this thesis, finding that a surprisingly large shift (>1 eV) in the XAS spectrum is observed during polaron formation.

1.2 Electron and Lattice Dynamics in Solids

As previously mentioned, condensed matter dynamics are complicated by the fact that an Avogadro's number of nuclei and even more electrons are interacting with each other at once in order to determine the material's macroscopic properties. Due to the complicated nature of these interactions, much of the analysis on condensed matter has focused on separating the electronic and atomic dynamics. In fact, not only are the electrons assumed to not interact with the lattice, they are often assumed to not interact with each other as well. For certain properties in certain types of materials, such as the electronic conduction of simple metals, this assumption is often valid and the conduction electrons can be viewed as being independent from the ions that make up the lattice. However, this assumption is actually not valid for many materials, especially those that have strongly correlated electrons. When this assumption breaks down, not only can electrons interact with the lattice through scattering events, changing their momentum, they can also interact in a coordinated, long-lived manner, known as polarons. Furthermore, if an electron is given excess energy above its conduction band minimum, it can dissipate this energy to the lattice in the form of electron-phonon scattering. The interactions between charge carriers and the lattice are especially important when it comes to solar energy conversion since the optical absorption leads to excited carriers which must efficiently travel across a material.

1.2.1 Electron Dynamics

Much like in molecular orbital theory, where atomic orbitals combine to form larger molecular orbitals, when a very large number of atoms come together to form a solid, their valence orbitals can come together to form energy bands. This band theory of solids has been extremely successful in predicting macroscopic properties of vastly different types of materials. In this theory, condensed matter is generally categorized according to its band structure and how it is populated by the electrons in the solid. Since electrons behave according to the Pauli exclusion principle,

they obey Fermi-Dirac statistics, which can be applied to the filling of the bands in a solid. The total density of electrons in a solid is given by[39],

$$\frac{N}{V} = \int_{-\infty}^{\infty} g(E) f(E) dE, \tag{1.17}$$

where N is the total number of electrons, V is the total volume of the solid, $g(E)$ is the electronic density of states, which will depend on the material, and $f(E)$ is the Fermi-Dirac distribution,

$$f(E) = \frac{1}{1 + e^{(E-\mu)/k_B T}}, \tag{1.18}$$

where μ is the total chemical potential of electrons, often referred to in solid-state physics as the Fermi level, E_F. The Fermi level then is the amount of work required to add one electron to the solid, and at thermodynamic equilibrium, represents the energy level that would have a 50% probability of being filled. The Fermi level is a crucial parameter in solids, and, depending on its position within a band structure, will determine whether the material is a metal, semiconductor, or an insulator, as shown in Fig. 1-6. If the Fermi level resides within a band, it means it will be partly filled and electrons can easily respond to an external electric field and conduct throughout the band, meaning the material will be a metal. If the Fermi level resides in a gap between bands, but the gap is small, there will be some probability of finding thermally excited electrons coming from the lower band to the upper band, and the material is a semiconductor. Lastly, if the Fermi level resides within a large gap, there is no chance of an electron being found in the top band at thermodynamic equilibrium such that all lower bands are completely filled, and the material is an insulator. The above is true for any solid, but calculating the band structure is not trivial. Depending on the atomic composition and crystalline structure, different assumptions must be made in order to do so.

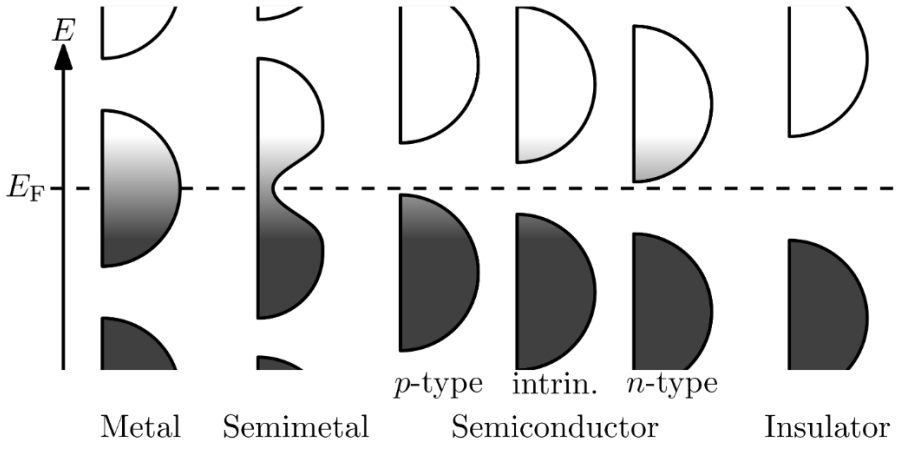

Figure 1-6: Illustration of the different classes of materials, which are classified by the position of the Fermi level with respect to the bands. Here the y-axis represents energy, while the width of each band represents the density of available states. The shading represents the Fermi-Dirac thermal distribution. Black represents filled, while white represents empty. In a metal, E_F lies within a band, such that electrons can easily move around it. In a semimetal, E_F lies within a narrow band, such that electrons can freely

move, but with lower density of states available. In semiconductors and insulators, E_F lies within a bandgap. However, for semiconductors, the bandgap is small enough such that electrons can be thermally excited across it, while for insulators the bandgap is too wide, so bands are either completely empty or completely filled.

At one extreme lies the free electron model, where the electrons in a solid are assumed to be independent and to behave exactly like in a Fermi gas, not interacting with each other or the ions that make up the lattice. Thus, the crystalline structure does not come into play and the density of states for a 3-dimensional free electron gas can be analytically determined to be[39],

$$g(E) = \frac{m_e}{\pi^2 \hbar^3} \sqrt{2 m_e E}. \tag{1.19}$$

Despite being very simple, this theory was successful in explaining several properties of simple metals such as the heat capacity, as well as the thermal and electrical conductivities, but it does not predict the existence of semiconductors and insulators.

A major improvement to this theory is the nearly free electron model, where the periodicity of the lattice is taken into account. The electrons are still considered to be independent from each other, but now are weakly perturbed by a periodic potential coming from a homogenous crystal lattice of ionic cores. By doing so, the Schrodinger equation can be solved for a periodic potential and the electronic wavefunctions can be described as Bloch waves,

$$\psi_k(\boldsymbol{r}) = e^{i\boldsymbol{k}\cdot\boldsymbol{r}} u_k(\boldsymbol{r}), \tag{1.23}$$

where u has the same periodicity as the lattice, such that $u_k(\boldsymbol{r}) = u_k(\boldsymbol{r} + \boldsymbol{R})$, with $\boldsymbol{R}$ being a translation vector of the lattice. Simply by taking the periodicity of the lattice into account, the existence of band gaps, and thus semiconductors and insulators, fall out of the theory[39,40]. Another important concept that emerges is that of the electronic effective mass m^*, which can be larger or smaller than that of a free electron, even being negative. The case of negative effective mass means that an electron can move in the opposite direction of the applied electric field, as if it were positively charged. For this reason, it is often described as being a hole, or electron vacancy. Lastly, the nearly free electron model predicts that a material can only be an insulator when the number of valence electrons in a primitive unit cell is even. The material could still be a metal in this case depending on the band structure, specifically if bands overlap in energy. However, this also implies that materials with an odd number of valence electrons in a primitive cell must be metallic, since a band will always be partially filled. Thus, transition metal compounds, such as oxides, should be metallic since they have partially filled *d*-shells. However, it has been experimentally determined that many transition metal oxides have wide bandgaps, making them insulators. For example, TiO_2, Fe_2O_3, and Cu_2O have bandgaps of 3.2, 2.1 and 1.6 eV, respectively[41]. As usual, when it comes to transition metal behavior, this is due to the fact that the partially filled *d*-shell has unpaired electrons that would prefer to remain far apart from each other.

At the other extreme is the tight-binding model. This is an extension of the linear combination of atomic orbitals (LCAO) typically used in molecular orbital theory. In this model, electrons are approximated as being tightly bound to the atomic nucleus, and as atoms are brought close

together, their orbitals start to overlap making it so electrons can hop between sites. This is the base of the model, but it can be formulated in different ways, either neglecting or incorporating electron-electron interactions. In the case of no interaction, the tight-binding Hamiltonian can be given in second quantization form,

$$H_{TB} = -\sum_{i,j}(t_{ij}\hat{c}_i^\dagger \hat{c}_j + t_{ji}\hat{c}_j^\dagger \hat{c}_i) + \sum_i V_i \hat{c}_i^\dagger \hat{c}_i, \tag{1.21}$$

where t_{ij} is the probability amplitude of hopping from site i to site j, $\hat{c}_i^\dagger(\hat{c}_j)$ is the creation (destruction) operators for an electron at site i, and V_i is the potential energy of having an electron in site i. Generally, only nearest neighbor hopping is considered since the probability of hopping to next nearest neighbors and beyond are much less likely. On the other hand, if the interaction between electrons is important, the Hubbard model can be invoked. In this case, the tight-binding Hamiltonian is modified only slightly, retaining the kinetic energy term describing hopping between sites, but including a potential energy term that describes the interaction between electrons,

$$H_H = -\sum_{i,j\sigma}(t_{ij}\hat{c}_{i\sigma}^\dagger \hat{c}_{j\sigma} + t_{ji}\hat{c}_{j\sigma}^\dagger \hat{c}_{i\sigma}) + \sum_i U_i \hat{n}_{i\uparrow}\hat{n}_{i\downarrow}, \tag{1.22}$$

where σ in the first sum represents the spin polarization of the electron being counted, and the U_i term is the energy required to have a site be doubly occupied, with $\hat{n}_{i\sigma} = \hat{c}_{i\sigma}^\dagger \hat{c}_{i\sigma}$. This model is surprisingly useful in describing materials like transition metal oxides, which under the independent electron approximation are expected to be metallic, but in reality, are mostly insulating. The Hubbard model predicts the metal to insulator transition by considering the relative strength of the hopping parameter t and the repulsion term U.[42] If $t \gg U$, the material is metallic as hopping is very favorable and the repulsion between electrons is negligible. At the other extreme, where $t \ll U$, the material becomes insulating since the repulsion between electrons is strong enough to keep them from getting too close to each other. This transition between metallic and insulating character not only takes place across the transition metal compounds, but can be thermally or even optically induced as in the case of VO_2.[43]

1.2.2 Phonon Dynamics

In the previous subsection, the lattice is either neglected or considered to be rigid, focusing instead on the electron dynamics. This is a natural assumption since the electron mass and nuclear masses are so vastly different. However, the lattice degrees of freedom must have some impact on the macroscopic properties of solids as well, especially transport dynamics such as heat flow. Much like in the case of the electronic dynamics, the models describing the lattice dynamics do not invoke electronic effects. The simplest type of lattice to consider is the monoatomic lattice with only one type of atom per primitive unit cell. On the other hand, a lattice could have two atoms per primitive unit cell.

The simplest approximation that can be made to deal with a dynamic lattice is to consider it as a 1-dimensional chain of monoatomic harmonic oscillators. Instead of having the nuclei stationary at the points $\boldsymbol{R}$, defining the Bravais lattice, these points are now only the mean equilibrium position of the nuclei around which they can oscillate. Also, by assuming that the dislocations of the nuclei around these points is small, the harmonic oscillator approximation can be used, as if each atom were connected to each other by a spring. Again, only nearest neighbor interactions are assumed as a first approximation, but it is found that adding the interaction between next nearest neighbors does not significantly alter the results. Just like in the electronic case, since the number of atoms is so large, it is assumed that periodic boundary conditions apply here. What is left then is to determine the normal modes of vibration of the lattice. It is found that in this case, the dispersion relation for the normal modes is given by,

$$\omega_k = \sqrt{\frac{2K}{m}(1-\cos ka)}, \tag{1.24}$$

where K is the spring constant, m is the mass of the atoms and a is the distance between atoms. Due to the periodic boundary conditions, it is also found that the wavevectors must have the form, $k = 2\pi n/aN$ where N is the number of atoms in the lattice and only values of k ranging from $-\pi/a$ to π/a are unique. Thus, there are N normal modes of vibration.

The next possibility is when a primitive unit cell contains two different atoms in it. This could be either due to different masses or due to different spring constants, but since the result is the same, it is often just assumed that the atoms have different masses with the same spring constant. The same assumptions are made here as were made above. The dispersion relation then is found to be,

$$\omega_k^2 = K\left(\frac{1}{m_1}+\frac{1}{m_2}\right) \pm K\sqrt{\left(\frac{1}{m_1}+\frac{1}{m_2}\right)^2 - \frac{4\sin^2\frac{ka}{2}}{m_1 m_2}}. \tag{1.25}$$

Now there are two possible branches for each k value, doubling the normal modes to $2N$. The lower branch has the same form as for the monoatomic lattice, while the upper branch is new and has a different form, as seen in Fig. 1-7. It is also found that the atoms move in phase with each other for modes in the lower branch, while they move 180° out of phase for modes in the upper branch. Thus, if the lattice is composed of positive and negative ions, a photon can polarize it so that the ions move out of phase, so the upper branch is referred to as the optical branch. On the other hand, sound waves appear as a coherent motion of atoms such that they all move in the same direction, and so the lower branch is referred to as the acoustic branch. These results are for a 1D lattice, but the treatment is the same for 3 dimensions, except now the wavevectors are also three dimensional, so there are $3N$ degrees of freedom. Another distinction is that in the 1D case, motion only occurs along the chain, corresponding to longitudinal motion (L), but in the 3D case, there will also be transverse motion (T), often referred to as the LA (LO) and TA (TO) modes (A acoustic, O optical), respectively. Analogously to the molecular case, where there are 3 translational degrees of freedom and $3(N-1)$ vibrational degrees of freedom, in the solid case, there are 3 acoustic modes (two transverse and one longitudinal) and $3(N-1)$ optical modes.

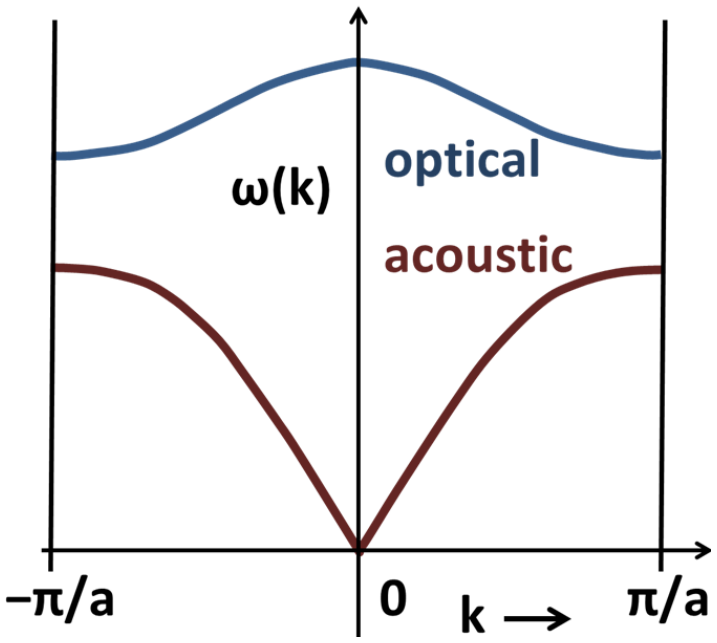

Figure 1-7: The phonon dispersion relations for the acoustic and optical branches within a Brillouin zone of a one-dimensional chain of atoms. The case of higher dimensions is analogous to this, except there will be more bands, each defined by a specific direction within the three-dimensional Brillouin zone.

Even though the above results are derived for a classical harmonic oscillator crystal, they are still valid when the quantization of the lattice is taken into account. In other words, there are still $3N$ normal modes of vibration, but the energy associated with each normal mode is quantized and given by,

$$E_n = \left(\frac{1}{2} + n\right)\hbar\omega_k, \tag{1.26}$$

where n is the excitation number and ω_k is still given by the dispersion relations found above. In analogy with the photon, which is the quanta of the electromagnetic field, a phonon is the quanta of the vibrational modes of the lattice. It is often more useful to speak in terms of phonons, especially when dealing with transport phenomena and scattering. Thus, instead of referring to the lattice being excited to the n^{th} level of the vibrational mode ω_k, it can be said that there exist n phonons with energy $\hbar\omega_k$. It is also interesting to note that due to the quantization of the vibrational modes, even at absolute 0, when there are no phonons, the lattice still has vibrational energy of $\hbar\omega_k/2$ contributed from each vibrational mode.

As is true for molecules, the harmonic approximation is extremely useful, but cannot fully explain the dynamics of lattices. In the case of solids, many energy transport effects must invoke anharmonicity to be fully understood. Phonon-phonon scattering is the main reason for this. For example, if the harmonic approximation was valid in all scenarios, a perfect, infinite crystal with insulating band structure would have infinite thermal conductivity since there would nothing for phonons to scatter with. In other words, making a crystal bigger (making the effects of the boundaries and impurities vanishingly small) would allow for infinite thermal conductivity. Thus,

the only way to realistically account for the thermal conductivity of an insulator is to consider phonon-phonon scattering, which cannot occur under the strictly harmonic approximation. By including the cubic and quartic terms in the expansion of the potential, the phonon-phonon interactions in Fig. 1-8 become available. It is important to note that low energy phonon scattering generally keeps the momentum of the scattered phonon within a Brillouin zone, and this is referred to as normal scattering. When high energy scattering takes place, it is possible for the momentum transfer to be large enough that the scattered phonon has a momentum outside the first Brillouin zone. However, any wavevector outside the first Brillouin zone is equivalent to one inside it (differing by one reciprocal lattice vector), so this type of scattering can in turn produce a phonon with lower momentum. This is the main process by which the thermal conductivity of insulators is lowered.

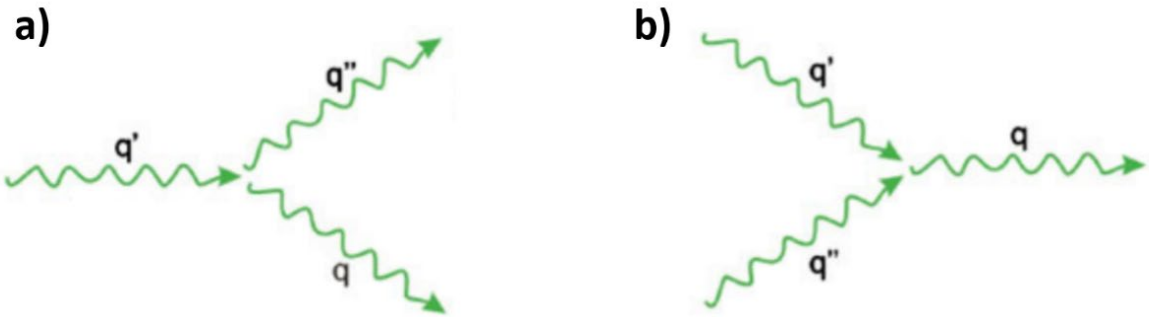

Figure 1-8: The different phonon-phonon scattering processes that can occur between 3 phonons. (a) represents the decay of a phonon into two other phonons, while (b) represents the combination of two phonons to create one phonon with momentum q. A normal scattering process occurs when the momentum of the scattered phonons remains within the first Brillouin zone, usually taking place between acoustic phonons. On the other hand, an Umklapp scattering event is when the scattered phonon momentum is large enough to lie outside the first Brillouin zone, which usually requires optical phonons. However, since all momenta are equal up to a reciprocal lattice vector, Umklapp processes actually serve to lower the momentum of the scattered phonon.

1.2.3 Electron-Phonon Dynamics and Polarons

So far, both the electron and phonon dynamics have remained independent of each other, and almost all properties of solids can be explained by doing so. However, the interaction between electrons and phonons must also have some impact on how solids behave macroscopically. For example, the heat capacity of metals, the electronic and thermal conductivities of both metals and insulators, the optical absorption of indirect semiconductors, and even superconductivity can only be fully explained by incorporating the interactions between electrons and phonons[39,40]. There are many possible classes of interactions between electrons and phonons due to there being different classes of phonons. Acoustic phonons have longer wavelengths and have low energy, so they typically give rise to elastic scattering, while optical phonons can have much higher energies and thus can lead to inelastic scattering events.

The scattering process between electrons and phonons can be described by their interaction Hamiltonian H_{e-ph} which is usually treated as a perturbation to the overall Hamiltonian of the system of electrons and phonons,

$$H = H_e + H_{ph} + H_{e-ph}. \tag{1.27}$$

Once again, the form of H_e will depend on which assumptions are made about the system. If electrons are mostly independent, a free electron or nearly free electron approach can be taken, leading to band conduction mechanisms, where electrons and holes are associated with effective masses. On the other hand, if electrons are fairly localized, a tight binding approach will be necessary, where there is a probability t of an electron hopping between nearest neighbor sites, and the effective mass approximation is not well defined. The H_{ph} term describes how many phonons there are with energy $\hbar\omega_q$, where ω_q represents the dispersion relation for either an acoustic or optical phonon. Lastly, the term describing the electron phonon interaction H_{e-ph} will also depend on the assumptions made, but the general form is given by[44],

$$H_{e-ph} = \sum_{k',k,q} g(\boldsymbol{k}, \boldsymbol{k'}, \boldsymbol{q}) c_{k'}^{\dagger} c_k \left(a_q + a_{-q}^{\dagger}\right), \tag{1.28}$$

where g is the electron-phonon coupling constant. It can be seen that this interaction Hamiltonian describes an event where an electron with momentum $\boldsymbol{k'}$ is created while an electron with momentum $\boldsymbol{k}$ is destroyed, and a phonon with momentum $\boldsymbol{q}$ is either created or destroyed (emitted or absorbed), where conservation of momentum dictates that $\boldsymbol{q} = |\boldsymbol{k} - \boldsymbol{k'}|$, up to a reciprocal lattice vector. There can be many different such interactions since the potential induced by different types of phonons will also differ. For example, covalent crystals (e.g. Si) cannot become polarized due to a deformation of the lattice, and so phonons in this case will only give rise to a slightly different deformation potential for electrons to scatter with, mostly leading to elastic scattering, which can take place either within a single band (intraband) or across bands (interband). On the other hand, polar or ionic lattices (e.g. Fe_2O_3 or NaCl) are susceptible to polarization when their atoms move from their equilibrium positions, especially in the case of optical phonons, such that interactions can become inelastic, lowing the energy of charge carriers, and in the extreme case, can even serve to combine electrons and phonons into a new quasiparticle called a polaron.

The polaron concept was first discussed by Landau[45] in 1933 as the effect of a slow-moving electron on the ions around it, where the electron is slow enough that the ions can shift from their equilibrium position to screen the electron charge. This shift then creates a potential well for the electron that can trap it. Since then, this concept has expanded to include most interactions between charge carriers and a polar lattice, being observed both in inorganic crystals[46] and organic materials such as polymers[47]. In essence the Coulomb interaction between charge carrier and lattice will always cause the lattice to shift from its equilibrium position, and charge carriers will travel through the material dressed by a cloud of phonons. The nature of the polaron will depend on the strength of the coupling between electrons and phonons, and in cases where the coupling is weak enough, the polaron concept can be ignored.

Large polarons (or continuum polarons) can form when the strength of the coupling between charge carriers and phonons is not strong enough to completely localize the carrier onto a single lattice site. In this case the charge carriers can still be approximated by an effective mass, freely moving through a modified conduction band, albeit with a much heavier effective mass. Since the continuum approximation is still valid, the polaron wavefunction can span several unit cells, hence the name. On the other hand, when the polaron binding energy is greater than half the bandwidth of the electron band, the discreteness of the lattice becomes important and the continuum approximation breaks down. In this case, the tight-binding picture must be used, and instead of being delocalized, the extent of the polaron spans only a single unit cell. In contrast, this is called the small polaron (or lattice polaron). The quantum theoretical framework behind these two cases were formalized by Frohlich[48] and Holstein[49] respectively, and since then both cases have been extensively investigated[46,47,50–53]. The impact of polaron formation on the conduction of charges in materials can be extreme. For example, the ground state conduction mechanism for Fe_2O_3 has been determined to be that of small polaron hopping, and its electron mobility has been measured[54] to be on the order of 10^{-2} $cm^2/V{\cdot}s$, while electron mobilities in Si are measured[55] to be on the order of 10^3 $cm^2/V{\cdot}s$.

Not only is electron-phonon scattering important under thermal equilibrium conditions, helping to determine the electrical and thermal conductivities, it also dominates the excited state dynamics of solids. The most commonly used technique to study these dynamics is ultrafast pump-probe spectroscopy. This involves using broadband femtosecond or attosecond laser pulses to optically excite the sample and then another pulse is sent in at a short time delay afterwards to probe the excited system. After absorption of the initial pulse, several scattering events take place before the system comes back to thermal equilibrium[56]. Immediately after excitation, the electronic distribution is highly non-thermal, and carrier-carrier scattering will dominate at timescales ranging from hundreds of attoseconds to tens of femtoseconds, bringing the electrons back to a thermal distribution, however at a much higher temperature than the lattice, which has not had time to react to the excitation. In the timescale of 10s of femtoseconds to 100s of picoseconds, electron-phonon scattering dominates, especially with higher energy LO phonons forming polarons in polar lattices, bringing the electronic and lattice temperatures into equilibrium with each other. At these timescales, the energetic optical phonons that have been created by the hot electrons will in turn decompose into acoustic phonons which can in turn scatter with carriers as well. Lastly, carriers can recombine, either through Auger or radiative recombination, and the system can return to thermal equilibrium with its surroundings.

1.3 High Harmonic Generation

Although synchrotron radiation generally has excellent flux and covers a very wide range of x-ray wavelengths, large and expensive facilities must be built to produce it. With the discovery of high harmonic generation (HHG), it became possible to create extreme ultraviolet (XUV) and soft x-ray light that was not only spatially coherent, but temporally coherent as well. High harmonic generation is a highly nonlinear process that can occur when a high energy, ultrashort, infrared or near-infrared laser pulse is tightly focused onto a target medium. Since the main process in HHG involves tunnel ionization of atoms, this makes it a fairly universal process and the target

medium can be in any phase of matter[57–59], although a noble gas is the most commonly used medium, making it the focus of this section.

1.3.1 Three Step Model

The process of high harmonic generation can be intuitively understood by taking a semi-classical, three-step approach first developed by Corkum[60], schematically illustrated in Fig. 1-9. In this model, the first step is tunnel ionization, in which the laser pulse's electric field is so intense that it will compete with and deform the atomic potential felt by the valence electrons of the noble gas such that they have a non-negligible probability of escaping the potential well they sit in. The interplay between electric field and the ionization potential of the atom is summarized by the Keldysh parameter[61],

$$\gamma = \frac{\omega\sqrt{2m_e I_p}}{eE}, \tag{1.29}$$

where ω is the angular frequency of the driving field, E is the field strength, m_e is the electron's mass and e is its charge, I_p is the ionization potential of the atom. Since the laser electric field is oscillatory, the barrier can only be lowered during individual cycles, this means that electrons must ionize on a timescale shorter than the inverse frequency of this oscillation, and thus lower frequency pulses are better for this process, i.e. $\gamma < 1$. This explains the use of near infrared and infrared driving fields for HHG. On the other hand, if the electric field frequency is high as well as being intense, i.e. $\gamma > 1$, the ionization potential can be reached by simply having enough of these photons interacting with the atom at once, leading to multiphoton ionization, which is not conducive to HHG. The tunneling probability can be calculated by the Ammosov-Delone-Krainov ionization model[62].

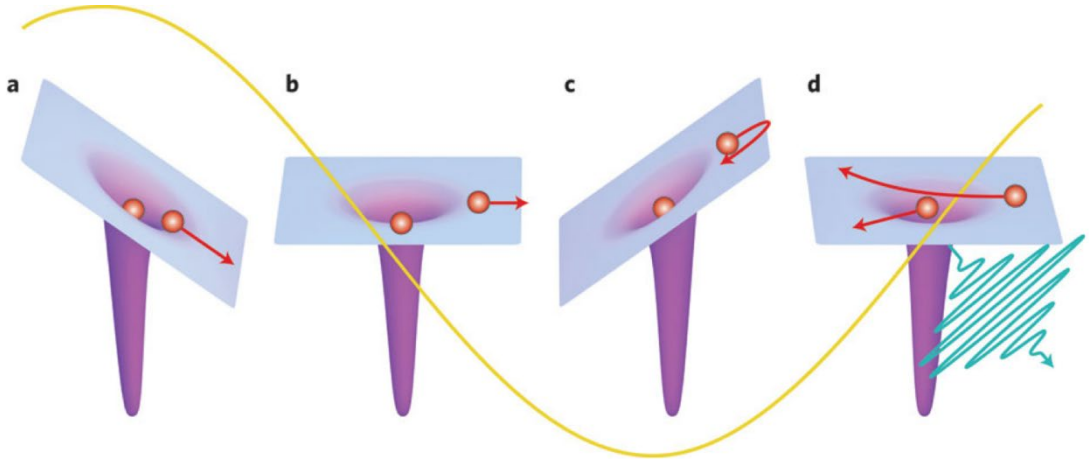

Figure 1-9: Schematic of the three-step model. (a) represents the tunnel ionization and the acceleration of the electron, (b) represents the turn-around point for the electron, (c) represents the acceleration of the electron back towards the parent atom, and (d) is the recombination step.

Step two corresponds to the acceleration of the recently freed electron in the presence of the electric field. Since the atomic potential is extremely weak compared to the laser field at any point

even slightly removed from the nucleus, the motion of the electron after ionization can be well described by a classically moving free electron in the presence of an electric field. It is also assumed that the initial velocity of the ionized electron is zero, but it turns out this is a valid assumption, so that the set of coupled equations describing the electron trajectory can be solved. It is found that there are multiple trajectories the electron can take, depending at which point in the cycle it was ejected, as seen in Fig. 1-10.

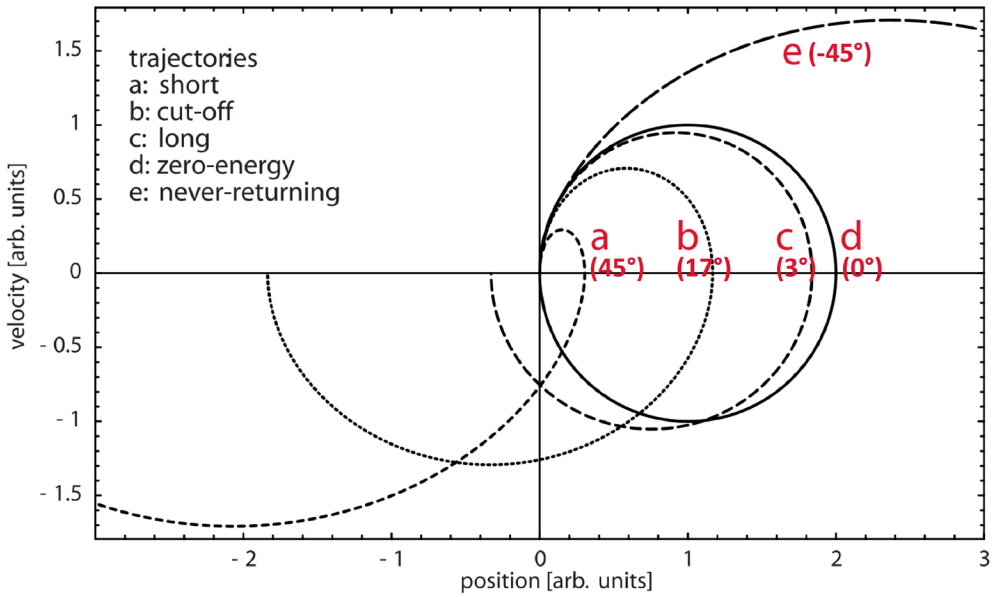

Figure 1-10: A plot of the velocity versus the position of an ejected electron for certain trajectories. The relative phase of each trajectory with respect to the electric field maximum is given in degrees. Adapted from Ref. 63. Of note, trajectories (a) and (c) return to the parent atom with the same velocity, despite very different trajectories.

It can be seen that some trajectories lead the electron astray, never to return, while electrons ejected at the electric field maximum, which also corresponds to the maximum tunneling probability, return to the parent atom with no kinetic energy. Thus, most trajectories do not contribute to the HHG process. Furthermore, there are two trajectories, one short and one long, which return the electron with the same kinetic energy. In any case, the total kinetic energy of the electron is simply the ionization potential plus the energy gained from accelerating in the field of the laser pulse. It is found that the maximum energy the electron can gain occurs at a trajectory with a relative phase of 17° with respect to the electric field maximum, and this is approximately given by the relation,

$$E_{kin} = I_p + 3.17U_p = I_p + 3.17\frac{e^2E^2}{4m_e\omega^2}, \tag{1.30}$$

where U_p is the ponderomotive energy of the electron in the presence of the field. This is essentially a cut-off energy for the HHG process, which can be overcome in several ways. First, the ionization potential can be increased, such as going to lighter noble gases. However, the difference in I_p

between them is not very large, only spanning 12.13 eV for Xe and 24.58 for He, which does not extend the range of kinetic energies very far. Also, a higher I_p means that the field strength needed for tunnel ionization will also increase. Next, the field strength can be increased, however this avenue is limited both by the Lorentz force, which can manifest at very high field strengths, and by phase matching conditions which will be discussed further below. Lastly, the driving field wavelength can be made longer. This avenue is limited quantum mechanically, specifically by the fact that the longer a free electron travels, the more diffuse its wavefunction becomes, which in turn will lower the probability of the electron recombining with its parent atom. Clearly, each individual dial has strengths and weaknesses, but by carefully adjusting them simultaneously, as well as taking the phase matching conditions into consideration, harmonics can be produced well into the soft x-ray regime[64], up to 1.6 keV.

The final step then is recombination of the free electron with its parent atom, which leads to the emission of a highly energetic photon. This process is inherently quantum mechanical as well, and must be calculated as such. In fact, a full quantum treatment of the three-step process was soon developed by Lewenstein[65]. It is important to note that in order for the recollision probability to be non-zero, the driving field must be linearly polarized. That is, ellipticity in the pulse will severely degrade the efficiency of the HHG process. However, it is possible to produce circularly polarized high order harmonics by using a two-color driving field[66] in which each pulse is circularly polarized with opposite directions, ensuring that the ionization will occur at the linear point in the total field.

An important prediction of the three-step model is that for a multi-cycle driving pulse, XUV emission will occur every half-cycle. This means that a single driving pulse will emit an XUV pulse train which has a periodicity of half a laser period, $T = \pi/\omega_{IR}$. Also, since each adjacent pulse in the train will be emitted with a different spectral sign, the interference between the XUV pulses in the pulse train will then lead to a spacing between them equal to $2\hbar\omega_{IR}$ in frequency space such that only odd-order harmonics are emitted, i.e. $\omega_{XUV} = (2n + 1)\omega_{IR}$. This limits the total energy coverage achieved, lowering the signal to noise ratio in the gaps between harmonic orders. However, there are some techniques which aim to overcome this limitation.

One way to accomplish this is by using few-cycle[67,68] or even single-cycle[69] driving pulses. In this way, the train of XUV pulses can become a few pulses or even a single pulse, minimizing the interference between them, leading to spectrally broader harmonics, in the extreme case, even creating a supercontinuum of photons, spanning several hundred eV. Not only is this beneficial in terms of energy coverage and spectral signal to noise, but a large bandwidth also means a shorter pulse duration. Thus, by using few cycle or single cycle driving pulses it is possible to generate XUV pulses in the attosecond regime.

Another way to widen the energy coverage of the high harmonic spectrum is to use a second, perturbative driving field in order to generate both even and odd order harmonics[70]. This is usually accomplished by generating a small amount of the second harmonic of the fundamental frequency and sending both frequencies collinearly onto the target medium. By adding the perturbative field, the overall field felt by the noble gas atom is no longer centrosymmetric, making it so XUV pulses

are no longer emitted every half cycle, instead they can only emit every full cycle. The net result is that each harmonic is spaced $\hbar\omega_{IR}$ apart in energy space. Not only does this technique generate both even and odd order harmonics, but it can also lead to a large improvement in the overall efficiency of the HHG process.

1.3.2 Phase Matching

Apart from this microscopic model, there are macroscopic considerations that determine the overall efficiency of the HHG process as well. The most important being that of phase matching[71] between the incident driving field and the generated high harmonics, across a significant portion of the gain medium. In other words, the phase velocity of the fundamental frequency must match that of the harmonics so that the emission from individual atoms remains coherent throughout the medium,

$$v_p^{IR} = v_p^{XUV}. \tag{1.31}$$

However, since the phase velocity depends on the frequency of the photon, $v_p = \omega_q/k$, each harmonic order, represented by q, would have a slightly different phase, leading to a phase mismatch between the driving field and certain harmonic orders. This is usually represented by the wave-vector mismatch given by,

$$\Delta k_q = qk_{IR} - k_{XUV}(q). \tag{1.32}$$

Thus, it is not possible to achieve perfect phase matching ($\Delta k_q = 0$) for all harmonic orders at the same time. As such, there is a length scale at which significant phase matching can occur within the medium without destructive interference dominating, this coherence length is given by,

$$L_{coh}(q) = \frac{\pi}{\Delta k_q} = \frac{2\pi c\omega_{IR}\varepsilon_0 m_e}{qn_e e^2}, \tag{1.33}$$

where c is the speed of light in a vacuum, ω_{IR} is the angular frequency of the driving field, ε_0 is the permittivity of free space, m_e is the electron mass, q is the harmonic order, n_e is the number density of electrons, and e is the electronic charge. It can be seen that this coherence length will decrease with increasing harmonic order as well as increasing electron number density. Thus, as the driving laser becomes more intense, ionizing more electrons, the coherence length decreases, making the HHG process less efficient, but using longer wavelengths will improve it.

There are also other sources of phase mismatch. For example, in order to reach the high intensities needed for HHG, the driving laser is usually tightly focused into the gas medium. In this case, the Gouy phase shift at the focus position must be taken into account. However, this can often be neglected by using a loose focus, or by using a hollow core waveguide. A more important source of phase mismatch comes from the fact that the neutral gas and the ionized gas will have different dispersion relations, thus the total wave vector can be given by,

$$\Delta k = \Delta k_N + \Delta k_{Pl} + \Delta k_G = -\frac{2\pi q}{\lambda_0}\frac{P}{P_{atm}}\delta_n(1-\eta) + q\eta N_{atm} r_e \lambda_0 \frac{P}{P_{atm}} - \frac{q\lambda_0}{\pi\omega_0^2}, \tag{1.34}$$

where λ_0 and ω_0 are the wavelength and angular frequency of the driving field, P/P_{atm} is the ratio of the gas pressure to the atmospheric pressure, δ_n is the difference in index of refraction between the fundamental and harmonic frequency, η is the fraction of ionized gas, r_e is the classical electron radius, and N_{atm} is the atomic number density. It is serendipitous that the mismatch due to the neutral gas and the mismatch due to the plasma have opposite signs, thus they can cancel each other out. It can be seen that the phase matching conditions are dependent on the gas pressure, as well as the fraction of ionized gas. Thus, the interplay between the intensity of the driving field and the gas pressure can be used to tune the efficiency of the HHG process.

This phase matching condition is further limited by the fact that the neutral gas medium will also absorb the newly created XUV frequencies. Therefore, another crucial relationship is the length between the interaction length L_{int} and the absorption length L_{abs}. The absorption length is given by,

$$\mathrm{L}_{abs} = \frac{1}{\sigma\rho}, \tag{1.35}$$

where σ is the ionization cross section and ρ is the gas density. It has been found that in order to optimize the HHG process, the following relationships between the coherence length and the interaction length must hold[72],

$$\mathrm{L}_{int} > 3\mathrm{L}_{abs}, \quad \mathrm{L}_{coh} > 5\mathrm{L}_{abs}. \tag{1.36}$$

This ensures that the macroscopic response is at least half the maximum possible response for the HHG process. Once again, the ionization rate is crucial in order to reach favorable phase matching conditions.

The rest of this dissertation is organized as follows: Chapter 2 describes the layout, as well as several upgrades made to, the experimental apparatus used to perform the scientific investigations into the excited state dynamics of solids done during the course of this thesis. Chapter 3 describes the time-resolved excited state dynamics of α-Fe_2O_3 following photoexcitation with 4 different excitation wavelengths (400 nm, 480 nm, 520 nm, and 560 nm), including small polaron formation dynamics and its impact on the photoconversion efficiency of α-Fe_2O_3 based photoelectrochemical cells. Chapter 4 describes the excited state dynamics of single crystalline Si thin films following photoexcitation by an 800 nm pump pulse. The electron-phonon scattering dynamics following photoexcitation are observed through the vantage point of the Si $2p$ core level absorption, demonstrating the strengths and unique capabilities of pump probe spectroscopy performed with high harmonic generation.

1.4 Bibliography

1. Seidl, R. *et al.* Forest disturbances under climate change. *Nat. Clim. Chang.* **7**, 395–402 (2017).

2. Stern, N. *Stern review: the economics of climate change*. (2006).

3. Change, I. P. on C. *Climate change 2014: Mitigation of climate change*. (Cambridge University Press, 2015).

4. Rühle, S. Tabulated values of the Shockley-Queisser limit for single junction solar cells. *Sol. Energy* **130**, 139–147 (2016).

5. Smith, C. & Barron, A. Synthesis and Purification of Bulk Semiconductors. (2012).

6. Pizzini, S. Towards solar grade silicon: Challenges and benefits for low cost photovoltaics. *Sol. Energy Mater. Sol. Cells* **94**, 1528–1533 (2010).

7. Murphy, A. B. *et al.* Efficiency of solar water splitting using semiconductor electrodes. *Int. J. Hydrogen Energy* **31**, 1999–2017 (2006).

8. Qiu, Y. *et al.* E ffi cient Photoelectrochemical Water Splitting with Ultrathin fi lms of Hematite on Three-Dimensional Nanophotonic Structures. *Nano Lett.* **14**, 2123–2129 (2014).

9. Kudo, A. & Miseki, Y. Heterogeneous photocatalyst materials for water splitting. *Chem. Soc. Rev.* **38**, 253–278 (2009).

10. Lindenberg, A. M. *et al.* Time-resolved X-ray diffraction from coherent phonons during a laser-induced phase transition. *Phys. Rev. Lett.* **84**, 111–114 (2000).

11. Harb, M. *et al.* Electronically driven structure changes of Si captured by femtosecond electron diffraction. *Phys. Rev. Lett.* **100**, 1–4 (2008).

12. Harb, M. *et al.* Carrier relaxation and lattice heating dynamics in silicon revealed by femtosecond electron diffraction. *J. Phys. Chem. B* **110**, 25308–25313 (2006).

13. Ferray, M. *et al.* Multiple-harmonic conversion of 1064 nm radiation in rare gases. *J. Phys. B At. Mol. Opt. Phys.* **21**, (1988).

14. McPherson, A. *et al.* Studies of multiphoton production of vacuum-ultraviolet radiation in the rare gases. *J. Opt. Soc. Am. B* **4**, 595 (1987).

15. Richter, A., Hermle, M. & Glunz, S. W. Reassessment of the limiting efficiency for crystalline silicon solar cells. *IEEE J. Photovoltaics* **3**, 1184–1191 (2013).

16. Dimroth, F. *et al.* Four-junction wafer-bonded concentrator solar cells. *IEEE J. Photovoltaics* **6**, 343–349 (2016).

17. Green, M. A. *Third Generation Photovoltaics: Advanced Solar Energy Conversion*. (Springer, 2003).

18. Queisser, H. J. Multiple carrier generation in solar cells. *Sol. Energy Mater. Sol. Cells* **94**, 1927–1930 (2010).

19. Mauerer, M., Shumay, I. L., Berthold, W. & Höfer, U. Ultrafast carrier dynamics in Si(111)7×7 dangling bonds probed by time-resolved second-harmonic generation and two-photon photoemission. *Phys. Rev. B - Condens. Matter Mater. Phys.* **73**, 1–8 (2006).

20. Ulbricht, R., Hendry, E., Shan, J., Heinz, T. F. & Bonn, M. Carrier dynamics in semiconductors studied with time-resolved terahertz spectroscopy. *Rev. Mod. Phys.* **83**, 543–586 (2011).

21. Van Der Laan, G. M2,3 absorption spectroscopy of 3d-transition metal compounds. *J. Phys. Condens. Matter* **3**, (1991).

22. Qiao, R., Chin, T., Harris, S. J., Yan, S. & Yang, W. Spectroscopic fingerprints of valence and spin states in manganese oxides and fluorides. *Curr. Appl. Phys.* **13**, 544–548 (2013).

23. Vura-Weis, J. *et al.* Femtosecond $M_{2,3}$-edge spectroscopy of transition-metal oxides: Photoinduced oxidation state change in α-Fe_2O_3. *J. Phys. Chem. Lett.* **4**, 3667–3671 (2013).

24. Huse, N. *et al.* Ultrafast Spin-State Conversion in Solvated Transition Metal Complexes Probed with Femtosecond Soft X-Ray Spectroscopy. *Int. Conf. Ultrafast Phenom.* TuD2 (2010).

25. De Groot, F. Multiplet effects in X-ray spectroscopy. *Coord. Chem. Rev.* **249**, 31–63 (2005).

26. De Groot, F., Kotani, A. *Core Level Spectroscopy of Solids*. (CRC Press, 2008).

27. Ballhausen, C. J. *Molecular Electronic Structure of Transition Metal Complexes*. (McGraw-Hill, 1980).

28. Tanabe, Y., Sugano, S. On the Absorption Spectra of Complex Ions. I. *J. Phys. Soc. Japan* **9**, 753 (1954).

29. Krüger, P. Ab initio calculation of ligand field multiplet parameters for transition metal L-edge spectra. *Radiat. Phys. Chem.* 0–1 (2018).

30. Bagus, P. S. & Ilton, E. S. Effects of covalency on the p -shell photoemission of transition metals: MnO. *Phys. Rev. B - Condens. Matter Mater. Phys.* **73**, 1–14 (2006).

31. Rehr, J. J.,Kas, J.J.,Vila, F.D., Prange, M. P., Jorissen, K. Parameter-free calculations of x-ray spectra with FEFF9. *Physiscal Chem. Chem. Phys.* **12**, 5503 (2010).

32. Rehr, J. J., Kas, Prange, M. P., Sorini, A. P., Takimoto, Y. Ab initio theory and calculations of X-ray spectra. *Comptes Rendus Phys.* **10**, 548 (2009).

33. Rehr, J. J., Albers, R. C. Theoretical Approaches to X-ray Absorption Fine Structure. *Rev. Mod. Phys.* **72**, 621 (2000).

34. Gilmore, K. *et al.* Efficient implementation of core-excitation Bethe-Salpeter equation calculations. *Comput. Phys. Commun.* **197**, 109–117 (2015).

35. Vinson, J., Rehr, J. J., Kas, J. J. & Shirley, E. L. Bethe-Salpeter equation calculations of core excitation spectra. *Phys. Rev. B - Condens. Matter Mater. Phys.* **83**, (2011).

36. Qteish, A. Role of semicore states in the electronic structure of group-III nitrides : An

exact-exchange study. 1–8 (2005).

37. Wang, Z. & Bevan, K. H. Exploring the impact of semicore level electronic relaxation on polaron dynamics: An adiabatic ab initio study of $FePO_4$. *Phys. Rev. B* **93**, 024303 (2016).

38. Bosman, A. J. & van Daal, H. J. Small-polaron versus band conduction in some transition-metal oxides. *Adv. Phys.* **19**, 1–117 (1970).

39. Ashcroft, N. W., Mermin, N. D. *Solid State Physics*. (Saunders College, 1976).

40. Kittel, C. *Introduction to Solid State Physics* (John Wiley & Sons, 2005).

41. Lany, S. Semiconducting transition metal oxides. *J. Phys. Condens. Matter* **27**, 283203 (2015).

42. Mott, N. F. *Metal-insulator Transitions*. (Taylor and Francis, 1974).

43. Quackenbush, N. F. *et al.* Nature of the Metal Insulator Transition in Ultrathin Epitaxial Vanadium Dioxide. *Nano Lett.* **13**, 4857–4861 (2013).

44. Devreese, J. T. & Alexandrov, A. S. Fröhlich polaron and bipolaron: recent developments. *Reports Prog. Phys.* **72**, 66501 (2009).

45. Landau, L. D. Über die Bewegung der Elektronen in Kristalgitter. *Phys. Z. Sowjetunion* **3**, 644–645 (1933).

46. Emin, D. & Kriman, A. M. Transient small-polaron hopping motion. *Phys. Rev. B* **34**, 7278–7289 (1986).

47. Lu, N., Li, L., Geng, D. & Liu, M. A review for polaron dependent charge transport in organic semiconductor. *Org. Electron.* **61**, 223–234 (2018).

48. Fröhlich, H. Electrons in lattice fields. *Adv. Phys.* **3**, 325–361 (1954).

49. Holstein, T. Studies of polaron motion. *Ann. Phys. (N. Y).* **8**, 325–342 (1959).

50. Katz, J. E. *et al.* Electron Small Polarons and Their Mobility in Iron (Oxyhydr)oxide Nanoparticles. *Science (80-.).* **337**, 1200–1203 (2012).

51. Lee, J. *et al.* The influence of charge and magnetic order on polaron and acoustic phonon dynamics in $LuFe_2O_4$. *Appl. Phys. Lett.* **107**, (2015).

52. Stoneham, A. M. Small polarons and polaron transitions. *J. Chem. Soc. Faraday Trans. 2* **85**, 505 (1989).

53. Feng, Z. *et al.* Dynamics of polaron formation in Li_2O_2 from density functional perturbation theory. *Phys. Rev. B* **88**, 184302 (2013).

54. Morin, F. J. Electrical Properties of a-Fe2O3. *Phys. Rev.* **93**, 1195–1199 (1954).

55. Canali, C., Jacoboni, C., Nava, F., Ottaviani, G. & Alberigi-Quaranta, A. Electron drift velocity in silicon. *Phys. Rev. B* **12**, 2265–2284 (1975).

56. Shah, J. *Ultrafast Spectroscopy of Semiconductors and Semiconductor Nanostructures*. (Springer, 1999).

57. McDonald, C. R., Vampa, G., Orlando, G., Corkum, P. B. & Brabec, T. Theory of high-harmonic generation in solids. *J. Phys. Conf. Ser.* **594**, 12021 (2015).

58. Luu, T. T. *et al.* Extreme–ultraviolet high–harmonic generation in liquids. *Nat. Commun.* **9**, 1–10 (2018).

59. Ganeev, R. A. High-order harmonic generation in a laser plasma: a review of recent achievements. *J. Phys. B At. Mol. Opt. Phys.* **40**, R213 (2007).

60. Corkum, P. B. Plasma Perspective on Strong-Field Multiphoton Ionization. *Phys. Rev. Lett.* **71**, 1994–1997 (1993).

61. Keldysh, L. V. Ionization in the Field of a Strong Electromagnetic Wave. *J. Exp. Theor. Phys.* **20**, 1307–1314 (1965).

62. Ammosov, M. V., Delone, N. B., Krainov, V. P. Tunnel ionization of complex atoms and of atomic ions in an alternating electromagnetic field. *Sov. Phys. JETP* **64**, 1191–1194 (1986).

63. Winterfeldt, C., Spielmann, C. & Gerber, G. Colloquium: Optimal control of high-harmonic generation. *Rev. Mod. Phys.* **80**, 117–140 (2008).

64. Popmintchev, T. *et al.* Bright Coherent Ultrahigh Harmonics in the keV X-ray Regime from Mid-Infrared Femtosecond Lasers. *Science (80-.).* **336**, 1287–1291 (2012).

65. Lewenstein, M., Balcou, P., Ivanov, M. Y., L'Huillier, A. & Corkum, P. B. Theory of high-harmonic generation by low-frequency laser fields. *Phys. Rev. A* **49**, 2117–2132 (1994).

66. Kfir, O. *et al.* In-line production of a bi-circular field for generation of helically polarized high-order harmonics. *Appl. Phys. Lett.* **108**, (2016).

67. Morishita, T., Le, A.-T., Chen, Z. & Lin, C. D. Accurate Retrieval of Structural Information from Laser-Induced Photoelectron and High-Order Harmonic Spectra by Few-Cycle Laser Pulses. *Phys. Rev. Lett.* **100**, 13903 (2008).

68. Goulielmakis, E. *et al.* Real-time observation of valence electron motion. *Nature* **466**, 739–743 (2010).

69. Goulielmakis, E. *et al.* Single-Cycle Nonlinear Optics. **320**, 1614–1618 (2008).

70. Kim, I. J. *et al.* Highly efficient high-harmonic generation in an orthogonally polarized two-color laser field. *Phys. Rev. Lett.* **94**, 2–5 (2005).

71. Balcou, P. & L'Huillier, A. Phase-matching effects in strong-field harmonic generation. *Phys. Rev. A* **47**, 1447–1459 (1993).

72. Heyl, C. M., Arnold, C. L., Couairon, A. & L'Huillier, A. Introduction to macroscopic power scaling principles for high-order harmonic generation. *J. Phys. B At. Mol. Opt. Phys.* **50**, (2017).

Chapter 2

Description of and Upgrades to Experimental Apparatus for Extreme Ultraviolet Femtosecond Transient Absorption

The work in this thesis was performed on a table-top transient XUV absorption apparatus discussed in this chapter. The chapter is separated into several sections describing different aspects, as well as upgrades made to the apparatus. The first subsection discusses the commercial laser system used to generate the high energy pulses needed for high harmonic generation, along with certain notes on its long-term maintenance. Second, the optical layout of the apparatus is discussed in section 2.2, and this is separated into the pump and probe paths, along with the major upgrades done to the apparatus. Finally, possible future upgrades that will improve the capabilities of the current system are discussed in section 2.3.

2.1 Ultrafast laser system

2.1.1 Chirped Pulse Amplifier System

In order to study the ultrafast dynamics of solid-state materials a commercial laser system is employed along with home-built sections to generate extreme ultraviolet high order harmonics, overlap pump and probe, and spectrally resolve the transient absorption in the extreme ultraviolet. A high powered, stable infrared laser source is required to generate high harmonic pulses reliably. The laser system is composed of a commercial chirped pulse regenerative amplifier (Spitfire Pro XP, Spectra Physics), which is seeded by a Ti:Sapphire oscillator (Tsunami, Spectra Physics) and also pumped by a Q-switched Nd:YLF laser (Empower 30, Spectra Physics). The oscillator itself is pumped by a continuous wave (CW) 532 nm diode laser (Millennia, Spectra Physics). About 3.9 W of the green CW laser is sent into the oscillator and converted to the near-infrared (NIR) wavelength of 800 nm by passing through a Ti:Sapphire crystal. The laser then makes its way through an acousto-optic modulator (AOM), which is used to actively mode-lock the laser and create pulses. Two prisms controlled by a micrometer are used to induce negative dispersion to compensate for the positive dispersion generated by the Ti:Sapphire crystal and the AOM. When the oscillator is mode-locked properly, the spectral bandwidth of the pulses is ~75 nm, leading to 3 nJ, 35 fs pulses centered at 800 nm, at an 80 MHz repetition rate.

The pulses are then directed into the Spitfire where they are first stretched by making multiple passes through a diffraction grating, inducing a positive chirp to them and leading to pulses that are ~100 ps in duration. This must be done because the pulses become over one million times more energetic in the amplifier cavity, and if the pulses remain close to their transform limit, they can reach peak intensities that are high enough to induce the self-focusing effect of Kerr lensing in the gain medium, resulting in damage to the regenerative amplifier. After the stretcher, the pulses are then directed into the regenerative amplifier cavity. The cavity is controlled by a set of two Pockel's cells (PC's). When the first PC is turned on, it will convert a pulse from horizontal to vertical polarization and the pulse will pass through a thin film polarizer, which allows the pulse into the cavity, otherwise the pulses are rejected. The second PC is behind the Ti:Sapphire gain medium and it will turn on to convert the pulse back to horizontal polarization, trapping the pulse in the cavity. After the pulse makes a few round trips through the cavity, reaching its maximum amplification, both PC's will turn off and allow the amplified pulse to exit the cavity. The gain medium itself is pumped by the Q-switched pulses from the Empower, which synchronizes the PC's to a 1 kHz repetition rate. The amplified pulses then make their way to the compressor section, where they make multiple passes through another diffraction grating, this time inducing negative chirp to bring the pulse duration back close to its transform limit. A retroreflector, which allows the pulse to make several trips across the compressor grating, is controlled through a computerized motor, giving fine control of the chirp of the pulses. When the amplifier is optimized, the pulse energy can reach ~3.5 mJ and the spectrum of the pulses coming out of the chirped pulse amplifier has been measured to be at ~40 nm FWHM centered at ~800 nm.

2.1.2 Notes on Long-Term Maintenance

This section details some notes on the maintenance of the commercial laser system that have been gathered throughout the course of the work performed in this thesis, which do not appear in the service manuals for the lasers. The commercial laser system used in this lab was manufactured in the early 2000s, and although these systems are built to be robust and stable over many years, certain parts are prone to damage or instability over time. The net effect from these instabilities is usually a decrease in the laser output power, and diagnosing the source of the decrease can involve checking many different parts of the system. Usually, when the output power of a laser system goes down, it is safe to assume this is due to a misalignment. However, when small adjustments to the alignment do not bring the output power back to its optimal level, it is helpful to know where the failures usually take place. The following paragraphs will be ordered from the most likely cause, requiring more frequent maintenance, to the least likely, which requires less maintenance.

First, due to the high peak powers reached in the compression section of the Spitfire amplifier, the compression grating itself is prone to damage. This occurs because dust or other debris in the air can be burned onto the grating surface where the peak power is highest, in turn leading to decreased reflectivity. Thus, keeping the lab clean and free from dirt is imperative, but even still, dirt buildup on optics will occur over time. This issue is known to Spectra-Physics, and their recommendation has been to clean the grating surface regularly with de-ionized water. A bright flashlight can be used to more clearly see if there is any damage. A dark spot should be clearly visible on the grating surface at the point where the pulses make their last pass by the grating

before exiting the compressor, corresponding to the top right corner. The procedure performed and recommended by the Spectra-Physics service technicians is as follows: Keep the grating in place so as to not disturb the alignment, place several absorbent paper towels, or another highly absorbent material, underneath the grating, use a squirt bottle with pure, de-ionized water (18.2 MΩ·cm resistivity) to wet the grating surface starting from the top of the grating so that the water flows down along the grating grooves, then immediately blow dry the grating using dry nitrogen gas from the same point at which the water was applied. The procedure may be repeated if needed. If water cleaning does not produce the desired results, clean, dry methanol may also be attempted.

Second, due to the compact, folded cavity design of the Tsunami oscillator, several of its optics face upwards, making them more prone to dust build up, the most important among these being the Ti:Sapphire gain medium itself. A clear indicator that the crystal needs cleaning is if there is too much green pump light scattering from it, as shown in Fig. 2-1a. Once cleaned, the scattered light should decrease significantly, as shown in Fig. 2-1b, leading to higher output power from the Tsunami. Since the crystal mount protrudes around the faces of the crystal, and the crystal itself has a very small diameter (<1 cm), it is not practical to use lens tissue, instead a nonabrasive cotton swab is recommended. When cleaning the gain medium, it is also prudent to clean the other optics that are more prone to dust build-up such as the prisms, pump mirrors 1 and 2, and mirrors 6 and 7.

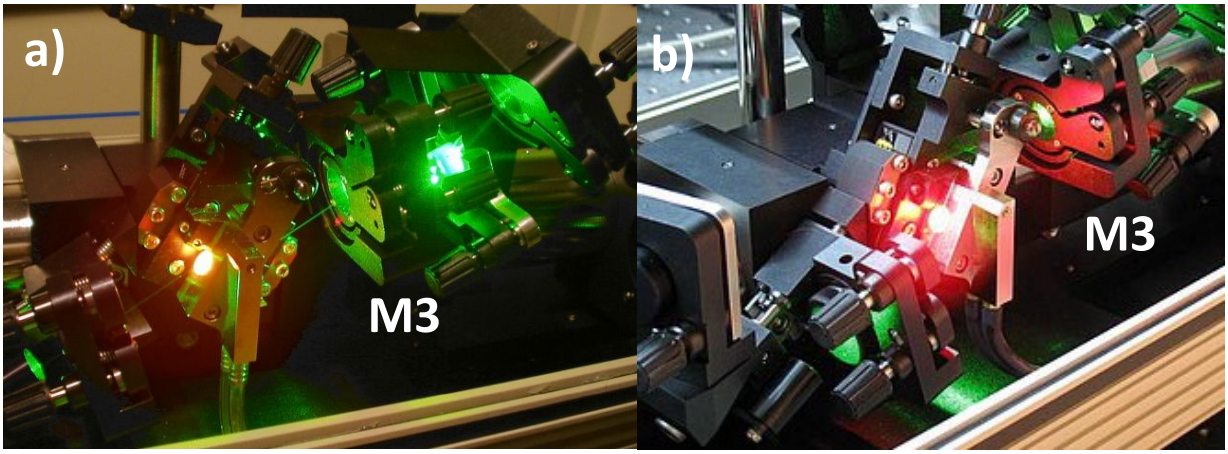

Figure 2-1: (a) Detail of the Tsunami oscillator cavity. The Ti:Sapphire gain medium appears yellowish due to pump light scattering from dust build-up on the crystal faces. Green light from pump scatter is especially obvious on M3 housing. (b) Detail of the Tsunami oscillator gain medium when it is clean, showing very little pump light scatter coming from the gain medium. Note almost no green light back-scattering onto M3, only fluerscence from the gain medium.

Third, the Empower laser head is composed of a central Nd:YLF rod used as the gain medium, along with four diode lasers connected in series used to pump the gain medium. Over time, the performance of the diodes will decrease and the current supplied to them may be increased in order to compensate for this. However, after many hours of operation at these higher currents, it is possible for the electrical connections between the diodes to degrade as well, due to soot build-up. This can perpetuate a cycle of decreasing performance and increasing current to compensate. In the case where the Empower performance has degraded significantly, it may be useful to check

the electrical connections of the diodes in the laser head for soot build-up. The connectors should naturally be a gold color. If there is a significant amount of soot built-up, the diodes can be removed and the connectors may be cleaned by using fine grit sand paper to brush away the soot and cleaned with dry methanol. When removing and replacing the diodes, care must be taken not to bend the connectors too far, otherwise they will not make contact the diodes when they are put back in.

2.2 Optical Layout

The entire laser system is composed of several sections, with two separate paths for the pump and probe beams, illustrated in Fig. 2-2. After exiting the amplifier, the laser is directed onto a 40% reflectivity beam splitter which splits the beam into the pump and probe paths. About 2 mJ is sent towards the high harmonic generation (HHG) chamber forming the probe path, while the remaining 1.5 mJ can be sent either into an optical parametric amplifier or through another path where it can either be sent unmodified into the sample chamber, or it can be converted to other wavelengths either through second and third harmonic generation of the fundamental, or through other parametric processes after entering an optical parametric amplifier (OPA).

Several updates to the laser system were performed during the course of the work in this thesis which will be outlined in the following subsections. Section 2.2.1 details a new, in-line configuration for generating two-color high harmonics. Section 2.2.2 describes the new beam stabilization system used on the probe beam to stabilize the HHG process. Section 2.2.3 describes the use of a new microchannel plate filter to remove the residual driving fields used for HHG. Section 2.2.4 describes a new way to mitigate sample damage caused by heating of the sample, by using jets of cold N_2 gas to cool the samples. Section 2.2.5 describes the spectrometer chamber. Section 2.2.6 describes the pump beam path, including upgrades to the commercial OPA system, which increased the available wavelength range and also improved the beam quality for the sum frequency generation wavelengths.

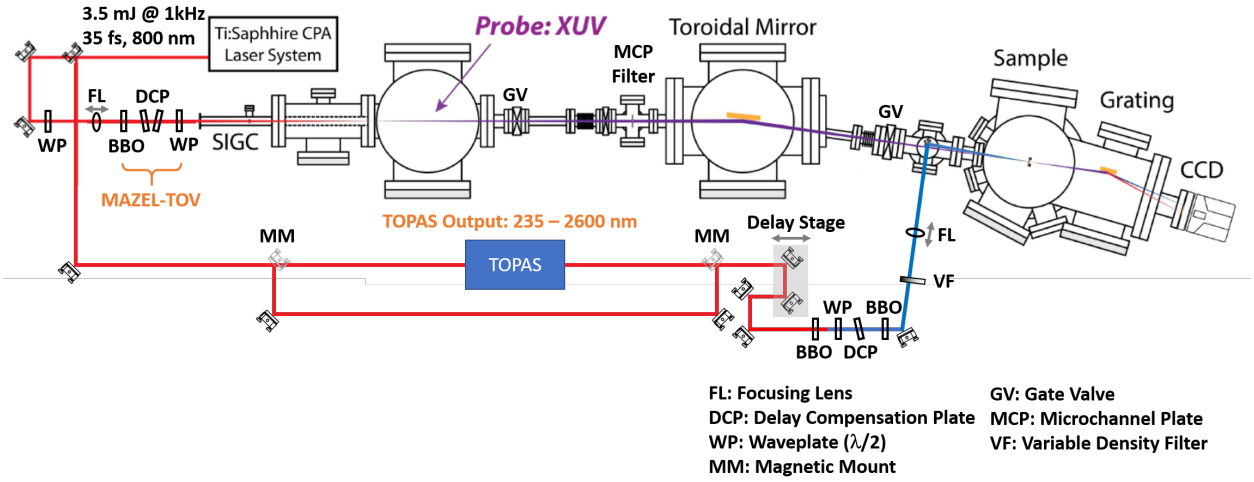

Figure 2-2: Schematic diagram of the table-top XUV transient absorption experimental apparatus. The MAZEL-TOV is the new in-line configuration used to generate the second harmonic of the fundamental frequency for high-harmonic generation.

2.2.1 Two-Color High Harmonic Generation

The 2 mJ portion of the pulse that transmits through the beam splitter is directed towards the HHG chamber. High harmonic generation is usually driven by a near infrared pulsed laser, such as that from a Ti:Sapphire amplifier, leading to discrete odd-order harmonic peaks. However, a two-color driving field can be used to produce both even and odd order harmonics to increase the energy coverage, with the second harmonic of the fundamental being used as a perturbative field[1]. At the beginning of this Ph.D., this was accomplished by further splitting the probe beam with a 90% reflectivity beam splitter (BS1-800-90-1004-45P, CVI). The reflected portion of the beam was focused into a semi-infinite gas cell (SIGC) by a 700 mm focal length fused silica spherical lens (PLCX-25.4-360.6-UV-670-1064, CVI) mounted on a 1" travel translational stage, allowing for precise control of the focus position of the 800 nm fundamental driving field into the SIGC. The 200 μJ portion of the pulse that was transmitted through the beam splitter was focused by a 500 mm focal length spherical lens into a 200 μm thick type-I BBO ($\theta = 29.2°$) frequency doubling it to 400 nm, with about 15% conversion efficiency. The second harmonic pulses were then converted back to horizontal polarization by a zero-order half-waveplate (QWPO-400-08-2-R10, CVI). Lastly, the second harmonic is focused with another 700 mm focal length spherical lens and recombined with the fundamental frequency beam collinearly through a 1 mm thick dichroic mirror (BSR-48-1004, CVI). The arrival time of the second harmonic pulse relative to the fundamental pulse was manually controlled by a delay stage in the 400 nm beam path.

This method for generating a two-color driving field is similar to a Mach-Zehnder interferometer and so it is susceptible to both spatial and temporal walk-off between the two beams throughout the day. Since HHG is a highly non-linear process, even very small deviations between the two pulses could severely degrade the high harmonic spectrum. If checked daily, the walk-off was small enough that optimization could be done by simply adjusting the spatial overlap and the delay stage while imaging the harmonics in real time. However, if the walk-off was significant such that the even harmonics were not present, it became necessary to either image the fundamental and second harmonic beams separately on a webcam and overlap them spatially, or to use a type-I BBO ($\theta = 44.3°$) along with a spectrometer to generate the third harmonic by combining the fundamental and second harmonic beams, using the delay stage to overlap them temporally. To improve the beam pointing stability, robust stainless-steel posts were used and a pair of active beam stabilization mirror mounts were purchased, using one stabilizing mirror each for the fundamental and the second harmonic beams. However, since the pulses are on the order of tens of femtoseconds, a difference of even 100 μm between the two beam paths can cause the pulses to lose temporal overlap, so even with active beam stabilization, the temporal overlap still needs to be adjusted throughout the day. Therefore, a more robust method for generating the two-color high harmonics was desired. To that end, a new configuration was found that could produce two-color HHG by using a compact in-line apparatus shown in Fig. 2-3. This method was dubbed the MAZEL-TOV (MAch-ZEhnder-Less for Threefold Optical Virginia spiderwort) apparatus and was designed for the purpose of creating circularly polarized high harmonics[2]. While circularly polarized harmonics were not created for the work presented in this thesis, the current setup would only need to replace the second half-wave plate with a quarter-wave plate in order to do so. Of

note, the unusual name comes from the fact that circularly polarized high harmonics have a spatial profile that has the same threefold symmetry as a Virginia Spiderwort flower[3], as seen in Fig. 2-4.

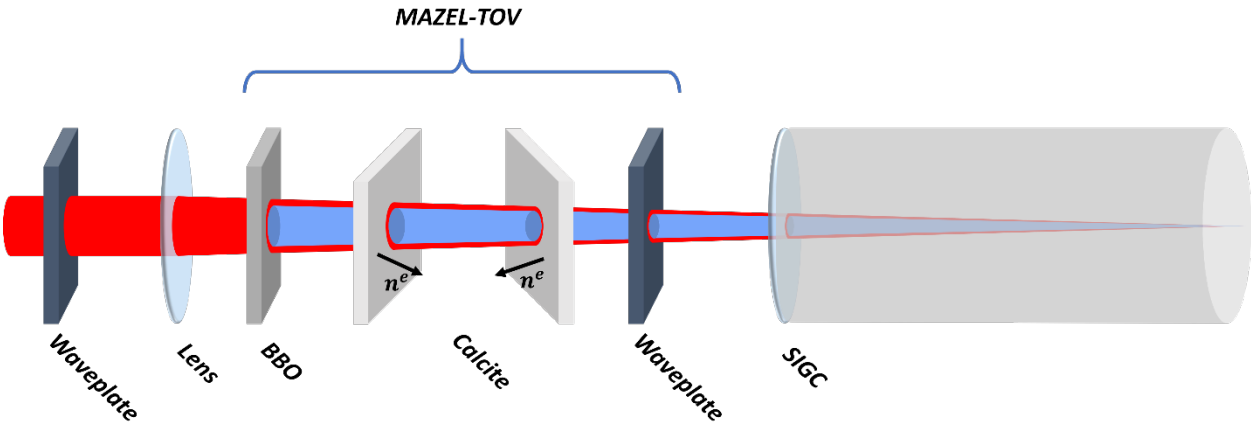

Figure 2-3: Schematic diagram for the MAZEL-TOV configuration used to generate the in-line second harmonic of the fundamental driving field for high-harmonic generation. A half-waveplate is placed before the lens to ensure that the final polarization of the HHG is in the desired polarization (horizontal). The calcite plates are used to compensate for the delay between the two driving fields induced by the BBO, second waveplate and SIGC entrance window. Two plates are used with inward facing optic axes in order to compensate for beam walk-off.

Figure 2-4: The unusual origin for the MAZEL-TOV acronym comes from the fact that the electric field vector (left) for the circularly polarized harmonics have the same threefold symmetry as the Virginia Spiderwort flower (right).

In order to achieve the current probe beam path, the 90% reflectivity beam splitter was replaced with an 800 nm high reflectivity mirror, allowing the full 2 mJ pulse energy to be directed towards the SIGC. The 200 μm type-I BBO ($\theta = 29.2°$) was moved to be an inch after the lens, partially converting the 800 nm pulse to its second harmonic frequency. This way, both wavelengths are focused colinearly into the SIGC, eliminating the need to align two separate beams. After the BBO, two calcite plates (TDC12102-AR, Newlight Photonics) are used to compensate for the delay between the fundamental and second harmonic induced by the BBO, waveplate, and fused silica SIGC window. Lastly, a zero-order dual wavelength waveplate (WPD03-H800-F400-SP, Newlight Photonics) is used to bring the 800 nm pulse polarization back

to the horizontal direction while keeping the 400 nm polarization unchanged. It is shown in the diagram in Fig. 2-3 that the fundamental pulses are first rotated from horizontal to vertical polarization using a zero-order half-waveplate (WPS03-H-800, Newlight Photonics) before entering the MAZEL-TOV. There are a few reasons for this. First, since the BBO used is of a type I configuration, the fundamental and second harmonic will have perpendicular polarizations after exiting it. Therefore, the polarization of one of the two pulses must be rotated to match the other. Also, it is highly desirable to only use zero-order waveplates as any higher order can lead to some ellipticity in the pulses, which in turn will degrade the HHG process. However, the zero-order wave plates available on the market can only impart a λ/2 phase shift to the 800 nm pulses while giving a full λ phase shift to the 400 nm pulses, and not the other way around. Therefore, if this were the only waveplate used, the beams would both end up polarized in the vertical direction, but the gold coated toroidal mirror used to focus the high harmonics has better reflectivity in the horizontal polarization than vertical polarization.

One drawback of the current setup is that the 200 μm BBO used is too thick, leading to a lower resolution for the harmonic output to the spectrometer, which is explained here in detail and summarized at the end of the paragraph. The reason for this drawback is that, at this thickness, the second harmonic conversion efficiency is too high. Even assuming the same 15% conversion efficiency would lead to ~300 μJ of second harmonic energy, which is 10 times more energy than is needed to perturb the fundamental driving field. This means that the 400 nm field is no longer in the perturbative regime and begins to compete with the 800 nm field to drive the HHG process. Thus, even if both the 800 nm and 400 nm pulses arrive at the same time and with the same polarization at the focus position, no even harmonics can be generated. While a thinner BBO would lead to a lower conversion efficiency, one was not immediately available. Alternatively, it was found that by rotating the BBO slightly around the surface normal, the second harmonic conversion efficiency could be lowered enough so that both even and odd high harmonics were produced. However, since BBO is a birefringent crystal, light propagating in a polarization direction that is perpendicular to the optical axis (OA) of the crystal, called the ordinary wave, will have refractive index n^o, while the part of the light that is propagating in the parallel direction to the OA experiences a separate refractive index, n^e.[4] The difference between these values, $\Delta n = n^e - n^o$, is the birefringence of the material, while the values depend on the wavelength of the incident light according to the Sellmeier equations[5]. Although n^o does not depend on the angle made between the incident beam and the OA, n^e does. At normal incidence n^e will depend on the angle, θ, made between the surface normal and the OA, given by the equation[6],

$$\frac{1}{n^e(\theta)^2} = \left(\frac{cos^2(\theta)}{(n^o)^2} + \frac{sin^2(\theta)}{(n^e)^2}\right)^{-1}. \tag{2.1}$$

As long as $\theta \neq 0$ or 90°, the extraordinary wave will have a different refractive index than the ordinary wave, leading to different propagation directions between the extraordinary and ordinary beams, as seen in Fig. 2-5. However, although the extraordinary wave's k-vector direction follows Snell's law, the same as the ordinary wave, the Poynting vector for the extraordinary wave will travel at an angle, ρ, instead given by the equation[6],

$$tan\rho = \frac{n^e(\theta)^2}{2}\left(\frac{1}{(n^e)^2} - \frac{1}{(n^o)^2}\right) sin(2\theta). \quad (2.2)$$

This walk-off effect can lead to spatially separate ordinary and extraordinary pulses, depending on the angle made between the extraordinary wave and the OA. Thus, the effect of rotating the BBO is that some of the incident light will now be polarized in the extraordinary direction, leading to some polarization impurity. The effect of this walk-off can be seen in the harmonic spectrum in Fig. 2-6, where each harmonic is doubled, with the copy appearing slightly offset on the camera. The net effect being a slight decrease in the high harmonic spectral resolution compared to the previous configuration. Nevertheless, this in-line method for producing high harmonics was much more stable than the previous interferometer-like method.

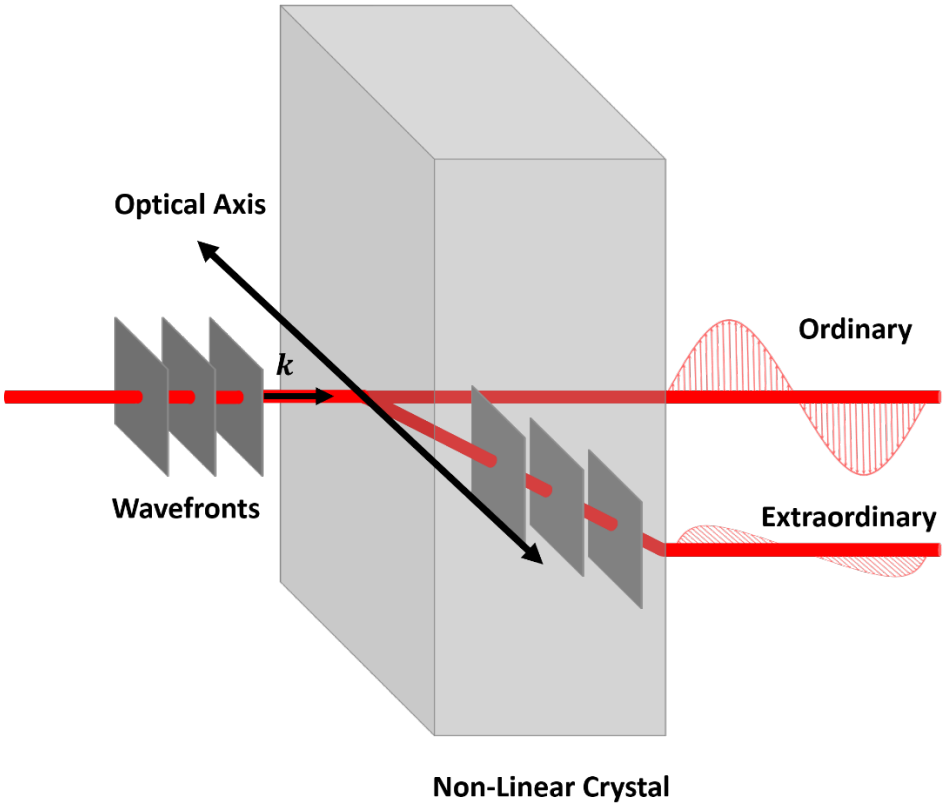

Figure 2-5: Schematic of the walk-off effect in a non-linear crystal, not to scale. The portion of the beam with polarization parallel to the optical axis, the extraordinary beam, will travel with a different refractive index compared to the ordinary beam, which has polarization perpendicular to the optical axis.

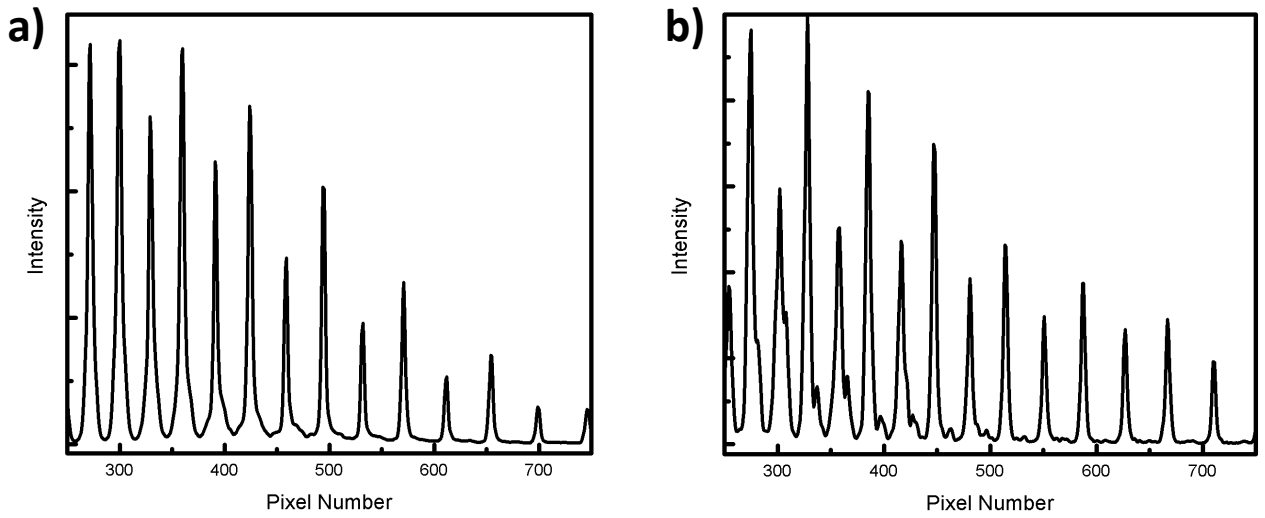

Figure 2-6: Lineouts of Ne high harmonic spectrum before (left) and after (right) installing the MAZEL-TOV. The small secondary peaks arise because the BBO must be rotated in order to compensate for its thickness. This rotation allows some polarization impurity, leading to the walk-off effect. A thinner BBO must be used to eliminate this issue.

2.2.2. Active Beam Stabilization System

With fewer degrees of freedom, it became possible to use two-point beam stabilization on the incident beam, further stabilizing the HHG process. The beam pointing stabilization components were purchased from MRC Systems. The details of the active beam stabilization system are now described. The system consists of a pair of motorized steering mirror mounts and a pair of 4-quadrant diodes (4-QDs). Both of these components are connected to an electronic module that takes the input from the 4-QDs and uses it to control the steering mirrors. The electronic module has a "Start/Stop" button for each actuator that can be used to initiate or terminate the active beam stabilization loop. The detectors are Si based photodiodes, which are divided into quadrants, and have a sensitive area of 10 x 10 mm^2. For the purposes of stabilizing the in-line, two-color HHG process, both steering mirrors are used on the beam before it enters the MAZEL-TOV. For best results, the actuators should not be too close to each other, with the first actuator being closer to the source of instability, and the second actuator being close to the target, which in this case is the SIGC. Also, the beam size at the detector cannot be too big, which in this case would be a diameter of 6 – 8 mm. In order to accomplish this, the actuators are placed before the focusing lens for the SIGC, while the detectors are placed after the lens, such that the beam is focused down at the detectors. The 4-QDs measure the position of the reflection of the 800 nm driving field coming from a 400 nm dichroic mirror positioned after the lens, which is split by a beam splitter. In this configuration, both the position and angle of the beam at the same point can be controlled.

In order to ensure that the detectors operate in the linear range, on the back of each detector, there is a power level display consisting of 10 green light emitting diodes (LEDs), used to make sure the optimal intensity is hitting the detector. The intensity at the detectors should be above level 3 but at no more than level 9 on the power indicator. Fine adjustments to the sensitivity of the 4-QDs can be made by using the potentiometer on the side of the detectors. However, if it is

not possible to reach a suitable level with fine adjustment, the detectors also come with 2 neutral density (ND) filters, one with a low optical density (OD) and the other with a higher OD, which can be used for coarse adjustment of the beam intensity at the detector. In the current setup, the higher OD filter had to be removed for both detectors.

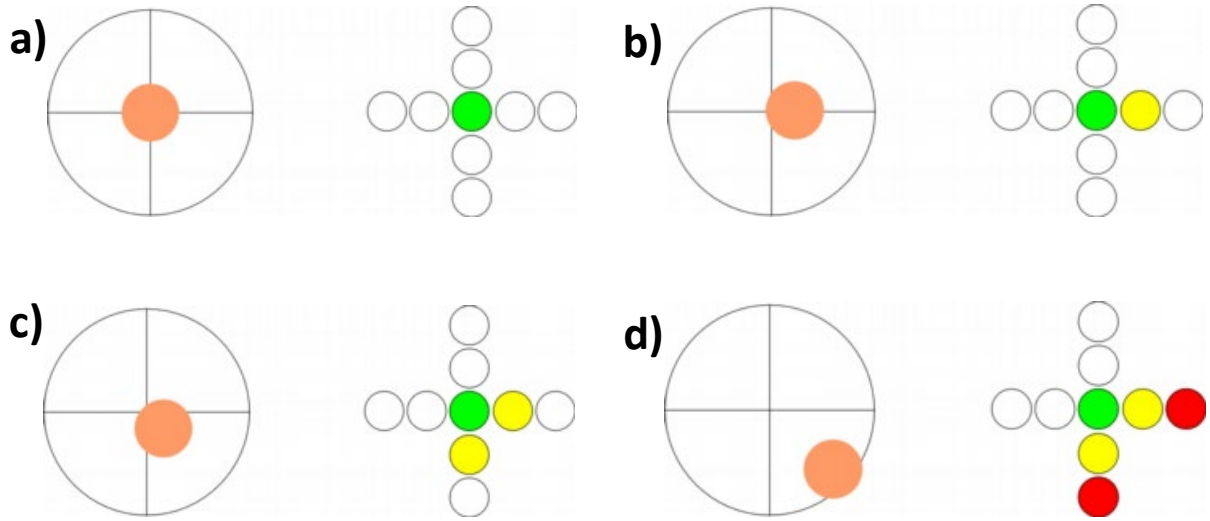

Figure 2-7: (a) When only the green light is on, the beam is centered on the 4-QD. (b) When the green light and only one yellow light are on, the beam is centered on one axis, but not the other. (c) When the green light and two yellow lights are on, the beam is not centered on either axis, but still close enough to be in the linear range. (d) When the red lights are on, the beam is too far from the center of the 4-QD for it to be useful.

The procedure to align the beam using the detectors is as follows: First, turn off the active beam stabilization and align the beam onto the target, which in this case is the CCD in spectrometer chamber. Then, use the beam splitter and the mirror after it to direct the beams onto their respective detectors. A cross shaped array of LEDs on the back of each detector is used to monitor the position of the beam on the 4-QD, as shown in Fig. 2-7. The beam is centered when only the central green LED is lit. Otherwise, if the beam is slightly off-center but the detector is still in the linear range, a yellow LED will light up, while if the beam is too far from the center, the red LED will light up. The horizontal and vertical position readings from the detectors can also be fed directly into an oscilloscope, allowing for a more precise measurement of the beam position on the detector. The combination of the MAZEL-TOV along with the two-point beam stabilization led to much more stable operation of the experiment, allowing for more sensitive experiments to be carried out.

2.2.3. Microchannel Plate Filter for Driving Fields

After the gas cell, the high harmonic driving fields travel collinearly with the generated XUV field and must be filtered out. Previously, this was accomplished by very thin (100s of nm) metal filters, due to the fact that they have very low transmission for 800 nm and 400 nm, but fairly high transmission for large portions of the generated high harmonic spectrum[7]. However, the extremely thin nature of this type of filter makes them notoriously difficult to work with since they are very prone to damage, such as from burning caused by the laser, oxidation caused by the air, or holes

poked by wind. Another disadvantage to this type of filter is the fact that they still absorb a significant portion of the XUV spectrum due to the broadband solid-state, core-level absorption. For example, the Al $L_{2,3}$-edge begins at 73 eV and extends for several hundred eV, cutting off higher energy harmonics, while the Zr N_2-edge cuts off the lower energy harmonics below 75 eV.

Another solution to this problem that does not suffer from these drawbacks is the use a microchannel plate (MCP) to diffract the driving fields while allowing the high harmonics to pass unchanged[7]. This technique takes advantage of the vast difference in wavelengths between the driving fields and the high harmonics, as seen in Fig. 2-8. The MCP is composed of leaded glass, and has a thickness of ~1.5 mm, making it much easier to handle, while not suffering from oxidation issues. Furthermore, it can be made to have a 1" diameter so that it can easily fit in conventional lens or mirror mounts. The channels are bored at a bias angle of 0° with respect to the surface normal, with bore diameters of 5 µm, and center to center distances of 6 µm. The XUV transmission for the MCP is compared to that of 600 nm of Al and 300 nm of Zr in Fig. 2-9. It is clear from the plot that the MCP has a broad transmission range from 10 eV – 200 eV, while the Al filter cuts off the higher energy harmonics, and the Zr cuts off the lower end of the XUV range while transmitting in the range of the Al absorption edge. Another important point of comparison for the MCP filter is its damage threshold, measured to be around 0.6 x 10^{12} W/cm^2, which is comparable to that of 650 nm of Al[7].

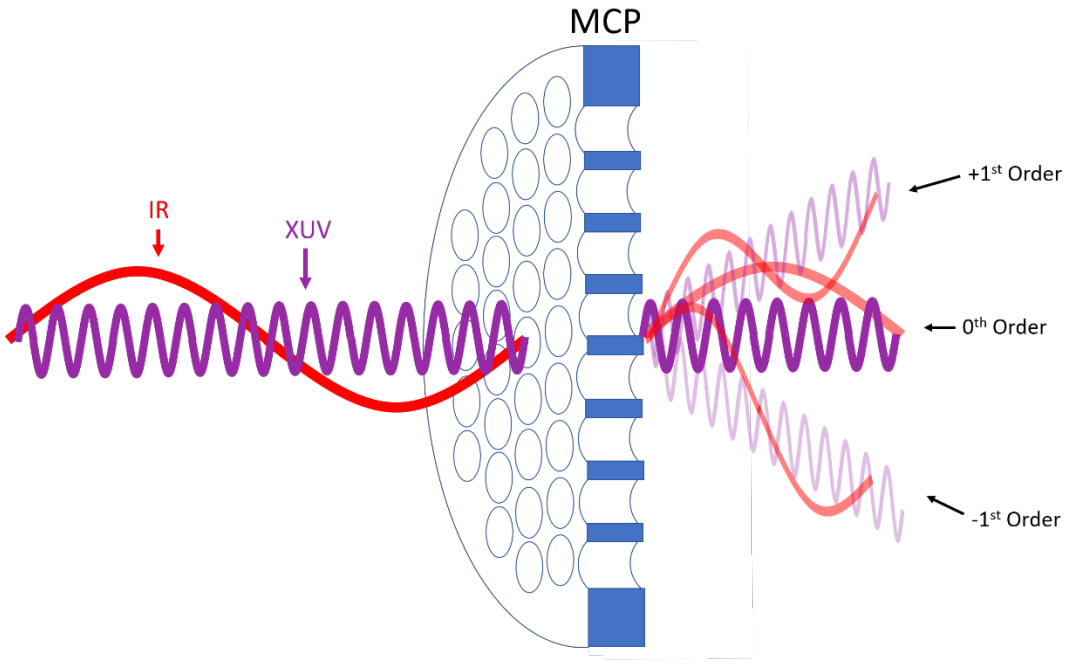

Figure 2-8: Schematic of the MCP filter concept. The longer wavelength of the infrared (or second harmonic) driving field is on the order of the bore size of the MCP which causes it to be diffracted strongly, indicated by the equal intensity of the diffraction orders. The much shorter XUV wavelengths can pass through almost unchanged, indicated by the very faint 1st order diffraction compared to the 0th order.

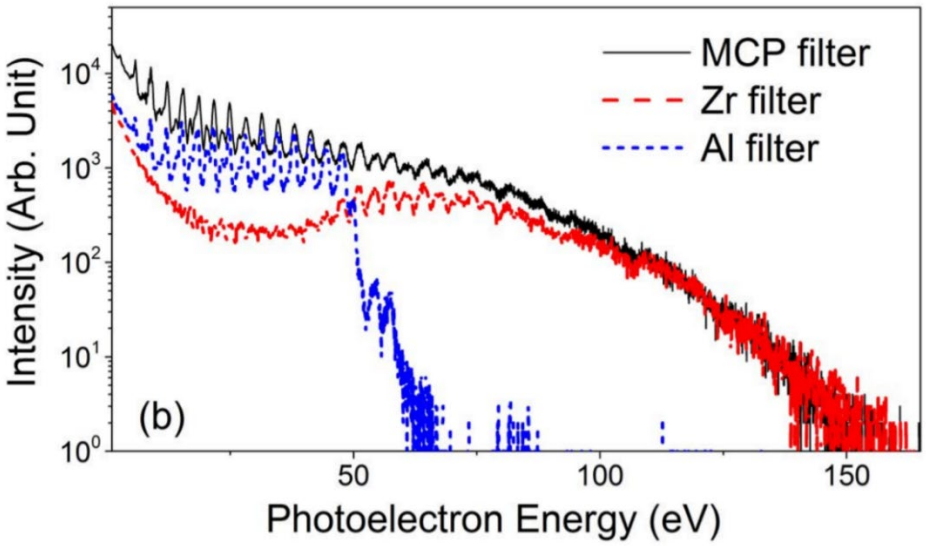

Figure 2-9: Extreme ultraviolet spectrum after passing through MCP (black line), Zr (red dashed), Al (blue dashed).

Previously only Ne and Ar had been used for high harmonic generation in this lab, with one of the main factors being the difficulty of working with Zr filters, due to its low damage threshold. This limited the usable energy range of the high harmonics to 73 eV, at the Al L-edge. However, with the addition of the MCP, He gas can also be used to drive the HHG process. The optimal gas pressure for He will vary depending on the range of harmonics desired, with higher pressure pushing the harmonics to higher energy as well. To generate harmonics at 100 eV and above, the optimal gas pressure is usually ~240 Torr with some fluctuation depending on the focus position of the driving field within the SIGC. Thus, with the installation of the MCP filter, a broad energy range can be covered by substituting between the three noble gases, as shown in Fig. 2-10.

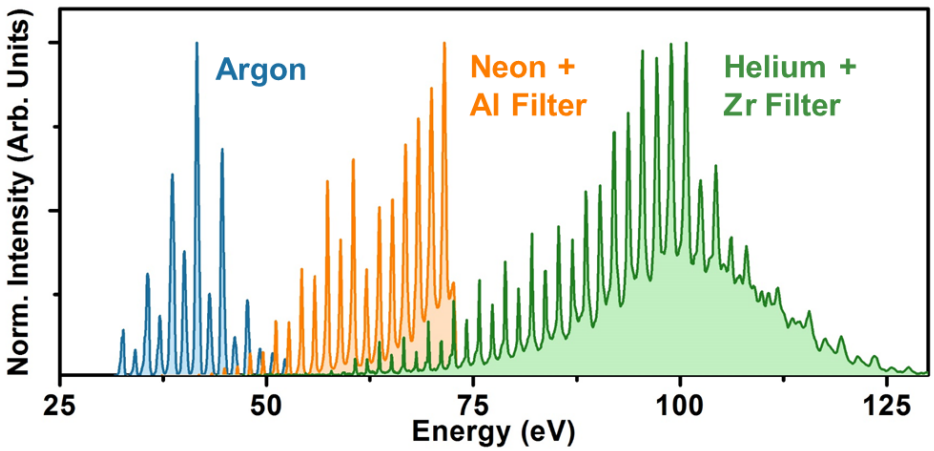

Figure 2-10: The MCP filter allows for the use of He high harmonics, greatly expanding the usable energy range. The high harmonic spectra of the three noble gases used to cover the energy range from 30 – 125 eV. High harmonics for Argon (blue) range from 30 – 50 eV. Those for Neon (yellow) range from 45 – 73 eV cut off by the secondary Al filter. Those for He (green) range from 55 – 125 eV

2.2.4. Gas Cooling of Samples

After the MCP, the beam is incident on a gold coated toroidal mirror, which directs and focuses the XUV beam into the sample chamber. The XUV is usually focused down to a spot size of ~100 μm in diameter at the sample position. The samples are held in place by a mount that can house 5 samples plus a pinhole used for overlapping the pump and probe beams. The mount is held in place by an angle bracket with a magnetic base, which allows for easy sample loading in the cramped vacuum chamber. The bracket is attached to a two-dimensional translation stage (MFA-CCV6, Newport) allowing for the sample holder to be translated in the vertical and horizontal directions while the chamber is under vacuum. This capability is important not only so that multiple samples can be measured without breaking the chamber vacuum, but also due to the fact that the extremely thin samples are prone to heat-induced damage coming from the pump beam. By raster scanning over the sample, the amount of heat deposited on any one spot at a given time is minimized, thus giving the sample a longer usable lifespan.

Under standard conditions, the convective cooling provided by the atmosphere plays a crucial role in the cooling of a hot surface. Since convective cooling is not possible under vacuum, the sample continuously heats under exposure to the laser beam, until damage occurs. However, if a small continuous stream of cold gas can be directed at the sample, convective cooling can take place without having to break the vacuum of the whole chamber. This is desirable because not only would samples suffer less damage over time, certain samples can be so sensitive to heat that they decompose, change phase, or go through thermally induced core-level shifts even at modest temperature changes[8,9]. Thus, active cooling can open up the range of samples that can be studied *in vacuo*. The first iteration was to cool the sample by blowing N_2 gas only from one side, using a Teflon nozzle previously used for HHG. However, it was quickly found that a single gas stream provided too much pressure on one side of the film, breaking them. If the pressure is equalized from the opposite direction, the sample will experience a net zero pressure and remain intact. A schematic comparison of these two iterations is shown in Fig. 2-11.

This design was successfully implemented to improve the sample lifetime, as well as allowing for higher pump power to be used without causing damage to the sample. The limiting factor in this configuration is the load on the vacuum system. If the current on turbo pump power supply reaches 2 A, the turbo pumps will become extremely hot, at higher current the Shimadzu pump will eventually turn itself off due to a temperature fault reached at 40 °C. For this reason, the current is usually kept around 1.7 A during operation to keep the turbo pump temperatures within safe operational levels while still achieving significant cooling. By monitoring the harmonic counts in real time on the CCD, while at the same time opening the gas inlet valve, it is possible to see when there is enough gas flow to start absorbing some of the harmonic flux. The sample temperature was not monitored directly, but the effect of the cooling gas is best exemplified in the case of Si. Using a 100 nm crystalline Si thin film as an example case, without active cooling, the damage threshold at 800 nm is ~20 μJ per pulse, with active cooling the damage threshold goes up to ~40 μJ.

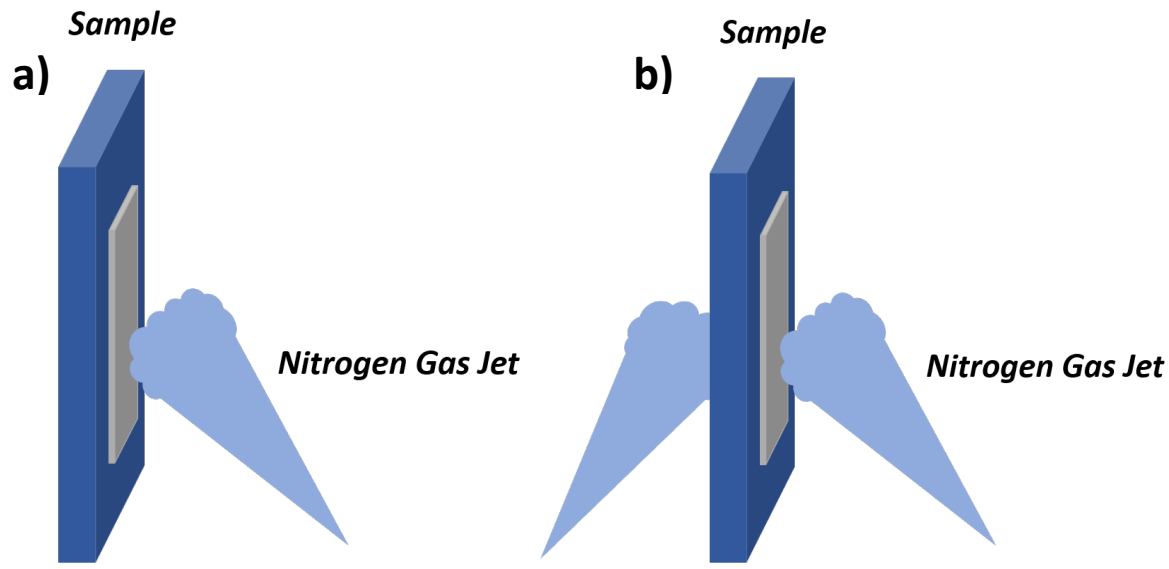

Figure 2-11: (a) Schematic of the first iteration of the active gas cooling. A single jet of dry N_2 gas was directed at the sample. (b) In the second iteration, a second gas jet flowing in the opposite direction was used to equalize the pressure at the sample, which not only keeps the sample from breaking, but doubles the sample cooling.

2.2.5. Spectrometer

After the sample, the remaining XUV makes its way through a small hole at the back of the sample chamber to enter the smaller spectrometer chamber. A few inches in front of the entrance, a metal filter is used to filter out any remaining residual 800 nm and 400 nm driving fields. The mount can hold two filters at once, and depending on the energy range of interest, either an Al filter or a Zr filter could be lowered into the beam path. After this filter, the XUV beam is dispersed and focused onto a CCD camera by a concave diffraction grating. This configuration has two major advantages to a pre-sample monochromator. First, allowing the whole pulse to impinge on the sample means that the temporal profile of the pulse is undisturbed, which is crucial for ultrafast experiments. Also, by using a diffraction grating after the sample, the full XUV spectrum can be imaged at once, allowing for much quicker and more efficient data acquisition.

A concave grating is used in order to focus the XUV, leading to much higher photon flux at the detector compared to a plane grating. However, if all groove lines were equally spaced, each harmonic would arrive at a different focus position on the CCD camera. In order to achieve a flat field focus, a variable line space grating is used[10], where the distance between the grooves of the grating are optimized to focus each harmonic to the same plane. Given the grating equation,

$$m\lambda = d(sin\alpha + sin\beta), \tag{2.3}$$

where m is the diffraction order, d is the average groove spacing, α is the incidence angle, and β is the diffraction angle. The grating used (Hitachi High Technologies) has an average groove spacing of 1200 grooves/mm, with a blaze angle of 3.2°. The extreme ultraviolet CCD camera used (PIXIS-XO 400B, Princeton Instruments) is back-illuminated and optimized for x-ray

absorption. The dimensions of the camera are 1340 x 400 pixels and each pixel is 20 x 20 μm^2, giving a length of L = 26.8 mm. At this incidence angle, the first order diffraction energy spread of 32-77 eV will diffract at angles 72.20° and 78.32°, respectively. The camera is aligned such that this energy range is dispersed onto the detector. Given the pixel density and CCD dimensions, along with the grating equation (Eq. 2.3), a calibration curve can be made to match any number of refence points. Due to its well separated and sharp absorption peaks in the XUV range, Xenon gas[11] is used as a standard sample for XUV absorption in order to calibrate the CCD and determine the spectrometer's resolution, but any well-known edges can be used as reference points for a calibration.

In order to image absorption edges that are at higher energies, ideally the camera would be translated across the flat field plane in order to reach the desired harmonic. Unfortunately, the CCD must be kept at vacuum and is currently mounted onto a rigid stainless-steel chamber. Nevertheless, it is still possible to image the higher energy harmonics with a stationary CCD, albeit at lower resolution, by simply rotating the grating to change the incident angle of the XUV with respect to the grating. If the change in incidence angle is small, the deviation from flat field focus will also be small, allowing for the imaging of higher energy harmonics. Using the grating equation (Eq. 2.3) it is found that to reach the Si 3p edge at 99 eV, for example, the grating would only need to be rotated by about 5°.

2.2.6 Pump Beam Path

The ~1.5 mJ portion of the pulses that are reflected at the first beam splitter are then directed towards the sample to be used as the pump source. The main motivation for the work in this thesis was to understand the fundamental charge carrier dynamics that govern solar energy conversion. As such, it was important to have a pump source that was highly tunable, spanning the same energy range as the solar spectrum at the Earth's surface[12]. Furthermore, in order to carefully study heterojunctions, it is important to have a selective pump as well as probe. Thus, depending on the material being investigated, the 800 nm beam can either be used directly, or it can be converted to other wavelengths through the use of nonlinear optics. One option is to simply convert the 800 nm to either its second or third harmonic, at 400 nm and 266 nm respectively. The other option is to use an OPA that can tune the wavelength anywhere from 235 – 3000 nm. The reason for generating the harmonics of the fundamental pulses separately is due to better beam quality, pulse width, and power output, compared with pulses coming out of the OPA. Regardless of the wavelength used the beam makes its way onto a retroreflecting, motorized, time delay stage. After the delay stage, the beam can be attenuated using a gradient neutral density filter, and lastly it is focused into the sample chamber using a 500 mm focal length spherical lens mounted on a 4" translational stage. In the chamber, the beam is reflected by a square aluminum mirror, making about a ~1° crossing angle with the XUV beam at the sample. A piece of black foil at the back of the chamber with a small hole in it allows the XUV to pass while blocking the pump beam.

When using the harmonics of the fundamental field, the optical layout can be modified to produce the desired pump wavelength. In the case of second harmonic generation, a 100 μm thick type-I BBO ($\Theta = 29.2°$) is placed after the retroreflector, while the remaining mirrors are replaced with 400 nm dielectric mirrors in order to filter out the remaining 800 nm light. The BBO is rotated

to be perpendicular with respect to the polarization of the incoming beam, ensuring that the 400 nm pulses are polarized in the same direction as the incoming fundamental pulses. The conversion efficiency can reach 5% without focusing of the beam into the BBO, leading to around 80 μJ per pulse. To create the third harmonic, a calcite plate, a zero-order dual waveplate, and a 20 μm thick type I BBO ($\Theta = 44.3°$) are placed in sequence after the retroreflector. The calcite plate is used to compensate for the delay between the 800 nm and 400 nm pulses induced by the birefringence of the first BBO. The waveplate rotates the 400 nm pulse's polarization to match the horizontal polarization of the fundamental 800 nm pulses. The third harmonic generation BBO has its OA kept perpendicular to the polarization direction of the incoming 800 nm pulses so that the 266 nm pulses can have horizontal polarization as well. After the second BBO, the mirrors are replaced by 266 nm dielectric mirrors in order to filter out the residual 800 nm and 400 nm light. Typically, ~4 μJ of pulse energy can be directed into the sample chamber.

When any other wavelength is needed, an 800 nm high reflective mirror mounted with a magnetic base is placed in front of the beam, as shown in Fig. 2-1, redirecting it towards a periscope that sends the beam into the OPA (TOPAS-Prime, Light-Conversion Technologies). The TOPAS is motorized and computer controlled, allowing for fast and reliable control of the wavelength used, and the layout is shown in Fig. 2-12. The optical layout of the TOPAS is discussed in brief. It is composed of two main sections, the pre-amplifier region which generates a signal and idler beam, and the amplifier region, which uses an 800 nm pump and can amplify the seed or idler wavelengths. First, the incoming beam is split by a 96% reflectivity beam splitter (BS), with the transmitted portion being sent into the pre-amplifier and the reflected portion sent into the amplifier. In the pre-amplifier, the transmitted portion of the beam is further split by an 80% reflectivity BS, with the transmitted portion passing through a sapphire plate to generate a white light continuum (WLC), while the reflected portion is used to pump a non-linear crystal (NC) which is seeded by the WLC in a non-colinear geometry. In the amplifier region, the beam coming from the first NC is used as the seed while the reflected portion of the 800 nm beam incident on BS1 is used as the pump, now in a collinear geometry. The signal and idler beams can be amplified using this configuration to produce high powered pulses with wavelengths ranging from ~1140 – 2600 nm.

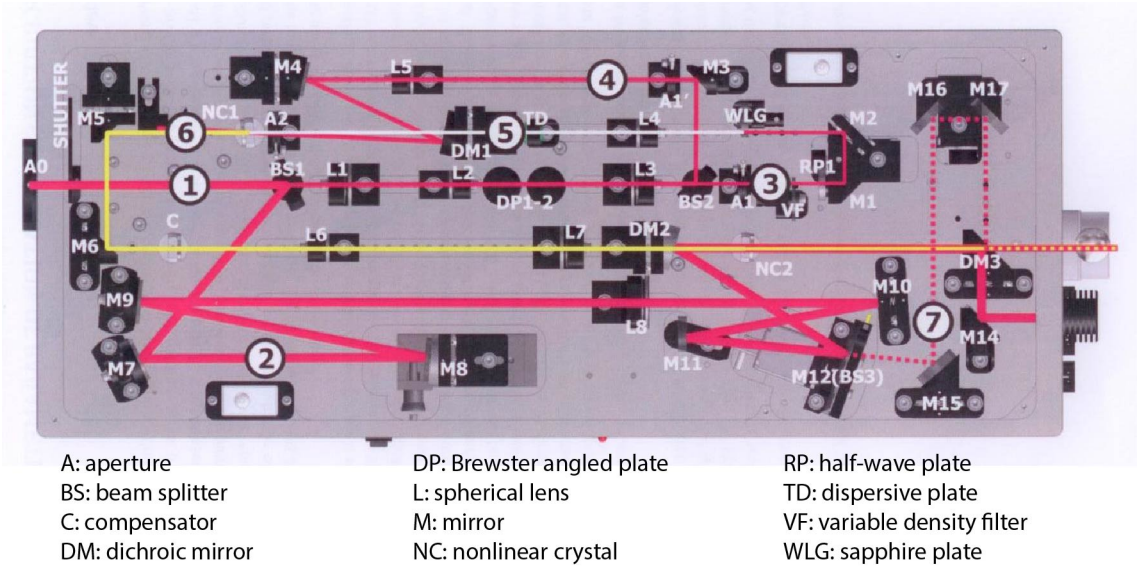

Figure 2-12: The optical layout for the TOPAS-Prime. It contains a pre-amplifier region which generates the white-light continuum used to generate the signal and idler beams, and an amplifier region which can either amplify these wavelengths, or generate others. Courtesy of Light Conversion Ltd.

In order to reach shorter wavelengths, the TOPAS can perform many different parametric processes to convert the signal and idler frequencies. Two separate wavelength mixing units have been purchased for the TOPAS, each containing multiple mixing crystals inside that can be rotated to the necessary angle for each parametric process. For wavelengths in the near infrared, the second harmonic of the idler (SHI) or the second harmonic of the signal (SHS) frequencies can be generated. For most of the visible spectrum, sum frequency generation must be performed with either the signal (SFS) or idler (SFI), using a portion of the 800 nm beam as the pump. There are two configurations available with the TOPAS to perform sum frequency generation, a depleted pump and a fresh pump option, with the fresh pump path being shown as path #7 in Fig. 2-12. Initially, the depleted pump option was purchased since it is the standard option, but it was soon found that the beam quality for the SFS and SFI wavelengths was too poor for reliable use in the experiment, especially the SFI wavelengths, so the fresh pump option was purchased. The depleted pump configuration simply moves the dichroic mirror (DM) out of the way allowing the residual 800 nm light to travel collinearly with the signal or idler into the third mixing crystal. On the other hand, the fresh pump configuration keeps the DM in place for all output wavelengths, but a motorized dual mirror mount is used to house both M12 and a 90% reflectivity BS. The BS can be used in conjunction with the retroflector created by M16 and M17 to send part of the 800 nm pump to the other side of the DM so that it can be used to pump the SFI, SFS processes. Lastly, the second mixing unit can be used to generate ultraviolet wavelengths by either generating the fourth harmonic of the idler (FHI) and signal (FHS) wavelengths or the second harmonic of the sum frequency of either the idler (SHSFI) or signal (SHSFS). In any case, the output is filtered by a set of two dichroic mirrors, which can be switched out depending on the wavelength range being used. The wavelength range for each process is shown in Table 2-1, along with their possible pulse energy ranges and polarizations.

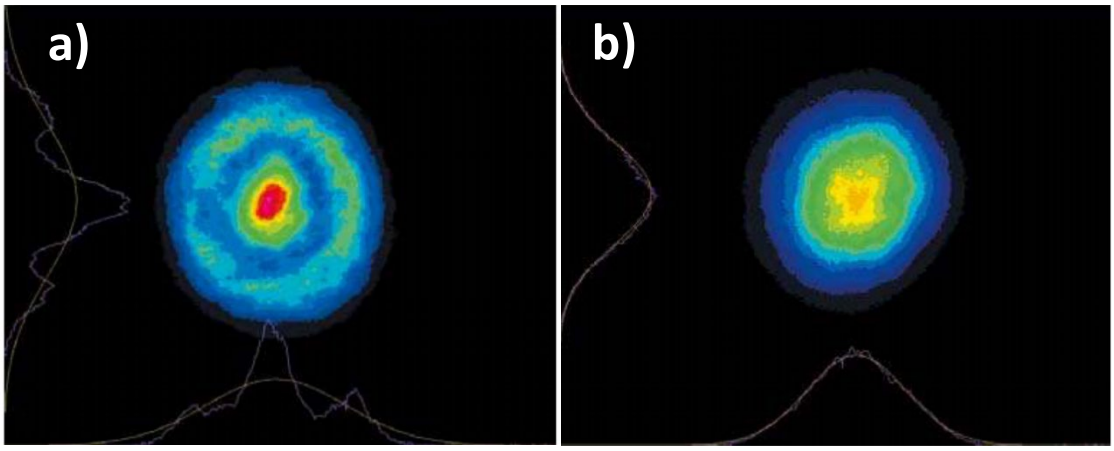

Figure 2-13: Comparison between the output beam profiles for the depleted pump (left) and fresh pump (right) configurations for the sum frequency generation processes of the TOPAS. Using the depleted configuration made it impossible to cleanly focus the beam spot to the desired size (~100 μm diameter). Courtesy of Light Conversion Ltd.

Parametric Process	Wavelength Range (nm)	Pulse Energy (μJ)	Mixer Rotation Axis[a]		Output Pulse Polarization
			Mixer 1	Mixer 2	
Idler + Pump	1570 – 2600	70 – 190	-	-	V
Signal + Pump	1140 – 1640	190 – 300	-	-	H
SHI	790 – 1150	2 – 40	H	-	V
SHS	570 – 810	25 – 110	V	-	H
SFI	530 – 600	35 – 100	H	-	V
SFS	471 – 537	40 – 90	H	-	V
FHI	395 – 485	0.55 – 6	H	V	H
FHS	285 – 405	1.9 – 15	V	H	V
SHSFI	266 – 300	3 – 20	H	V	H
SHSFS	235.5 – 267.5	2.3 – 14	H	V	H

Table 2-1: Output wavelengths and pulse energies for each parametric process available with the TOPAS-Prime. The pulses entering the TOPAS have a wavelength of 800 nm, a pulse width of 40 fs, a pulse energy of 1.25 mJ, at a repetition rate of 1 kHz, and is in the horizontal polarization. V-vertical, H-horizontal. [a]The mixer rotation axis is vertical when the cover faces up.

The filtered output is then brought back to the height of the rest of the optical plane with a periscope. After the periscope, an Al mirror with a magnetic mount needs to be placed in the beam path in order to direct it towards the sample chamber, with the usual dichroic mirrors used to reflect the fundamental frequency and its harmonics being replaced by Al mirrors.

After choosing the desired pump wavelength, the pulses travel through a motorized, computer controlled, retroreflecting delay stage. The maximum delay that can be achieved between the pump and probe pulses is limited by how far the delay stage can move relative to the point of zero delay

between the pump and probe pulses, with positive delay being defined as having the probe pulse arriving first. During the work performed in this thesis, it was found that the delay stage was secured to the table in a position that limited its positive delay range to less than +100 ps. However, the length of the delay stage track allows for a time delay >300 ps, thus by moving the entire delay stage assembly closer to the incoming pump beam by ~2 inches, these longer time scales could be achieved. This update to the system was important in order to study longer time scale dynamics which are relevant in the decay of quasiparticles in solids.

2.3 Future Improvements

Although this table-top transient XUV absorption apparatus has been a powerful tool used to study the ultrafast electronic and lattice dynamics of solid state systems, it can still be further improved in order to study an even broader range of samples with better resolution. It is mentioned in section 2.2.1 that the new in-line second harmonic generation configuration currently uses a BBO that is too thick. This leads to a conversion efficiency that is too high for the two color HHG process. To mitigate this, the BBO crystal is rotated to decrease the conversion efficiency, also leading to higher time delay between the two pulses. In turn leading to an increase in the angle of the calcite plates needed to compensate for the delay. Unfortunately, the tuning of the calcite will lead to back reflections which degrade the spectrometer resolution. The desired conversion efficiency for the BBO should be about 10 times less than what is currently being used, which would end up being ~1.5%. Under the current conditions, where the beam is unfocused, the efficiency is low enough that the pump can be considered to be undepleted, and the group velocity mismatch is negligible, the desired BBO thickness has been calculated to be 25 μm. The BBO still needs to be purchased and installed, but should lead to a cleaner beam and better resolution.

Another valuable upgrade to the system would be the ability to image a wider range of harmonics at once. Currently the residual driving fields are filtered by a combination of an MCP filter right after the SIGC and a circular metal filter in the spectrometer chamber right before the diffraction grating. There are two metal filters available for use in the spectrometer chamber, Al and Zr, which can be switched depending on the energy range of interest, acting as low-pass and high-pass filters for the XUV energies, respectively. The Al $L_{2,3}$-edge sharply cuts off the harmonic intensity above 72 eV, while the Zr N_1-edge cuts off the lower energy harmonics below ~65 eV. Another solution is to place a rectangular filter after the grating, where one half is Al and the other half is Zr, as shown in Fig. 2-14b. By placing this type of foil after the grating, the low energy harmonics up to the Al $L_{2,3}$-edge impinge on the Al portion of the filter, and the higher energy harmonics impinge on the Zr portion. This configuration will allow for both sides of the harmonic spectrum around the 65-72 eV region to be imaged at once. The rectangular metal filter has been purchased from the Lebow Company and it is currently being installed.

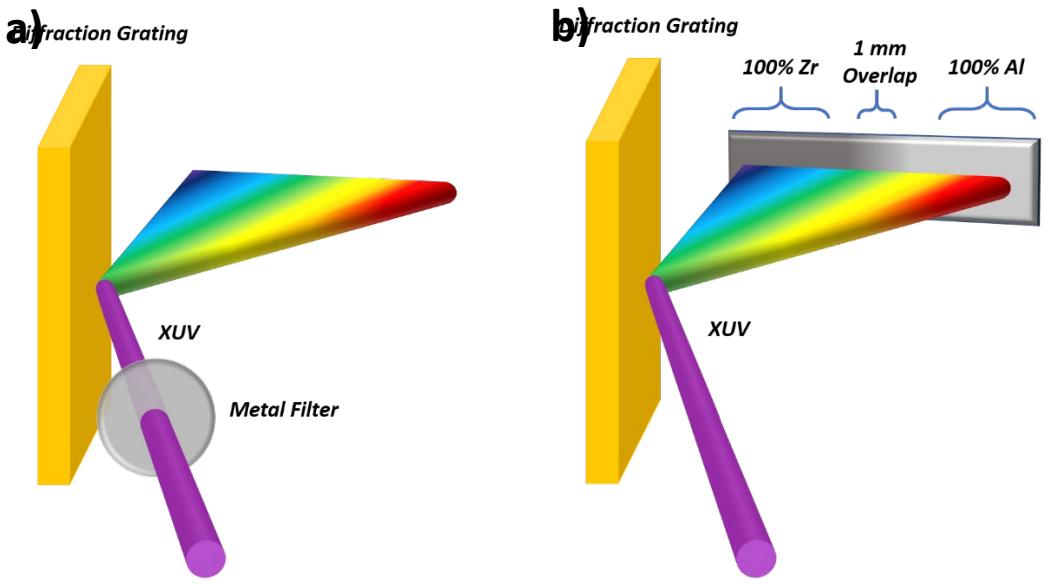

Figure 2-14: (a) Schematic showing the current configuration for filtering out the residual driving fields traveling along with the XUV beam, which are still present after passing through the MCP and sample. A thin metal film, either Al or Zr, is placed in the beam path before the diffraction grating. (b) The new configuration would place an elongated, composite filter after the diffraction grating, using Zr to filter the residual driving field corresponding to the region of the higher order harmonics and Al to block the lower ones. A 1 mm region where both metals overlap blocks the intermediate region, corresponding to the energy region around 65 – 73 eV.

Lastly, the spectrometer achieves the best resolution and reflectivity at an incidence angle of 87°, and the CCD is fixed in position such that at this incidence angle the harmonics on the camera span an energy range of ~30-78 eV. Thus, in order to image higher energy harmonics, the grating must be rotated away from the flat field focus angle. However, the grating's flat field focus plane covers energies from 60 – 250 eV, so if the CCD could be moved instead, a wider range of harmonics could be imaged with optimal resolution. In order to obtain a broad energy coverage, a spectrometer chamber that has a movable CCD detector was designed and implemented by Andrew Attar, also in the Leone lab[13]. The design schematic is presented in Figure 1.4 of his thesis. The CCD is housed in a custom-made vacuum chamber that is connected to a stainless-steel bellows made for vacuum applications, with the CCD itself attached to a movable stage that can be controlled from outside of the chamber. In order to implement this design into the D42 apparatus, a similar bellows design would have to be designed with a smaller footprint since there is not much room between the CCD and the wall. In his thesis[14], Chang-Ming Jiang proposed an upgraded sample chamber that could be used to prepare samples *in vacuo*. Thus, for the general longevity of this experimental apparatus, it would be beneficial to design a new spectrometer chamber that can both prepare samples as well as image a broad energy range with excellent resolution.

2.4 Bibliography

1. Kim, I. J. *et al.* Highly efficient high-harmonic generation in an orthogonally polarized two-color laser field. *Phys. Rev. Lett.* **94**, 2–5 (2005).

2. Kfir, O. *et al.* In-line production of a bi-circular field for generation of helically polarized high-order harmonics. *Appl. Phys. Lett.* **108**, (2016).

3. Milošević, D. B. & Becker, W. Attosecond pulse trains with unusual nonlinear polarization. *Phys. Rev. A - At. Mol. Opt. Phys.* **62**, 4 (2000).

4. Boyd. Boyd - Nonlin Optics. *J. Chem. Inf. Model.* **53**, 1689–1699 (2013).

5. Nikogosyan, D. N. Beta barium borate (BBO) - A review of its properties and applications. *Appl. Phys. A Solids Surfaces* **52**, 359–368 (1991).

6. Sutherland, R. L., Mclean, D. G. & Kirkpatrick, S. *Handbook of Nonlinear Optics with contributions by*.

7. Zhang, Q. *et al.* Suppression of driving laser in high harmonic generation with a microchannel plate. *Opt. Lett.* **39**, 3670 (2014).

8. Leijtens, T. *et al.* Towards enabling stable lead halide perovskite solar cells; Interplay between structural, environmental, and thermal stability. *J. Mater. Chem. A* **5**, 11483–11500 (2017).

9. Riffe, D., Hale, W., Kim, B. & Erskine, J. Thermally induced core-electron binding-energy shifts in transition metals: An experimental investigation of Ta(100). *Phys. Rev. B* **54**, 17118–17122 (1996).

10. Bowyer, M. C. H. and S. Variable line-space gratings: new designs for use in grazing incidence spectrometers. *Appl. Opt.* **22**, 3921–3924 (1983).

11. Ederer, D. L. & Manalis, M. Photoabsorption of the 4 d electrons in xenon. **65**, 634 (1975).

12. ASTM G173-03(2012), Standard Tables for Reference Solar Spectral Irradiances: Direct Normal and Hemispherical on 37° Tilted Surface, ASTM International, West Conshohocken, PA, 2012.

13. Attar, A. R. Photochemical Reaction Dynamics Studied by Femtosecond Soft X-ray Transient Absorption Spectroscopy. University of California - Berkeley (2016).

14. Jiang, C.-M. Charge Carrier Dynamics in Transition Metal Oxides Studied by Femtosecond Transient Extreme Ultraviolet Absorption Spectroscopy. University of California - Berkeley (2015).

Chapter 3

Excitation-Wavelength-Dependent Small Polaron Trapping of Photoexcited Carriers in α-Fe_2O_3

*The content and figures in this chapter are reprinted or adapted with permission from L. M. Carneiro, S. K. Cushing, C. Liu, Y. Su, P. Yang, P. Allivisatos, S.R. Leone, "Excitation-wavelength-dependent small polaron trapping of photoexcited carriers in α-Fe_2O_3." Nature Materials, **2017**, 16, 819–825. Copyright 2017 Nature Publishing Group.*

Small polaron formation is known to limit ground-state mobilities in metal oxide photocatalysts. However, the role of small polaron formation in the photoexcited state and how this affects the photoconversion efficiency has yet to be determined. In this chapter, transient femtosecond extreme-ultraviolet measurements suggest that small polaron localization is responsible for the ultrafast trapping of photoexcited carriers in hematite (α-Fe_2O_3). Small polaron formation is evidenced by a sub-100 fs splitting of the Fe 3*p* core orbitals in the Fe $M_{2,3}$ edge. The small polaron formation kinetics reproduces the triple-exponential relaxation frequently attributed to trap states. However, the measured spectral signature resembles only the spectral predictions of a small polaron and not the pre-edge features expected for mid-gap trap states. The small polaron formation probability, hopping radius and lifetime varies with excitation wavelength, decreasing with increasing energy in the t_{2g} conduction band. The excitation-wavelength-dependent localization of carriers by small polaron formation is potentially a limiting factor in hematite's photoconversion efficiency.

3.1 Introduction

Small polaron formation is known to limit ground-state mobilities in metal oxide photocatalysts. However, the role of small polaron formation in the photoexcited state and how this affects the photoconversion efficiency has yet to be determined. Here, transient femtosecond extreme-ultraviolet (XUV) measurements suggest that small polaron localization is responsible for the ultrafast trapping of photoexcited carriers in hematite (α-Fe_2O_3). Small polaron formation is evidenced by a sub-100 fs splitting of the Fe 3*p* core orbitals in the Fe $M_{2,3}$ edge. The small polaron formation kinetics reproduces the triple-exponential relaxation frequently attributed to trap states. However, the measured spectral signature only resembles the spectral predictions of a small polaron and not the pre-edge features expected for mid-gap trap states. The small polaron formation probability, hopping radius, and lifetime varies with excitation wavelength, decreasing with increasing energy in the t_{2g} conduction band. The excitation-wavelength dependent

localization of carriers by small polaron formation is potentially a limiting factor in hematite's photoconversion efficiency.

Metal oxide semiconductors are promising materials use in solar water splitting and artificial photosynthesis. In particular, hematite (α-Fe_2O_3) is an Earth-abundant semiconductor that has a visible light band gap in the optimal 2 eV range and is photostable, making it an ideal candidate[1-3]. However, the lifetime of photoexcited carriers in hematite is picoseconds, not the milliseconds needed to drive water oxidation[4-10]. Short carrier recombination lifetimes in hematite are usually assigned to surface and mid-gap trap states[4-10]. Doping, nanostructuring, surface modifications, and co-catalysts have been used to alleviate the mobility, lifetime, and kinetics issues[1-3,11-17]. However, even when trap states have been passivated, hematite's overpotential and poor fill factor issues are not fully overcome[11,12]. Even the best performing hematite electrodes are still at one third of their potential efficiency[18].

This discrepancy in performance has recently been attributed to hematite's small polaron-limited, minority carrier conduction[6,19,20]. When an excess charge is added to an Fe center, the electron-optical phonon interaction causes the lattice to expand, self-trapping the carrier[19,21]. For transport to occur, phonon motion must bring two Fe centers in proximity, giving the charge carrier a finite probability to hop between atoms. Similar to a mid-gap or surface trap state, the small polaron acts to localize the carrier to a specific site until sufficient thermal energy is present for conduction[22-25]. Given that polaron formation is accelerated at defect sites, small polaron formation also acts to trap mobile carriers at recombination centers[21].

While it is known that injecting a photo-excited electron from a dye to hematite creates a small polaron[26], it is unknown whether photoexcitation of hematite itself leads to small polaron localization. Small polaron formation should be particularly relevant for the photoexcited state in hematite because the dominant optical transition shifts electron density from the O to Fe center[26]. This shift of charge density may accelerate localization of the electrons into a small polaron, decreasing mobility compared to a free carrier state and limiting photoconversion yields. While ground state polaron-transport is accepted for most metal oxide semiconductors[27], the role of small polarons in the photoexcited state remains unidentified.

In this chapter, transient extreme ultraviolet (XUV) spectroscopy is used to investigate small polaron localization of photoexcited carriers in hematite. Spectroscopic signatures characteristic of electron localization by small polarons are measured within 100 fs following photoexcitation. The small polaron state is found to form directly following the first optical-phonon scattering events and polaron formation continues for ~2-3 picoseconds. The small polaron formation rate versus excitation energy is found to be fastest at a visible light excitation of 2.5 eV, but the small polaron formation probability decreases with increasing energy within the t_{2g} conduction band. The observed spectral splitting of the Fe *3p* core level after photoexcitation suggests that trapping and localization of minority carriers on ultrashort timescales can be attributed to small polaron formation and not occupation of mid-gap or surface states. Further, these trends suggest that the wavelength-dependent photoconversion efficiency does not follow the increase in visible light absorption in the t_{2g} conduction band[1-3,14-18] because small polaron formation alters the photoexcited electron mobilities to a different extent depending on excitation energy.

3.2 Experimental Methods

The α-Fe_2O_3 thin films were deposited onto 30 nm Si_3N_4 substrates by RF magnetron sputtering of ~10 nm of iron metal, and subsequent oxidation in ambient atmosphere in a tube furnace at 500 ºC for 1 h, followed by natural cooling to room temperature. The resonant $M_{2,3}$-edge absorption of the samples has two peaks at 55 eV and 57 eV in agreement with literature values for thin film α-Fe_2O_3. Vura-Weis et al. prepared α-Fe_2O_3 thin film samples using the same process and confirmed the α phase composition through electron diffraction measurements[49].

Transient XUV pulses were created using a 1 kHz Ti:Sapphire chirped pulse amplifier (Spitfire Pro, Spectra Physics) generating 40 fs, 3.5 mJ pulses centered at 800 nm. The XUV spectrum is produced using high harmonic generation (HHG) in a 40 cm long semi-infinite gas cell (SIGC) filled with 80 Torr of neon. The spot-size of the focused beam is about 100 μm giving a peak intensity of 5.7 X 10^{14} W/cm^2. 20 μJ of 400 nm light was mixed with the 800 nm fundamental to generate both odd- and even-order harmonics. A 0.6 μm thick Al foil is employed to block any residual 800 nm and 400 nm light from reaching the sample. The XUV pulses were spectrally dispersed by a variable line spacing grating onto a CCD camera (PIXIS-400, Princeton Instruments). The spectrometer has an energy range of 38 – 80 eV and a spectral resolution of ~150 meV. An optical parametric amplifier (TOPAS-Prime, Light Conversion) was used to excite the sample. The pump beam spot size at the sample is ~150 μm, and the pump power was adjusted to create a carrier density of 8 x 10^{19} per cm^3 at each excitation wavelength. In order to avoid thermally induced damage, each 3 mm x 3 mm sample is raster scanned by 100 μm step sizes between each pump-probe time delay measurement. In order to avoid artifacts caused by scattering of residual pump beam, spectra taken with the XUV pulse arriving 500 fs before the pump pulse are subtracted from the spectra at each pump probe time delay.

3.3 Results and Discussion

3.3.1 Optical Excitation Induced Change of XUV Absorption at Fe $M_{2,3}$-edge

The XUV transient absorption at the Fe $M_{2,3}$-edge before excitation, immediately after excitation, and after polaron formation is shown in Fig. 3-1. The XUV absorption corresponds to the transitions between the Fe 3*p* core-level and the unoccupied Fe 3*d* density of states as modified by the Fe 3*p* core-hole, shown schematically in the second panel of Fig. 3-1b. The core-hole potential makes the XUV absorption a poor representation for the conduction band energy structure of the first panel in Fig. 3-1b. In particular, for the localized Fe 3*d* orbitals, the XUV absorbance reflects the multiplet splitting between the $3p^6 3d^5$ ground state and the $3p^5 3d^6$ XUV excited state, combined with the spin-orbit coupling of the core level, and all broadened by the core-hole lifetime[28].

Excitation of hematite with visible light leads to a charge transfer transition from majority O 2*p* hybridized orbitals to majority Fe 3*d* hybridized orbitals (Fig. 3-1a, represented by the dashed and solid blue circles)[26]. The shift of electron density from the O to Fe atom hybridizes the oxygen ligand's and metal center's energy levels, with the resultant energy relaxation decreasing with increasing separation between ligand and metal energy levels[28]. Thus, when the charge transfer hybridized state interacts with the core-hole in an XUV transition, the separation between multiplet peaks in the XUV structure is decreased compared to the ground state plus core hole absorption (shown schematically in second to third panel of Fig. 3-1b).

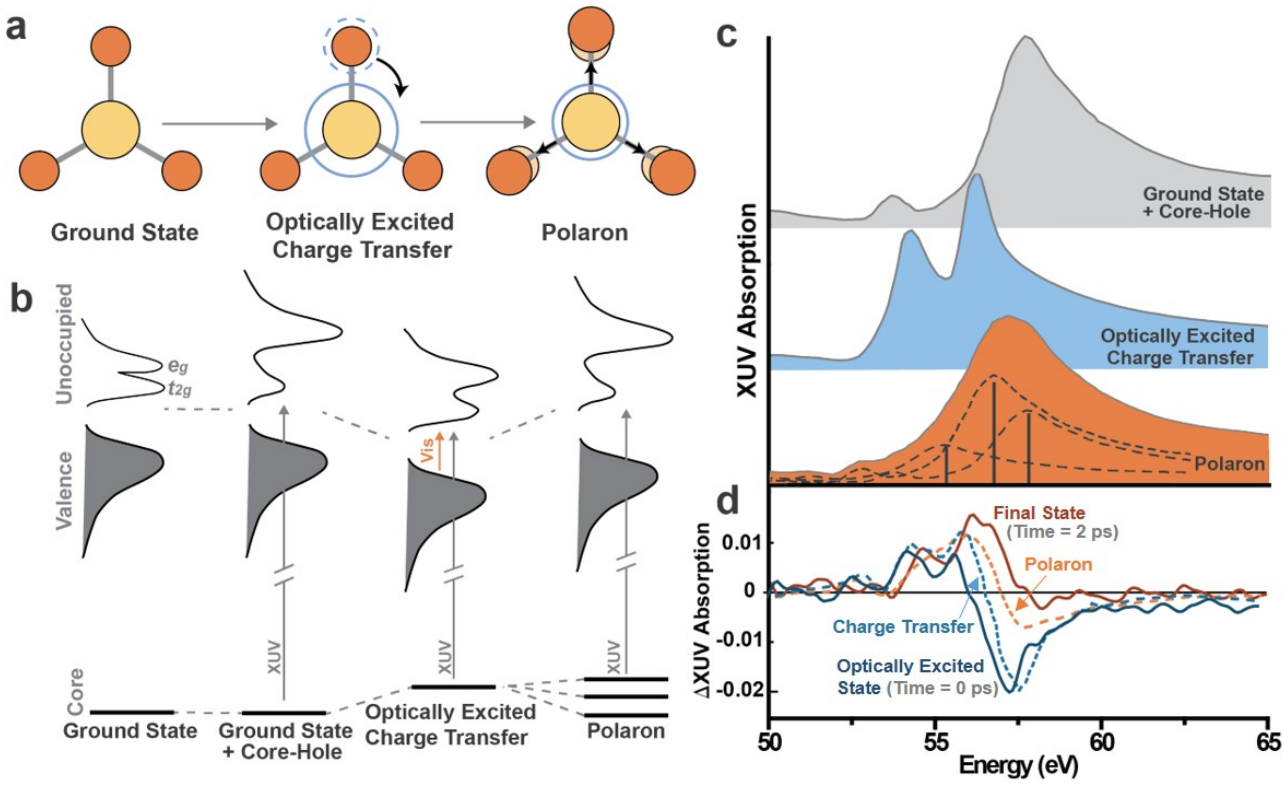

Figure 3-1: (a) Initial excitation of Fe_2O_3 leads to a charge transfer transition from oxygen (dark orange) to iron (light orange). The initial excited carriers undergo optical-phonon scattering, during which the charge can be trapped in a small polaron, expanding the lattice. (b) The XUV transition reflects the core-hole modified unoccupied density of states (second panel) instead of the ground state (first panel). The optical charge-transfer transition changes the electronic symmetry and occupation of the Fe atom, changing the multiplet splitting measured in the XUV transition. The polaron locally changes the lattice symmetry, breaking the degeneracy of the *3p* core level, and replicating the ground state plus core hole XUV transition to result in an overall broadened and red-shifted absorption. (c) The XUV absorption spectra of the polaron formation process; the top panel is experimental data, the bottom two panels are simulations. The multiplet splitting caused by the core hole is visible in the experimental ground state plus core hole absorption (first panel). The decrease in multiplet splitting after optical excitation is predicted following Reference 26 (second panel). The small polaron spectrum is predicted by splitting the experimentally measured ground state plus core hole following Reference 30 (third panel). The three contributions to the overall absorption in the polaron case are shown as dashed lines. (d) The differential absorption predicted (dashed lines) from the difference in the spectrum of part (c) is compared to the *Time=0 ps* and *Time=2 ps* differential absorption measurements following a 480 nm excitation pulse (solid lines).

The change in XUV multiplet splitting with optical excitation is experimentally demonstrated by the differential absorption measured immediately following above-band-gap excitation with 480 nm light (*Time = 0 ps*, Fig. 3-1d). The optical charge-transfer hybridized state appears in the differential absorption as a double-peaked, positive increase in absorption between 53 and 56 eV and a decrease in absorption between 56-60 eV[26]. These features correspond to the difference in multiplet peak splitting between the ground and charge-transfer hybridized state, which can be seen in Fig. 3-1c by comparing the experimental core-hole modified ground state XUV absorption

to that predicted for the excited state using a charge transfer multiplet calculation[29]. The charge transfer state differential absorption in Fig. 3-1d is calculated as the difference between the charge multiplet calculation and the ground state absorption.

The XUV absorption for the initial optically excited state is predicted using a charge transfer multiplet calculation by CTM4XAS (Reference 29) with a crystal field splitting of 10Dq = 1.45 eV following Reference 26. The optically induced charge transfer can be included by designating the final state to be Fe^{2+}, or by setting the difference between the core hole and Hubbard potential to 5 eV and the hopping parameter for the t2g and eg band to 2 eV. The latter introduces a ligand-hole on the oxygen site, introducing the optical charge transfer into the CTM4XAS calculation. In order to account for shorter Auger lifetimes at higher energy, the broadening of the x-ray transitions is represented by a Lorentzian with a linearly increasing width from 0.5 eV at 54.5 eV to 2 eV at 56 eV and a Fano asymmetry parameter of 3.5. Instrument resolution is included by a 0.5 eV width Gaussian. The differential absorption is calculated using the difference between the excited state, charge transfer model and the experimentally measured core-hole modified ground state in Fig. 3-1d. For the differential spectrum, a 0.5 eV Lorentzian broadening of the core-hole modified ground state absorption was also found to improve agreement, consistent with an electronic-excited state broadening.

The polaron state was predicted by convolving the ground state plus core hole XUV absorption with a three-fold energy splitting of the 3*p* core level using the values and weighting predicted for Fe^{3+} in FePO4 in Reference 30. The experimental ground state absorption was convolved with a three-fold delta function at energies of 0 eV, 1 eV, and 2.5 eV with weighting of 1/3, 1/2, and 1/6, respectively, which best-fit the data. The differential absorption was calculated by taking the difference between the polaron state absorption and the experimental ground state absorption.

3.3.2. Effects of Small Polaron Formation Dynamics on Transient XUV Absorption

Small polaron formation should have two distinct effects on the photoexcited XUV spectrum[30]. First, the small polaron creates an anisotropic expansion in the lattice as the excess charge self-traps, breaking the degeneracy of the Fe 3*p* levels and splitting their energies by several eV (final panel of Fig. 3-1b). This can also be thought of as resulting from the larger radius of the Fe^{2+} to Fe^{3+} ion. Second, the small polaron-induced localization of electron density on the Fe atom decreases the charge-transfer hybridization compared to the initial optically excited state, represented by the blue circles in Fig. 3-1a. The small polaron therefore has a conduction band density of states that more closely resembles the ground state Fe^{3+} atom before optical excitation than after[30]. That is, the small polaron state resembles the Fe^{3+} state, just with new XUV transitions from the degeneracy-split core levels, leading to a spectrum that appears broadened and red-shifted compared to the ground state plus core hole absorption (bottom panel of Fig. 3-1c). The small polaron's XUV spectrum can therefore be predicted by convolving the ground state plus core hole XUV absorption with a three-fold energy splitting of the *3p* core level of 0 eV, 1 eV and 2.5 eV, using the values predicted for Fe^{3+} in $FePO_4$ in Reference 30. In order to confirm that the transient signal comes a degeneracy split, Fe^{3+}-like state, and not from the charge-transfer hybridized Fe^{2+}-like state, the differential absorption predicted from a splitting of the *3p* core levels in the ground state is compared to that of the charge transfer hybridized state, reflecting the photoexcited electron and hole, in Fig. 3-2.

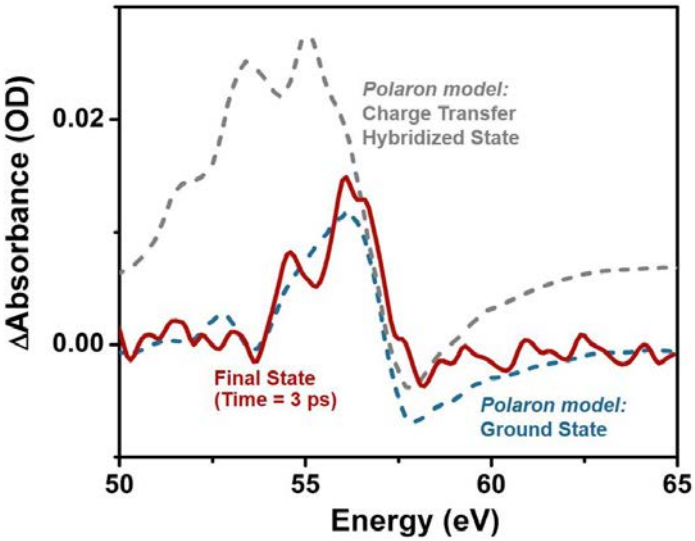

Figure 3-2: The differential absorption at *Time = 3 ps* is compared to two polaron models predicted using the splitting of the Fe *3p* core level in either the ground state or the excited, charge transfer hybridized state. The values of the core-level splitting and the assumed amplitude of the polaron state are taken to be the same for both models. Only the polaron model using the ground state can be related to the observed differential absorption. The model using the photoexcited charge transfer hybridized state, consisting of the photoexcited electron and hole, cannot describe the differential absorption. The discrepancy occurs because the charge transfer hybridized state is already red-shifted from the ground state. When the polaron-induced core-level splitting is applied, the spectrum is further redshifted. The change in absorbance below 57 eV is then overestimated compared to polaron splitting of the core-levels in the ground state.

The differential absorption at 2 ps after optical excitation is compared to the differential absorption predicted for the small polaron in Fig. 3-1d, confirming the presence of small polaron formation in hematite. The polaron state differential absorption in Fig. 3-1d is calculated as the difference between the polaron state and the ground state absorption. In both the experimental and predicted spectrum, the initial increase in absorption between 53 and 56 eV is blue-shifted and the decrease in absorption at 56-60 eV is reduced, leading to a blue-shift of the zero-crossing between the two features. This can be visualized by comparing the predicted polaron XUV spectrum to the ground and charge transfer hybridized XUV absorption in Fig. 3-1c. The blue-shift of the zero crossing provides a convenient reference to monitor the small polaron formation dynamics and is circled for clarity in the full 0-3 ps experimental differential absorption in Fig. 3-3a and lineouts in Fig. 3-3b show. The lineouts in Fig. 3-3b are averaged over the six nearest time points on a logarithmic scale.

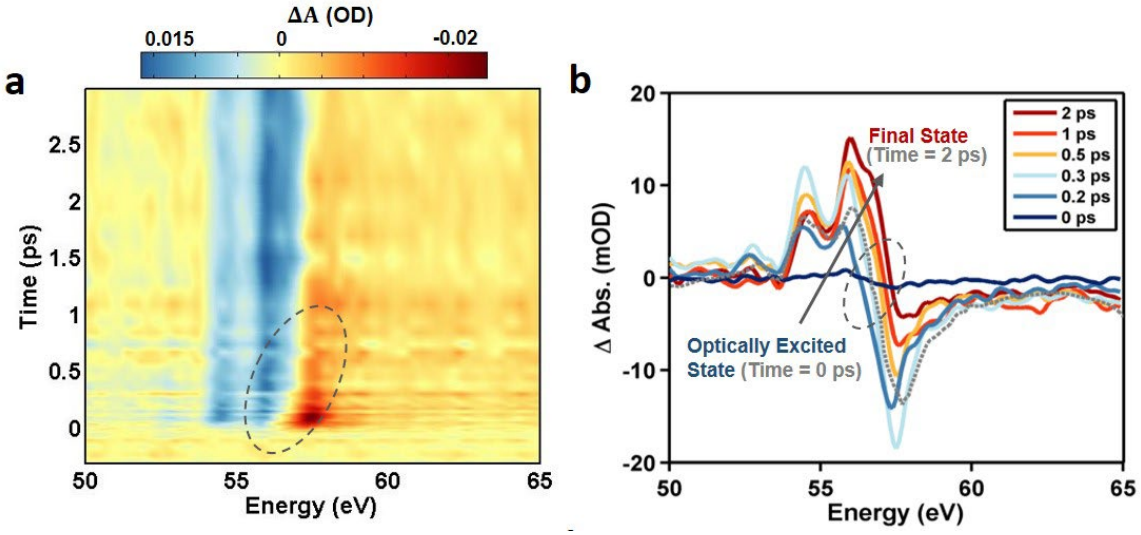

Figure 3-3: (a) Following excitation, the differential absorption reveals regions of increased and decreased absorption around 55 and 56 eV. The energy of the zero crossing between the areas of increased (blue) and decreased (red) absorption shifts on a 500 fs timescale and is circled for clarity. (b) Lineouts from the full differential absorption in the experimental data, averaged over the surrounding 6 time points on a logarithmic scale to isolate the key time periods during relaxation. The shift of the zero crossing around 56-58 eV is circled.

Since there are many possible decay pathways for an electronically excited state in a solid, it is important to rule out other possible explanations for the final state transient signal. Some possibilities include, carrier-induced[31], optical phonon[32-34], or acoustic phonon[35] renormalizations of the excited state. None of these possibilities can account for the measured spectral evolution because the expected energy shifts associated with them are only on the order of ~100 meV compared to the several eV expected for a small polaron[30]. Neither can trap-state effects, which would lead to an additional bleach or absorption at the pre-edge of the *Fe 3p* core level around 53 eV[36]. A mid-gap trap state would absorb lower energy photons, which is not observed in the experimental data. A visualization for each of these alternative explanations is provided in Fig. 3-4 for comparison with the measured differential absorption. It is clear from the comparisons that only the anisotropic, degeneracy split Fe^{3+} core levels, corresponding to small polaron formation, can explain the blue shift of the zero crossing.

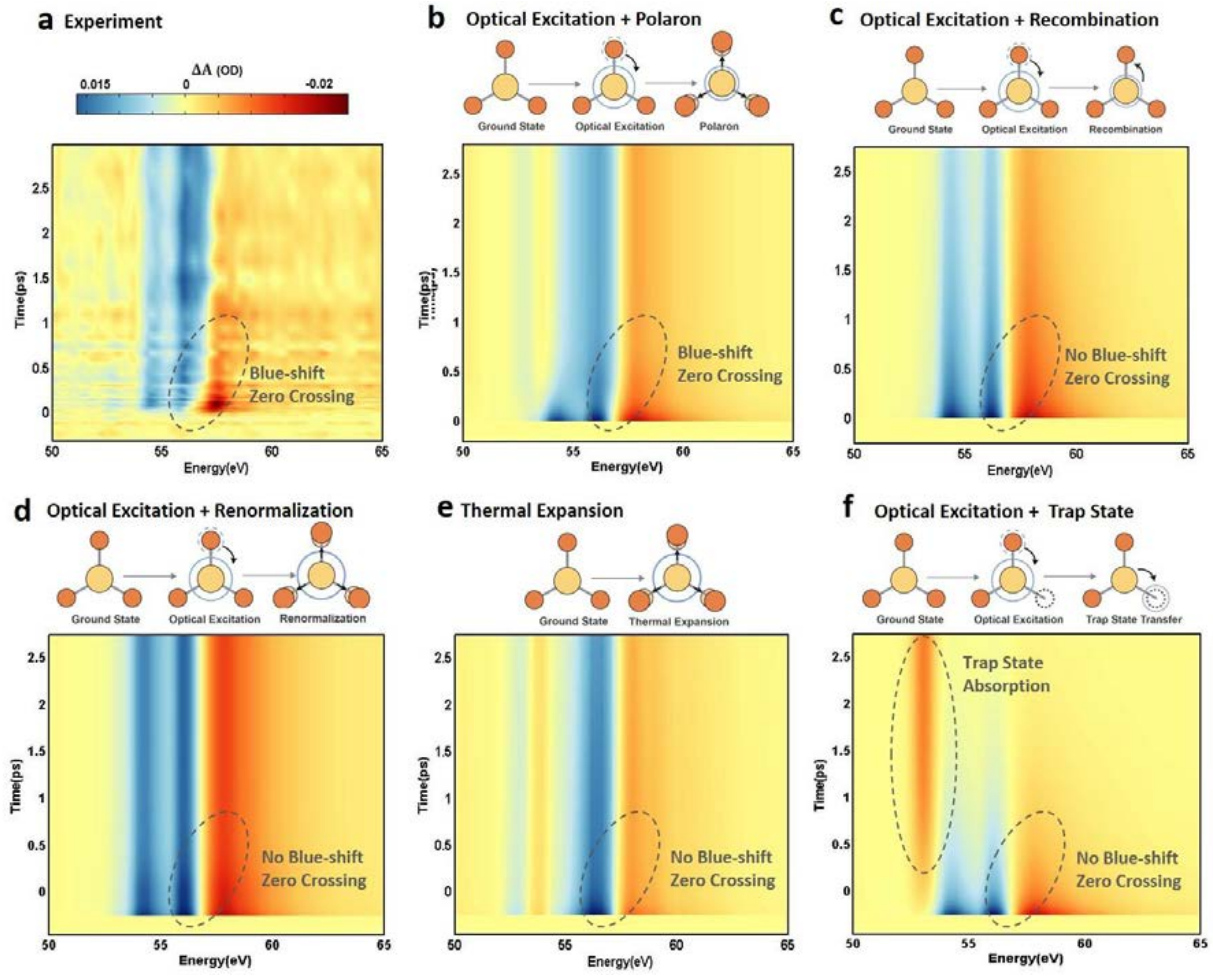

Figure 3-4: (a), The experimental data are compared to the possible recombination pathways after optical excitation. The feature that characterizes the formation of the polaron state is the blue-shift of the zero-crossing around 57 eV, circled for clarity in each plot. (b), Predicted differential absorption of the charge transfer state and polaron formation. (c), Charge transfer state and recombination. (d), Charge transfer state and renormalization representing carrier-carrier, optical phonon, or acoustic phonon based energy shifts. (e), Thermal lattice expansions. and (f), Charge transfer state followed by transfer to a defect state. The key regions of absorption are circled for clarity. Only for the polaron formation in (b) does the simulation reproduce the blue-shift of the zero crossing around 57 eV. The charge transfer and polaron state in (b) are simulated as described in the main text. Recombination in (c) is approximated by a triple exponential decay of the charge transfer state amplitude with time constants of 100 fs, 1 ps, and 10 ps, matching those commonly inferred from visible light transient absorption literature. Renormalization in (d) is approximated by a 200 fs, 500 meV red-shift of the charge transfer, representing the upper limit of the usually sub 100 meV renormalization caused by carrier-carrier, optical phonon, or acoustic phonon interactions as discussed in the main text. Thermal effects in (e) are approximated by a constant 500 meV red-shift of the ground state, representing lattice expansion. Trap state absorption in (f) is approximated by a 5 percent Gaussian decrease in absorption centered at 53 eV with a width of 500 meV and a 1 ps transfer time from the charge transfer state. A trap state absorption or bleach could occur at the pre-edge of either multiplet peak, however, in neither case is the experimental data in part (a) replicated as well as the polaron model of (b).

3.3.3. Polaron Formation Kinetics

The small polaron formation kinetics can be further examined by using a multivariate regression to decompose the experimental differential absorption into the charge-transfer hybridized and polaron states (Fig. 3-2b). The initial charge transfer hybridized state is taken as the *Time = 0 ps* differential absorption, while the final polaron state is taken as the *Time = 2 ps* differential. The amplitude versus time from the multivariate regression is shown in Figs. 3-5 as circles and squares for the charge transfer hybridized and polaron state, respectively. The charge-transfer hybridized state's amplitude rises within the 50 fs pulse-width, then decays into the small polaron state amplitude within several hundred femtoseconds. The transfer of amplitude from the hybridized state to the small polaron state stops within ~2-3 ps, indicating that small polaron formation has ceased. The residuals from the multivariate regression are reflective of the 5 mOD noise background of the experiment.

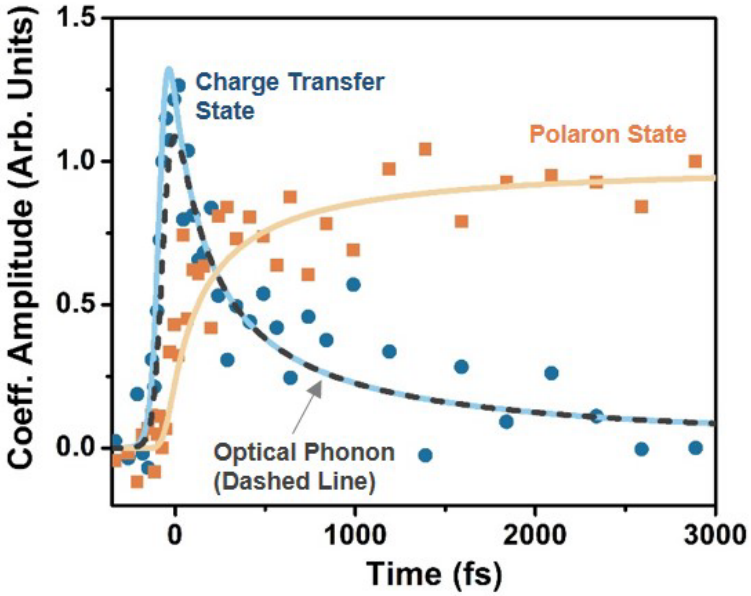

Figure 3-5: The experimental *Time=0 ps* and *Time=2 ps* slices are used to extract the amplitude of the charge transfer and small polaron state using a multivariate regression of the experimental data. These amplitudes are fit with a rate equation model for small polaron formation (solid lines). The effective phonon population that results from the rate equation model fit is shown for comparison as a dashed grey line. The phonon population is not directly measured in the experiment, so here it is scaled the same as the electron population, which would represent one electron scattering to create one phonon, which then combine to create one polaron.

Since the small polaron formation kinetics reflect localization of the photoexcited electrons, a two-temperature rate equation model[37] can be adapted to simultaneously describe the hot electron-phonon equilibration while also allowing a bimolecular recombination between the hot electrons and phonons to create a small polaron (Fig. 3-5a). An in-depth discussion for the motivation behind the use of the two-temperature rate model, along with its derivation, are given in the next subsection. In brief, the rate equation model has two rate constants that must be fit to the experimental data for electron-phonon scattering and small polaron formation (Fig. 3-5b). Additionally, two amplitude coefficients must be fit to the data to relate the change in the average population of electrons and small polarons to the amplitude in the measured transient XUV

spectrum. An average population is used since the relationship between the temperature of the electrons, phonons, and polarons and the resulting XUV spectral amplitudes is unknown. Using an average population ignores the momentum and energy-specific occupation of the density of states, as well as the dependence of the electron-phonon scattering rate on energy and momentum. This approximation is justified since the transient XUV traces represent the average change in population across all occupied energy and momentum states, so fitting the kinetics gives an equally averaged electron-phonon scattering rate or polaron formation rate.

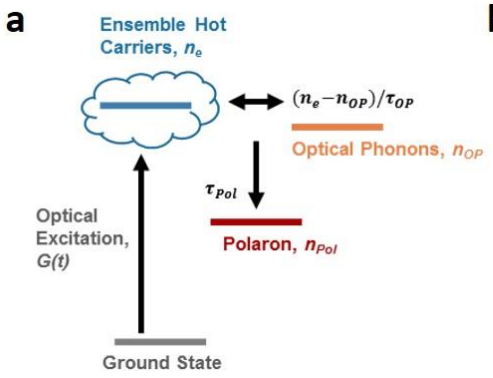

b

$$\frac{dn_e}{dt} = G(t) - \frac{n_e - n_{OP}}{\tau_{OP}} - \frac{n_{OP} n_e}{\tau_{Pol}}$$

$$\frac{dn_{OP}}{dt} = \frac{n_e - n_{OP}}{\tau_{OP}} - \frac{n_{OP} n_e}{\tau_{Pol}}$$

$$\frac{dn_{Pol}}{dt} = \frac{n_{OP} n_e}{\tau_{Pol}}$$

Figure 3-6: (a) Following excitation, the optically excited electrons in the charge transfer state thermalize by scattering off of and exciting optical phonons. The optical phonon and electron can then combine to create a polaron. (b) The rate equation model representing the polaron formation process. Here, *G(t)* represents the excitation source. *ni* and *τi* are the population and scattering time for *i=OP* the optical phonons, *i=e* the electrons, and *i=Pol* the polarons. The fit is performed using a robust, multi-start algorithm.

3.3.4. Derivation of Polaron Formation Rate Equation Model

Generally, hot electron-phonon equilibration is described in a two-temperature model, where the average occupation statistics of each system are described using their excited state temperature. The temperature is then related to the total energy of the system through the heat capacity, allowing a thermodynamic balance model to be used to describe the thermalization rates. In a two-temperature model, optical excitation first creates a hot electron population. Next, electron-phonon scattering thermalizes the hot electrons by creating a non-thermal optical phonon population. The transfer rate between the two systems is then determined by the electron-phonon scattering time, which must be fit to the data, as well as the relative temperature of each system.

Here, in addition to electron-phonon scattering, an optical phonon and electron can recombine to localize the electron in a small polaron, requiring an additional scattering time to be fit. The exact relationship between the temperature of hot electrons and the amplitude of the charge transfer hybridized state is unknown. Additionally, the optical phonon temperature cannot be directly measured. It is, however, expected that the charge transfer hybridized state amplitude will decrease as the hot electron distribution cools since optical phonon scattering changes the local electronic environment. To simultaneously describe hot carrier thermalization and polaron formation, the two-temperature model can instead be converted into a rate equation with average populations for the hot electrons and optical phonons.

Using the change in the average population instead of a temperature allows a bimolecular recombination term between an electron and optical-phonon to be included to describe small

polaron formation. The feedback between hot electron and hot phonon populations, the cooling rate of hot electrons by scattering with optical phonons, and the possibility of a hot electron combining with an excited phonon to create a polaron can then be described simultaneously. Inclusion of electron and optical phonon scattering with acoustic phonons in the rate equation model does not alter the dynamics because of the low temperatures (<350 K) and short time scales (<3 ps) modeled. Only the polar optical phonons take part in polaron formation, so acoustic phonons would not be expected to directly change the polaron formation rate, only indirectly on longer time scales by influencing the electron or optical phonon population. In this model, small polaron formation is treated statistically, ignoring the spatial nature of the electron and phonon that creates the polaron after excitation.

The hot electron occupation of a given band *k*, considering all optical phonon absorption and emission processes but ignoring state filling effects, is given by the differential equation:

$$\dot{n_k} = \frac{1}{\tau_{OP}}\left[-(\bar{n}+1)n_k + \bar{n}n_{k-q} + (\bar{n}+1)n_{k+q} - \bar{n}n_k\right] \tag{3.6}$$

where τ_{OP} is the electron-phonon scattering time, $\bar{n}$ is the average occupation of the phonon mode (Maxwell-Boltzmann distribution), and n_i is the electron occupation at the given momentum. The density of states and momentum dependence of τ_{OP} is neglected. The total phonon population for momentum q would then go as

$$\dot{n_q} = -\sum\nolimits_k \dot{n_{k,q}} \tag{3.2}$$

since a phonon is created or destroyed for each emission or absorption process. The transient XUV measurement only gives information about the ensemble-averaged occupation over all energy and momentum, as the transient amplitudes only show to what extent the charge transfer state and polaron state are occupied or not, independent of energy and momentum. To simulate the experimental observables, the sum over all the k and $k\pm q$ connected states can be performed. Assuming the excited electron populations are described by a Boltzmann distribution, this allows Equation 1 to be rewritten as the difference in population between any two states separated by phonon momentum q as

$$\sum \Delta\dot{n_k} = \sum \frac{1}{\tau_{OP}}[-(\bar{n}+1)\Delta n_k + \bar{n}\Delta n_k] = -\sum \frac{\Delta n_k}{\tau_{OP}} \tag{3.3}$$

where $\Delta n_k = n_{k+q} - n_k$.

The sum gives an ensemble averaged change between any two states separated by a phonon of momentum q with an average scattering time of τ_{OP}. To turn Equation 3.3 into a thermodynamic balance model, the sum can be done over the energy of each state *k*, giving the ensemble average of the change in energy of the system. This leads to the Two Temperature Model as

$$\frac{dU_e}{dt} = -\frac{C_{V,e}(T_e)\cdot(T_e - T_{OP})}{\tau_{OP}} \tag{3.4}$$

$$\frac{dU_{OP}}{dt} = \frac{C_{V,e}(T_e)\cdot(T_e - T_{OP})}{\tau_{OP}} \tag{3.5}$$

where $U = C_V(T) \cdot T$ is the energy for each system at constant-volume through the specific heat $C_V(T)$ and temperature T. In equation (3.4) and (3.5) the kinetics are summarized in the time dependent change of the average system temperature and dependence on temperature of the specific heat. Here, the relationship between the temperature of the electron, phonon, and polaron and the measured amplitude is unknown. The heat capacity of the polaron is also unknown. Therefore, the sum in equation 3 can instead be taken only over the population, giving the average change in population between any two k states separated by phonon momentum q as

$$\dot{n_e} = -\frac{n_e - n_{OP}}{\tau_{OP}} \tag{3.6}$$

$$\dot{n_{OP}} = -\frac{n_e - n_{OP}}{\tau_{OP}} \tag{3.7}$$

This allows the polaron to be added in as a bimolecular change in both the electron and hole population. The polaron formation time then describes taking an excited electron at some k and a phonon at some q and removing that population from the ensemble excited state.

$$\dot{n_e} = -\frac{n_e - n_{OP}}{\tau_{OP}} - \frac{n_e \cdot n_{OP}}{\tau_{Pol}} \tag{3.8}$$

$$\dot{n_{OP}} = \frac{n_e - n_{OP}}{\tau_{OP}} - \frac{n_e \cdot n_{OP}}{\tau_{Pol}} \tag{3.9}$$

$$\dot{n_{Pol}} = \frac{n_e \cdot n_{OP}}{\tau_{Pol}} \tag{3.10}$$

Equations 3.8-3.10 are fit to the experimental data to obtain the electron-phonon scattering time, the polaron formation time, and two amplitude fit coefficients to relate the predicted population to the change in the experimental differential absorption for the polaron and charge transfer hybridized states. The fitting was done using a robust, multi-start fit method to find the global minimum.

A fit to the experimental data using the rate equation model is shown as the solid lines in Fig. 3-5. The fit gives an electron-phonon scattering rate of 20-30 ps^{-1} (30-60 fs) and an initial small polaron bimolecular formation rate of 11±0.5 ps^{-1} (90±5 fs), similar to previous reports for polaron formation[22-24]. The competition between electron-phonon scattering to create phonons, then subsequent removal of electrons and phonons in the generation of polarons, leads to the fast rise in small polaron population followed by a slowing down of polaron formation at ~3 ps in Fig. 3-5. The large uncertainty of the electron-phonon scattering rate originates in the 50 fs excitation pulse width, which represents the instrument response time and is accounted for in the fit. The extracted electron-phonon scattering rate of 20-30 ps^{-1} (30-60 fs) is consistent with inter- and intra-valley scattering in polar semiconductors where longitudinal optical (LO) phonons dominate[38-40], as well as with hematite's highest energy optical phonon frequency (659 cm^{-1})[41,42].

The kinetics of Fig. 3-5 suggests that, after excitation, the optically excited electrons in the charge transfer hybridized state quickly scatter off of optical phonons. This optical phonon population then begins creating small polarons on a 100 fs time scale by combining with the excited electrons. As the electron and phonon populations are consumed, the small polaron

formation slows down, with the majority of electrons and optical phonons combined within ~2-3 ps following optical excitation. Although the phonon population is not directly measured, for visualization it is shown as a dotted line in Fig. 3-5 using the same fit amplitude as the electron population.

3.3.5. Wavelength Dependence of Small Polaron Formation Dynamics

To determine the impact of multi-phonon effects arising from excess carrier energy, the procedure of Fig. 3-5 was repeated for four pump wavelengths covering the visible light absorption of hematite, at wavelengths of 560 nm, 520 nm, 480 nm, and 400 nm. The transients for all four wavelengths, along with the multivariate regression based fits, are shown in Figs. 3-7 and 3-8, respectively. The transients show that small polaron formation takes place at all excitation wavelengths and at similar timescales, with the blue-shift of the zero-crossing occurring within 500 fs for all cases. The fits at each wavelength also demonstrate that most of the excited carriers become self-trapped within a few hundred femtoseconds.

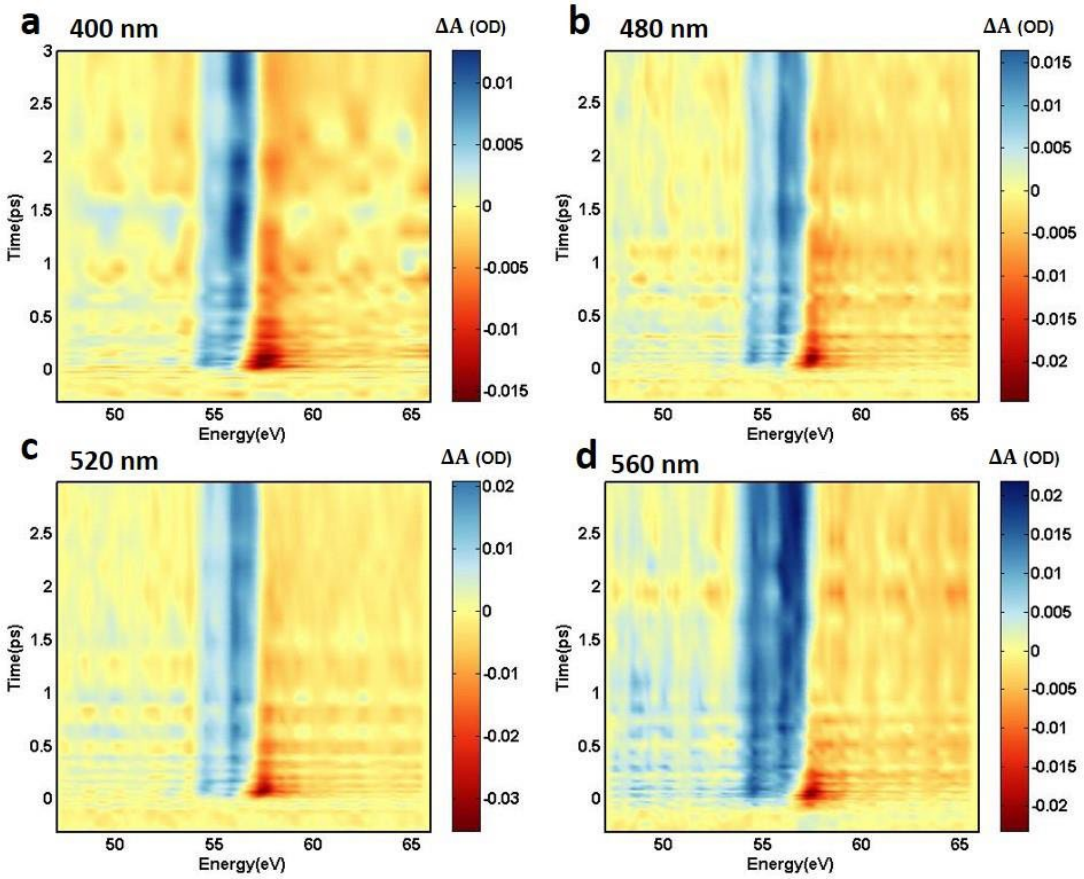

Figure 3-7: At each pump wavelength indicated on the figure, the zero-crossing point near 56-57 eV between the positive and negative features is seen to blue-shift within ~500 fs. The blue-shift consistently stops within ~2-3 ps.

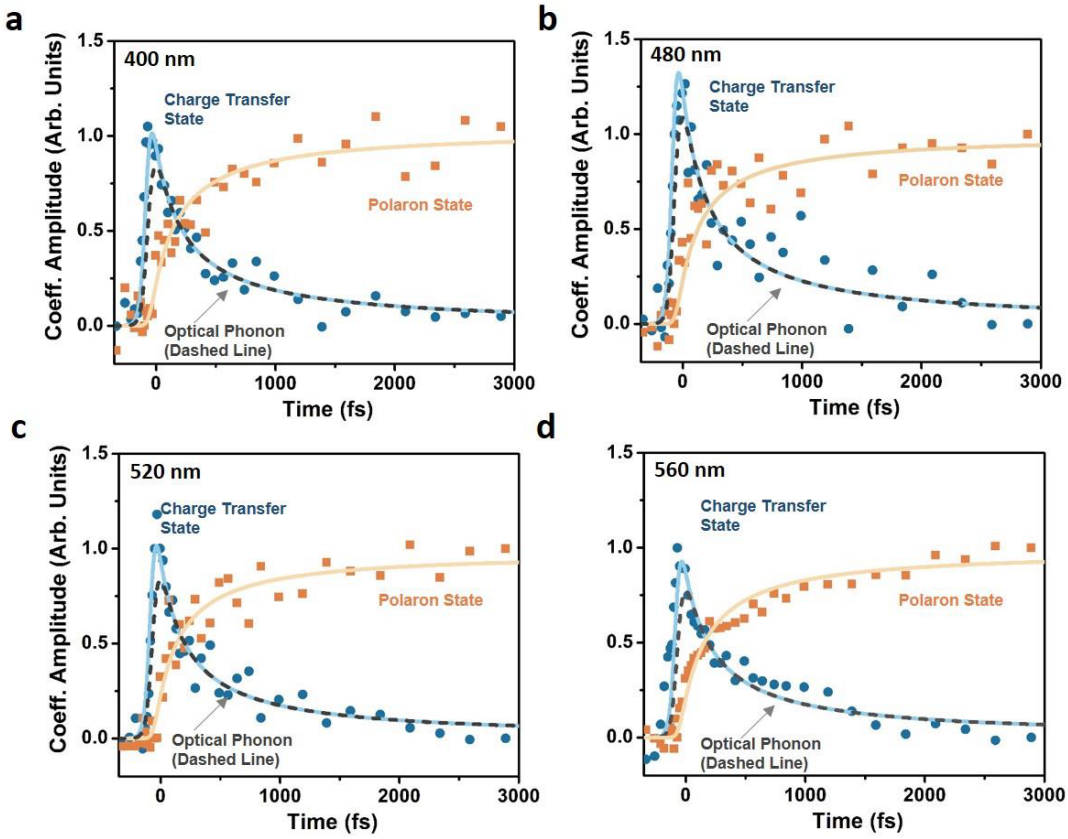

Figure 3-8: The multivariate regression amplitudes for the charge transfer hybridized and polaron state (circles and squares, respectively) are shown for each pump wavelength indicated on the figure, along with the fit (solid lines) using the rate equation model described above. The scaled phonon population that results from the rate equation model fit is shown for comparison as a dashed grey line. The phonon population is not directly measured in the experiment, so here it is scaled the same as the electron population, which would represent one electron scattering to create one phonon, which then creates one polaron. The deviations from this picture caused by multi-phonon effects are discussed in the text. For each pump wavelength the fitted electron-phonon scattering constant is 30-60 fs, with the insensitivity to electron-phonon scattering time coming from the 50 fs instrument response function of the pump pulse. The fitted polaron formation times are 97±4 fs for 400 nm excitation, 87±5 fs for 480 nm excitation, 88±3 fs for 520 nm excitation, and 100±5 fs for 560 nm excitation.

The small polaron formation and decay process is shown schematically in Fig. 3-9a. The fitted small polaron formation rate versus excitation wavelength is shown in Fig. 3-9b and found to be fastest at 2.5 eV photoexcitation energy. The excitation wavelength dependence of the small polaron formation rate reflects the energy necessary to localize the conduction band electron and is expected to go as[22,43,44]

$$k_{st} = Ae^{-(\Delta\varepsilon + E_{rel})^2/4E_{rel}k_BT} \tag{3.17}$$

where the prefactor A is related to the coupling between the mobile and localized states, $\Delta\varepsilon$ is the exothermicity of excited carriers ($E_{pump} - E_g$), E_{rel} is the relaxation energy associated with carrier self-trapping by polaron formation, and k_BT the thermal energy. Equation 3.11 reflects the

predictions from Marcus theory, namely, if the excited carrier has too little or too much excess energy, the formation rate will increase[22]. Fitting Equation 3.11 to the formation rate within the lower t_{2g} conduction band[7] gives a small polaron localization energy of -0.4±0.05 eV, close to a previously measured energy of -0.3 eV[45]. An elevated temperature of 600 K, roughly double the <350 K reached by optical excitation, is required to fit the data. The elevated temperature arises because Equation 3.11 is classically derived for molecular systems and does not properly account for the optical phonon modes in the solid[22]. If the formation energy is fit considering the narrow t_{2g} and e_g conduction bands as one band, outside the validity of Equation 3.11, the localization energy fit is doubled to -0.6±0.05 eV and the temperature fit more than quadrupled from the expected temperature to 1600 K.

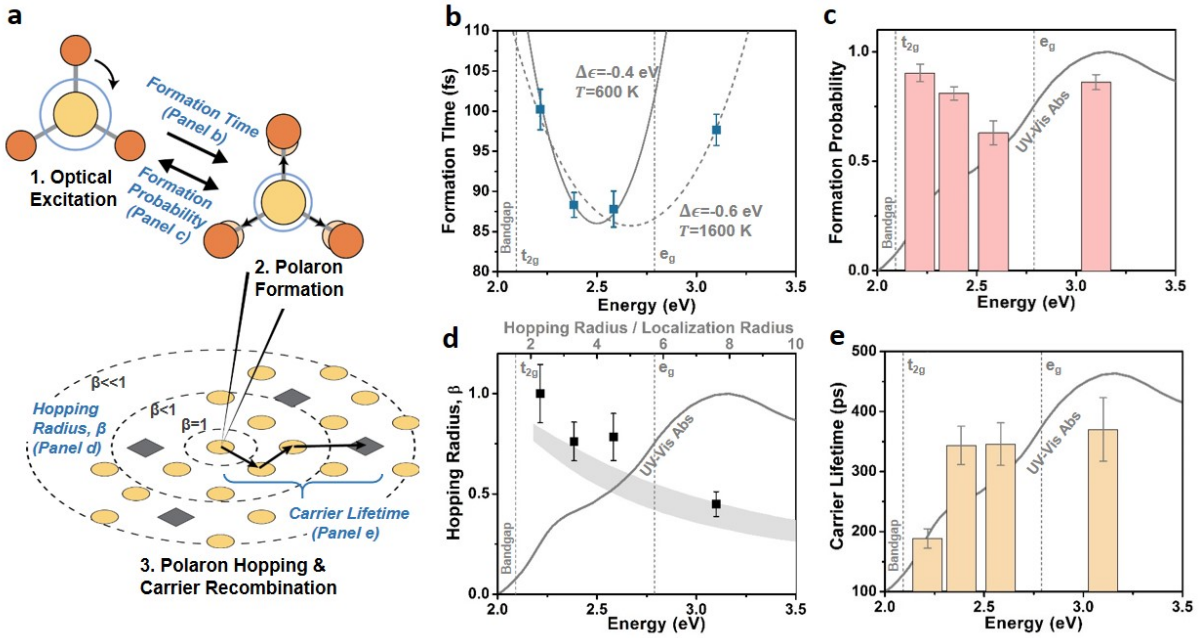

Figure 3-9: (a) Schematic explanation of the small polaron formation and decay, including representations of (b) the formation time, (c) the excitation and de-excitation process that determines the formation probability, and (d) the hopping and recombination process that determines (e) the measured excited state lifetime. (b) The small polaron formation rate is plotted versus pump photon energy. The parabolas represent the small polaron formation energy (Δε) and effective lattice temperature within the conduction bands of Fe2O3. Fits that consider the narrow t2g and eg conduction bands as separate (solid line) and consolidated (dashed line) are shown. (c) The relative polaron formation probability versus excitation wavelength from the rate equation model. Parts (b) and (c) reveal that at the band edge of Fe2O3 the majority of excited carriers are localized as small polarons. As the excess energy of excited carriers increase, the hot-optical phonon population increases, decreasing the effects of small polaron localization. (d) The best-fit exponential stretching parameter versus excitation wavelength, related to the hopping radius as outlined in Reference 46. The grey area and top axis are a qualitative comparison to the predicted dependence of β on the ratio of hopping radius to localization radius from Reference 46. The grey area and top axis are a guide to the eye and are not quantitative. (e) The best-fit lifetime from the stretched exponential model versus excitation wavelength. Parts (d) and (e) reveal that as the excitation energy is increased, the larger phonon bath promotes more hopping, resulting in a longer excited state lifetime. In each panel the error bars represent the standard error of the best-fit parameter. The positions of the conduction band edges and the UV-Vis absorption are shown for reference in panels (c)-(e).

The small polaron formation probability is shown in Fig. 3-9c, and represented schematically in Fig. 3-9a in its relation to the formation rate. The polaron formation probability is calculated as the ratio between the amplitude fit coefficients, which relate the population predicted by the rate equation model to the measured transient XUV amplitudes. As the excitation energy is decreased, the amplitude fit coefficients are adjusted to reflect the number of polarons produced from the initial population of electrons. Given that the same number of electrons are excited for each pump wavelength, it would be expected that an increase in polaron formation rate would translate to either an increase in the number of polarons or no change if the electron population is rate limiting. Fig. 3-9c demonstrates neither case is true, as can also be seen by comparing the amplitudes of the *Time = 0 ps* and *Time = 2 ps* states in the kinetics of Fig. 3-8, at which time the polaron formation has reached a steady state. Instead, the polaron formation probability decreases with increasing energy above the t_{2g} band edge, increasing again at the e_g band edge. This trend reflects the increasing number of optical phonons created per excited electron with excess energy above the relevant conduction band edge. This suggests that when more hot optical phonons are present, it becomes more likely that the phonon population will re-excite or interfere with polaron formation, decreasing the formation probability. Fig. 3-9c therefore reflects the multi-phonon effects not included in the rate equation model and suggests that faster polaron formation rates (Fig. 3-9b) do not necessarily lead to larger final polaron state amplitudes (Fig. 3-9c).

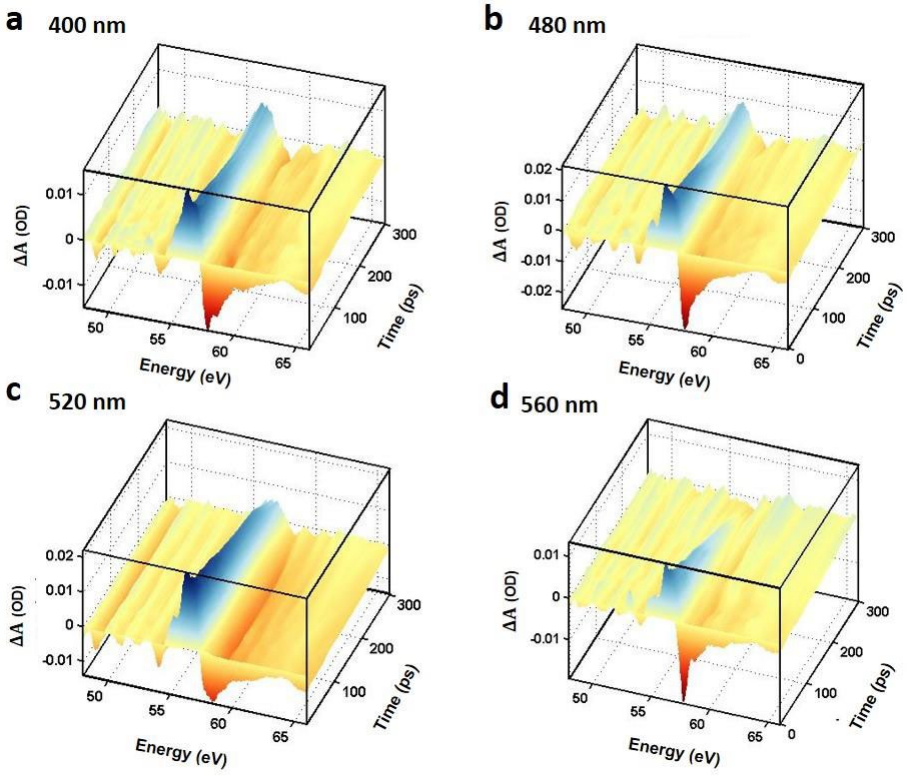

Figure 3-10: The lifetime of the polaron signal (blue, positive change in absorption) decreases with increasing excitation wavelength. At 560 nm excitation, the polaron signal has decayed to within noise level by ~250 ps.

The decays of the differential absorption on a 300 ps timescale (Fig. 3-10) further suggest the impact of the non-thermal phonon bath. For 560 nm excitation, the differential absorption signal disappears within the noise level of the experiment by 300 ps. For 520 nm, 480 nm, and 400 nm excitation the polaron signal still exists at 300 ps, although largely reduced in amplitude, indicating decay of the polaron state. The polaron state absorption represents the excited carrier – polaron pair. The measured decay and disappearance of the polaron state, and the absence of any new spectral features such as a trap-state or charge-transfer state absorption, confirms that the excited carriers are recombining while self-trapped as a small polaron.

The measured long time scale dynamics are best fit using the stretched exponential theory for polaron-hopping between trap states[46,47],

$$n(t) = A \cdot \exp\left(-\left(\frac{t}{\tau}\right)^{\beta}\right), \tag{3-18}$$

where t is the time, τ is the decay constant, and β the stretching parameter. The stretched exponential fit is shown in Fig. 3-11 and the best-fit parameters are tabulated in Table 3-1. The decay dynamics are fit starting at the 2-3 ps timescale during which polaron formation reaches a steady state. In polaron-hopping-based decay, the stretching factor β corresponds to the possible hopping radius relative to the localization radius of the polaron (shown schematically in Fig. 3-9a). The stretching factor β in the exponential represents the sum over all possible hopping paths to a terminal defect site[46,47]. When β is one, the stretched exponential reduces to an exponential decay and the excited carrier decays almost on-site with a defect-state determined lifetime of τ. As β becomes smaller than one, more hopping paths are sampled before recombination, and the excited state population lives longer as compared to the single-site case. In other words, the farther the excited carrier can hop before recombination, the more the decay dynamics change from a single exponential.

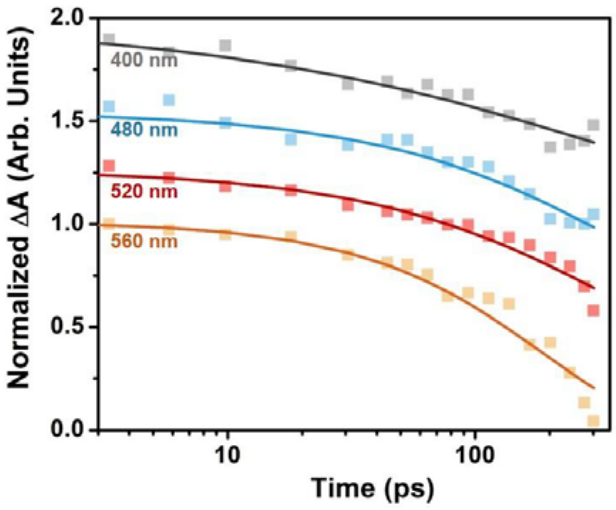

Figure 3-11: Squares represent the experimental data, calculated by summing over the polaron peak in Fig. 3-10. Solid lines represent the best fit using the stretched exponential function described above. The excited-state lifetime and the hopping radius increase with increasing excitation energy. The best-fit parameters are tabulated in Table 3-1. The curves have been offset for clarity.

Wavelength (nm)	Amplitude, A	Lifetime, τ (ps)	Stretching Factor, β
400	0.98±0.04	370±50	0.45±0.06
480	0.94±0.03	345±35	0.78±0.10
520	0.96±0.03	344±30	0.76±0.1
560	1.01±0.04	189±15	1±0.15

Table 3-1: Best fit coefficients for the stretched exponential function (Eq. 3-12). Error bars represent the standard error of the fit.

In agreement with polaron-hopping theory, as excitation energy is increased in the measured data, increasing the non-thermal phonon bath, the best-fit parameter β decreases (Fig. 3-9d), representing increased hopping (Fig. 3-9a). In Fig. 3-9d the grey shaded area and top axis represent qualitatively how β changes with the ratio of the hopping radius to the localization radius (adapted from Reference 46). The grey area and top axis are shown only as a trend-line and are not a quantitative comparison. For 560 nm excitation, β is best-fit to one, conveying a fast recombination with little hopping. For 400 nm excitation, the best-fit of β decreases to ~0.4, indicating an increased hopping radius before recombination. In agreement with the increased hopping radius, the best-fit lifetime in the stretched exponential also increases with increasing excitation energy (Fig. 3-9e). Figs. 3-11d and 3-11e suggest that as the excitation energy is increased, more excess energy goes to the lattice, allowing hopping at a frequency faster than the recombination time of the occupied site. This leads to an increase of the excited state lifetime with increasing excitation energy.

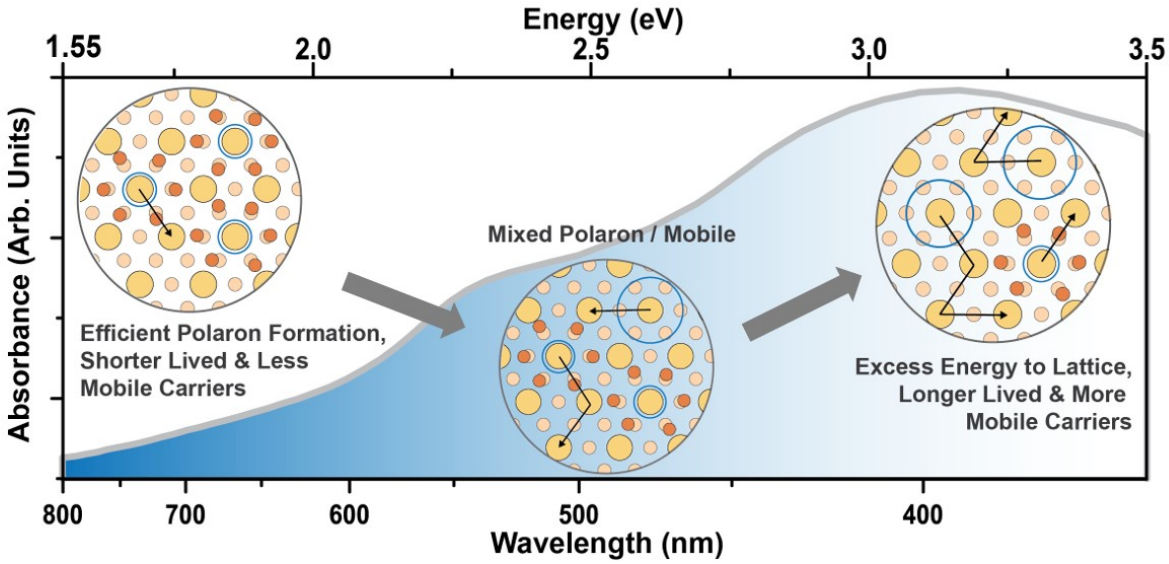

Figure 3-12: At excitation wavelengths near the band edge, polaron formation is efficient. Excited carriers have little excess energy, so the non-thermal phonon bath is small, leading to less polaron hopping. This results in trapping of excited state carriers, preferentially at defect sites[21,46], which leads to faster recombination times. As the excitation energy is increased, the excited state polaron formation becomes less efficient, and the non-thermal phonon bath increases. This leads to an increased polaron hopping, and on average, the excited state carriers should have a higher mobility and longer lifetime.

The wavelength dependence of small polaron formation across hematite's visible-light absorption, and thus the expected impact on photoconversion efficiency, can be summarized as shown in Fig. 3-12. Near the hematite band edge, the majority of carriers are localized as small polarons following photoexcitation. The excited carriers mostly exist as polarons (Fig. 3-9c) and complete fewer hops before recombining (Fig. 3-9d). This will lead to a lower excited state mobility and lifetime. As the excitation energy is increased, more optical phonons are created per excited carrier, and the equilibrium between mobile carriers and polarons shifts with fewer polarons being formed. As more excess energy goes to the lattice, the non-thermal phonon bath increases the hopping rate of the polaron. This leads to an increased hopping radius for the localized carrier (Fig. 3-9d), prolonging recombination (Fig. 3-9e), and increasing the average excited state mobility. These trends match the competition between recombination and charge extraction in the internal quantum efficiency for hematite[48]. The internal quantum efficiency is often referred to as the absorbed photon-to-current efficiency (APCE).

The transient absorption spectra can only be replicated using a rate equation model for short time scales that incorporates bimolecular formation of a small polaron. The transient absorption spectra can only be replicated for long time scales using a stretched exponential model that describes a random hopping terminated at a defect site. If the decay timescales are extracted at a single XUV probe energy, thus ignoring the structure of the XUV absorption spectrum, the data can be fit with a triple-exponential model. For example, the time constants obtained from a fit at an energy of 57.5 eV (peak of the bleach) following 480 nm excitation are 78±16 fs, 1.6±0.1 ps, and >100 ps. These time constants reflect those reported in the visible light transient absorption literature[4-10], which are commonly attributed to hot electron relaxation (~100s fs), followed by trapping (~1 ps), and finally relaxation back to the ground state (~100s ps). However, within the experimental noise, the measured differential XUV spectrum does not have the pre-edge increase or decrease in absorption around 53 eV that would be associated with trap or mid-gap states[36], nor can it be reproduced by triple-exponential recombination of the charge-transfer hybridized state alone (Fig. 3-4). The polaron state is measured to persist through the decay of the differential absorption. While defect states themselves undeniably affect the photoconversion efficiency, most likely serving as the recombination sites in the random walk of the hopping polaron[21,46], the results here suggest that small polarons are primarily responsible for the ultrafast trapping processes and decreased mobility measured in hematite, and not the mid-gap or surface states themselves. The critical difference is that even when trap states are passivated, small polaron localization will still exist, still acting as an upper bound on the photoconversion efficiency in hematite.

3.4 Conclusions

The results of this chapter therefore support recent suggestions that small polaron formation is what is limiting bulk transport and recombination in even the highest efficiency hematite photoelectrodes to date[6,19,20]. If photoexcited carriers are not trapped as a small polaron, their mobility is determined by the curvature of the energy band and its effective mass, just as in most semiconductors. Once localized as a small polaron, however, the effective mass greatly increases and transport occurs by thermally activated hopping, most often terminating at defect sites[21,46].

The limiting effect of small polarons may be further evidenced in that the photoconversion efficiency of hematite[1-3,11-17] does not increase proportionately with the optical absorption near 2.1-2.5 eV (500-600 nm) in the t_{2g} conduction band, peaks near 2.5 to 3 eV (400-450) nm, then drops or levels off for higher excitation in the e_g band. This is best visualized by examining the

absorbed photon-to-current efficiency (APCE), which represents the internal quantum efficiency, for hematite such as shown in Reference 48. The APCE represents the competition between charge extraction and recombination for a photoexcited carrier. For excitation wavelengths near hematite's band edge, small polaron formation is largest, and a smaller hopping radius is measured before recombination. The average carrier lifetime and mobility will therefore be smaller, decreasing the internal quantum efficiency in agreement with the APCE[48]. As the excitation energy is increased, small polaron formation decreases, and the hopping and excited state lifetime increase. The average carrier lifetimes and mobility will therefore be improved compared to band-edge excitation, increasing the internal quantum efficiency, again in agreement with the APCE[48]. In other words, these results indicate that the photoconversion efficiency will deviate from the optical absorption trend at excitation wavelengths where small polaron formation is high and the small polaron's hopping-rate is low.

3.5 Bibliography

1. Lin, Y. *et al*. Hematite-based solar water splitting: Challenges and opportunities. *Energy Environ. Sci.* **4,** 4862 (2011).
2. Sivula, K. *et al*. Solar water splitting: Progress using hematite (α-Fe2O3) photoelectrodes. *ChemSusChem* **4,** 432–449 (2011).
3. Tamirat, A.G. *et al*. Using hematite for photoelectrochemical water splitting: A review of current progress and challenges. *Nanoscale Horiz.* **1**, 243-267 (2016).
4. Cherepy, N.J. *et al*. Ultrafast studies of photoexcited electron dynamics in γ-and α-Fe2O3 semiconductor nanoparticles. *J Phys. Chem. B*, **102**, 770-776 (1998).
5. Barroso, M. *et al*. Charge carrier trapping, recombination and transfer in hematite (α-Fe2O3) water splitting photoanodes. *Chem. Sci.* **4,** 2724 (2013).
6. Pendlebury, S.R. *et al.* Ultrafast charge carrier recombination and trapping in hematite photoanodes under applied bias. *J. Am. Chem. Soc.* **136**, 9854-9857 (2014).
7. Sorenson, S. *et al*. Ultrafast carrier dynamics in hematite films: The role of photoexcited electrons in the transient optical response. *J. Phys. Chem. C* **118**, 23621-23626 (2014).
8. Joly, A.G. *et al.* Carrier dynamics in α-Fe2O3 (0001) thin films and single crystals probed by femtosecond transient absorption and reflectivity. *J. Appl. Phys.* **99**, 053521 (2006).
9. Fitzmorris, B. C. *et al.* Ultrafast transient absorption studies of hematite nanoparticles: The effect of particle shape on exciton dynamics. *ChemSusChem* **6,** 1907–1914 (2013).
10. Nadtochenko, V. a *et al.* Femtosecond relaxation of photoexcited states in nanosized semiconductor particles of iron oxides. *Russ. Chem. Bull. Int. Ed.* **51,** 457–461 (2002).
11. Le Formal, F. *et al*. Back electron–hole recombination in hematite photoanodes for water splitting. *J. Am. Chem. Soc.* **136**, 2564-2574 (2014).
12. Braun, A. *et al.* Direct observation of two electron holes in a hematite photoanode during photoelectrochemical water splitting. *J. Phys. Chem. C* **116**, 16870-16875 (2012).
13. Zandi, O. & Hamann, T.W. The potential versus current state of water splitting with hematite. *Phys. Chem. Chem. Phys.* **17**, 22485-22503 (2015).
14. Gui, Q. *et al.* Enhanced photoelectrochemical water splitting performance of anodic TiO2 nanotube arrays by surface passivation. *ACS Appl. Mater. Interfaces* **6,** 17053-17058 (2014).
15. Cesar, I. *et al*. Influence of feature size, film thickness, and silicon doping on the performance of nanostructured hematite photoanodes for solar water splitting. *J. Phys. Chem. C* **113**, 772-782 (2008).
16. Sivula, K. Metal oxide photoelectrodes for solar fuel production, surface traps, and catalysis. *J. Phys. Chem. Lett*. **4**, 1624-1633 (2013).
17. Ling, Y. & Li, Y. Review of Sn-doped hematite nanostructures for photoelectrochemical water splitting. *Part. Part. Syst. Charact.*, **31**, 1113-1121 (2014).

18. Shen, S. *et al*. Hematite heterostructures for photoelectrochemical water splitting: Rational materials design and charge carrier dynamics. *Energy Environ Sci*, **9**, 2744-2775 (2016).

19. Rettie, A.J. *et al*. Unravelling small-polaron transport in metal oxide photoelectrodes. *J. Phys. Chem. Lett.* **7,** 471-479 (2016).

20. Warren, S.C. *Photoelectrochemical Hydrogen Production*, 293-316 (Springer US, 2012).

21. Emin, D. *Condensed Matter Physics,* 16-34 (Springer New York, 1987).

22. Ge, N.H. *et al.* Femtosecond dynamics of electron localization at interfaces. *Science* **279**, 202-205 (1998).

23. Wang, T. *et al*. From two-dimensional electron gas to localized charge: Dynamics of polaron formation in organic semiconductors. *Phys. Rev. B* **91,** 041201 (2015).

24. Muntwiler, M. & Zhu, X.Y. Formation of two-dimensional polarons that are absent in three-dimensional crystals. *Phys Rev. Lett.* **98**, 246801 (2007).

25. Katz, J.E. *et al.* Electron small polarons and their mobility in iron (oxyhydr) oxide nanoparticles. *Science* **337,** 1200-1203 (2012).

26. Vura-Weis, J. *et al.* Femtosecond M_{23}-edge spectroscopy of transition-metal oxides: Photoinduced oxidation state change in α-Fe2O3. *J. Phys. Chem. Lett.* **4**, 3667-3671 (2013).

27. Bosman, A.J. & Van Daal, H.J. Small-polaron versus band conduction in some transition-metal oxides. *Adv. Phys.* **19**, 1-117 (1970).

28. De Groot, F. & Kotani, A. *Core Level Spectroscopy of Solids*, 133-142 (CRC press, 2008).

29. Stavitski, E. & de Groot, F. M. F. The CTM4XAS program for EELS and XAS spectral shape analysis of transition metal L edges. *Micron* **41,** 687–694 (2010).

30. Wang, Z. & Bevan, K. H. Exploring the impact of semicore level electronic relaxation on polaron dynamics: An adiabatic ab initio study of $FePO_4$. *Phys. Rev. B* **93,** 024303 (2016).

31. Tränkle, G. *et al.* Dimensionality dependence of the band-gap renormalization in two-and three-dimensional electron-hole plasmas in GaAs. *Phys. Rev. Lett.* **58**, 419 (1987).

32. Rethfeld, B. *et al*. Timescales in the response of materials to femtosecond laser excitation. *Appl. Phys. A* **79,** 767-769 (2004).

33. Stampfli, P. & Bennemann, K.H. Theory for the laser-induced femtosecond phase transition of silicon and GaAs. *Appl. Phys. A* **60**, 191-196 (1995).

34. Bennett, B.R. *et al*. Carrier-induced change in refractive index of InP, GaAs and InGaAsP. . *IEEE J. Quant. Electron.* **26,** 113-122 (1990).

35. Rose-Petruck, C. *et al.* Picosecond–milliångström lattice dynamics measured by ultrafast X-ray diffraction. *Nature* **398**, 310-312 (1999)

36. Santomauro, F.G. *et al.* Femtosecond X-ray absorption study of electron localization in photoexcited anatase TiO_2. *Sci. Rep.* **5**, 14834 *(2015)*.

37. Van Driel, H.M. Kinetics of high-density plasmas generated in Si by 1.06-and 0.53-μm picosecond laser pulses. *Phys. Rev. B* **35**, 8166 (1987).

38. Becker, P.C. *et al.* Femtosecond intervalley scattering in GaAs. *Appl. Phys. Lett.* **53**, 2089-2090 (1988).

39. Lin, W.Z. *et al*. Femtosecond absorption saturation studies of hot carriers in GaAs and AlGaAs. *IEEE J. Quant. Electron.* **24**, 267-275 (1988).

40. Fluegel, B.D. *et al.* Experimental and theoretical investigation of femtosecond carrier relaxation in CdSe. *Solid State Commun.* **83**, 17-19 (1992).

41. Shim, S.-H. & Duffy, T. S. Raman spectroscopy of Fe_2O_3 to 62 GPa. *Am. Mineral.* **87,** 318–326 (2001).

42. Jubb, A.M. & Allen, H.C. Vibrational spectroscopic characterization of hematite, maghemite, and magnetite thin films produced by vapor deposition. *ACS Appl. Mater. Interfaces 2*(10), pp.2804-2812 (2010).

43. Holstein, T. Studies of polaron motion. *Ann. Phys. (N. Y).* **8,** 325–342 (1959).

44. Marcus, R. A. & Sutin, N. Electron transfers in chemistry and biology. *BBA Reviews On Bioenergetics* **811,** 265–322 (1985).

45. Peng, H. & Lany, S. Semiconducting transition-metal oxides based on d5 cations: Theory for MnO and Fe_2O_3. *Phys. Rev. B - Condens. Matter Mater. Phys.* **85,** 1–5 (2012).

46. Sturman, B. *et al*. Origin of stretched exponential relaxation for hopping-transport models. *Phys. Rev. Lett.* **91**, 176602 (2003).

47. Merschjann, C. *et al*. Nonexponential relaxation dynamics of localized carrier densities in oxide crystals without structural or energetic disorder. *Phys. Rev. B* **84**, 052302 (2011).

48. Lin, Y. *et al*. Nanonet-based hematite heteronanostructures for efficient solar water splitting. *J. Am. Chem. Soc.*, **133**, 2398-2401 (2011).

49. Gialanella, S. *et al.* On the goethite to hematite phase transformation. *J. Therm. Anal. Calorim.* **102**, 867-873 (2010).

Chapter 4

Hot Phonon and Carrier Relaxation in Si(100) Determined by Transient Extreme Ultraviolet Spectroscopy

The content and figures in this chapter are reprinted or adapted with permission from S. K. Cushing, Michael Zürch, Peter M. Kraus, Lucas M. Carneiro, Angela Lee, Hung-Tzu Chang, Christopher J. Kaplan, and Stephen R. Leone, "Hot Phonon and Carrier Relaxation in Si(100) Determined by Transient Extreme Ultraviolet Spectroscopy." Structural Dynamics, ***2018****, 5.*

The thermalization of hot carriers and phonons gives direct insight into the scattering processes that mediate electrical and thermal transport. Obtaining the scattering rates for both hot carriers and phonons currently requires multiple measurements with incommensurate timescales. In this chapter, transient extreme-ultraviolet (XUV) spectroscopy on the silicon *2p* core level at 100 eV is used to measure hot carrier and phonon thermalization in Si(100) from tens of femtoseconds to 200 ps, following photoexcitation of the indirect transition to the Δ valley at 800 nm. The ground state XUV spectrum is first theoretically predicted using a combination of a single plasmon pole model and the Bethe-Salpeter equation with density functional theory. The excited state spectrum is predicted by incorporating the electronic effects of photo-induced state-filling, broadening, and band-gap renormalization into the ground state XUV spectrum. A time-dependent lattice deformation and expansion is also required to describe the excited state spectrum. The kinetics of these structural components match the kinetics of phonons excited from the electron-phonon and phonon-phonon scattering processes following photoexcitation. Separating the contributions of electronic and structural effects on the transient XUV spectra allows the carrier population, the population of phonons involved in inter- and intra-valley electron-phonon scattering, and the population of phonons involved in phonon-phonon scattering to be quantified as a function of delay time.

4.1 Introduction

The control of ultrafast carrier thermalization and transport processes is increasingly important in nanoscale semiconductor junctions,[1] next-generation thermoelectrics,[2] and hot carrier solar cells.[3] Through extensive optical and electrical characterization, the electron-phonon and phonon-phonon scattering processes have been detailed in Si, Ge, and GaAs for carriers in the lowest-lying conduction and valence valleys.[4–6] This information has proven vital for allowing accurate device prediction and modeling through the Boltzmann transport equations.[7] However, the time scale and energy range over which the individual scattering pathways can be tracked are limited by the narrow pump and probe pulse bandwidths required to select specific phonon or electron features. Additionally, the need for multiple types of instrumentation hinders rapid understanding of hot carrier transport and relaxation in nanostructured and two-dimensional materials.

Transient electron diffraction and x-ray diffraction measurements have made considerable progress towards understanding coupled carrier-phonon dynamics by directly measuring the lattice dynamics following photoexcitation.[8–14] The lattice deformations created by the initial carrier distribution and the lattice expansions caused by excitation of a non-thermal phonon bath during carrier thermalization have been measured and predicted in Si and other semiconductors at and above the melting threshold.[15–21] The electron-phonon scattering has been separated into three phonon modes using a non-thermal lattice model.[8] Coherent optical and acoustic phonon measurements, as well as acoustic shock wave measurements, have also allowed phonon creation and decay to be understood following electronic excitation.[22–28] The lattice dynamics are directly measured in each of these investigations, but the electronic contribution must often be inferred. A table-top technique that can directly measure both the carrier and phonon distributions following excitation remains to be established.

Generation of extreme ultraviolet light (XUV) by high harmonic generation (HHG) can be used to probe the electronic and structural dynamics through core-level transitions, similar to the previous measurements at synchrotron and free electron sources but using a table-top setup.[29–34] When a core electron is promoted to an unoccupied state, the core-hole potential modifies the valence potential, and a highly localized core-hole exciton is formed. The measured XUV absorption is therefore distorted from the ground-state unoccupied density of states and contains local structural information.[35–37] In atomic and molecular systems, core-hole effects can be theoretically predicted, allowing electronic and vibrational dynamics to be quantified following photoexcitation.[38,39] In a semiconductor, multi-electron and many-body effects complicate the interpretation and prediction of XUV absorption, making it difficult to separate electronic and structural contributions.[40–42] This has so far slowed the use of transient XUV spectroscopy as a single-instrument method for understanding the carrier and phonon thermalization pathways in semiconductors.

In this chapter, the underlying electronic and structural contributions to the Si $L_{2,3}$ edge evolution are separated following 800 nm optical excitation to the Δ valley. Ground and excited state calculations using a single plasmon pole model and the Bethe-Salpeter equation (BSE) with density functional theory (DFT) are used to interpret the measured changes in the Si $L_{2,3}$ edge

XUV absorption. Hot carrier thermalization dynamics are resolved through state-filling at the appropriate valleys' critical points. Lattice dynamics are recognized using the unique changes in the critical point structure that result from optical and acoustic phonon excitation. From the comprehensive measurements of XUV transient absorption versus time, a [100] lattice deformation is extracted with kinetics that mirror the high-energy phonons involved in intervalley electron-phonon scattering. Additionally, a thermal lattice expansion is obtained with kinetics that follow the creation of low-energy, mainly acoustic phonons by intra-valley electron-phonon scattering and phonon-phonon decay processes. These findings suggest that ultrafast pump-probe transient XUV spectroscopy can provide the important carrier and phonon scattering timescales and pathways following photoexcitation in a single set of measurements.

4.2 Methods

4.2.1 Experimental

The static and transient XUV absorption spectra of 200 nm thick, p-type (B-doped, 10^{15}/cm^3) Si (100) membranes purchased from Norcada are measured with high-harmonic generation (HHG) XUV radiation. The HHG is produced in helium gas (semi-infinite gas cell) with a 50 fs pulse duration, 1 kHz repetition rate regeneratively amplified Ti-sapphire laser.[32] A 400 nm frequency doubled output produced in a BBO crystal is added to the 800 nm fundamental to produce both even and odd harmonics in the HHG process. The excess 800 and 400 nm light is removed from the HHG spectrum using a combination of a micro-channel plate (MCP) and Zr filters, resulting in XUV harmonics spanning from 70 to 120 eV.[43] The excitation wavelength is chosen to match the indirect optical transitions to the Δ (800 nm, 1.55 eV) valley.[44] The polarizations of the pump and probe are parallel to the [110] direction of the (100) membrane. Delay times between optical pump and XUV probe are obtained by varying the distance of a retroreflector with a computer-controlled delay stage.

Pump powers are adjusted to produce a carrier density of 1.5 10^{20}/cm^3. The average carrier density (ΔN) is estimated using[13]

$$\Delta N = \frac{F}{\hbar\omega}\frac{1-R}{L}(1-e^{-\alpha L})(1+Re^{-\alpha L}), \tag{4.9}$$

where F is the laser fluence, R is the reflectivity of the thin film, hx is the energy of the photons, L is the membrane thickness, and a is the absorption coefficient for Si.[45] The second exponential term accounts for back-reflections at the rear membrane-vacuum interface. The absorption was estimated as 2.5 ± 0.5 ×10^3 cm^{-1} using the measured transmission of the sample at 800 nm, and then accounting for reflectivity losses using the Fresnel equations for thin films and the known refractive index of silicon. To prevent the possible propagation of error from this estimated absorption, the excited carrier density is fit during the analysis. For 800 nm excitation, the absorption depth is larger than the 200 nm membrane thickness, so the depth-dependent effects from the photoexcited carrier distribution are negligible.

The effects of two-photon absorption (TPA) are considered for the high fluence used, especially for 800 nm excitation across the indirect band gap.[46,47] The spatially- and intensity-dependent absorption can be solved for using

$$\frac{dI}{dz} = -\alpha I - \beta I^2, \tag{4.10}$$

where I is the peak intensity of the sech^2 experimental pulse, α is the same as in Eq. (1), and β is taken as 2×10^{-9} cm/W.[48,49] Given that one electron-hole pair is created for every two photons in two-photon absorption, Eq. (4.2) predicts that at 800 nm excitation the two photon absorption contribution is less than 10% of the photoexcited carriers at the intensities used in the experiments. The lack of a two-photon absorption contribution is also experimentally confirmed by the absence of a measurable state-filling signal within the 5 mOD noise level at the L_1 critical point of the XUV spectrum for 800 nm pulsed excitation. Two photon absorption effects are therefore excluded in the experimental analysis, recognizing that the < 10% modulation would be below the 5 mOD noise level of the < 40 mOD overall changes measured in the experiment.

4.2.2 Theoretical

Calculation of the ground state XUV absorption is done within the OCEAN code (Obtaining Core-level Excitations using *Ab initio* methods and the NIST BSE solver).[50,51] The density functional level is used to calculate the ground state electron densities and wave-functions using Quantum-ESPRESSO.[52] In the OCEAN code, projector augmented wave (PAW) reconstructed wave functions are used to estimate the core-level transition matrix elements. The dielectric screening is estimated using a real-space random phase approximation inside a sphere around the atom along with a Levine-Louie model dielectric function outside the sphere.[53,54] The final electron-hole states are then calculated by the Bethe-Salpeter (BSE) equation.

The specific parameters for the DFT and BSE-DFT calculations are as follows. The DFT density of states is calculated within the local density approximation (LDA) using a norm-conserving generalized gradient approximation (GGA) Perdew-Burke-Ernzerhof pseudopotential with a converged *k*-point mesh of 20 × 20 × 20 points and a plane wave cutoff of 100 Ry. The converged lattice constant was 5.46 Å. The BSE-DFT calculations in OCEAN are then performed using the Quantum ESPRESSO results. The final and projector augmented wave states are found converged to an accuracy that reproduces the experimental absorption at k-point meshes of 8 × 8 × 8 and 2 × 2 × 2, respectively. The total number of bands for the final and projector augmented wave states are well converged at 100 and 200, respectively. The SCF mixing is taken as 0.7 with 250 iterations used. The BSE mesh is taken as 6 × 6 × 6 and a cut-off radius of 8.0 Bohr is used. A radius of 8.0 Bohr is also used for the projector augmented wave shell with a 0.8 scaling factor of the slater G parameter. A dielectric constant of 11.7 is used for silicon. The absorption is calculated for XUV dipole orientations along the [100] and [110] directions. Within the experimental broadening, little difference in the predicted spectrum is found between these dipole orientations.

The varying lattice expansions for the non-linear fit are linearly interpolated from a series of lattice expansions in the BSE-DFT calculations to make the fitting procedure computationally feasible. Lattice expansion values of –5% to 5% are computed to allow an accurate interpolation of intermediate values and to not restrict the non-linear fit parameter search space. The unit cell is relaxed for each expansion value. The BSE-DFT calculations do not properly describe valence core-hole effects at energies below the Fermi level or interference from photoelectron scattering pathways that begin at 5–10 eV above the Fermi level. The best fit is therefore determined in the energy range of 98–105 eV. The loss in accuracy outside this energy range is reflected in the discrepancies between the experimental and predicted ground state absorption shown in Fig. 4-1(b). The inaccurate description of the valence region, the weak Si 2*p* transition strength to the mostly *p*-character valence band, and the excited-state broadening prevent the hole signatures from being extracted with reasonable certainty.

4.3 Results and Discussion

4.3.1 Ground State Absorption

An accurate mapping of the silicon band structure onto the ground state XUV absorption is critical for interpreting the experimental spectra. Not only does the photoexcited core-hole modify the energy and amplitude of the band structure's critical points but also the energy-dependent core-hole lifetime smooths the critical point structure at energies higher than the transition edge. By first modeling the effects of the Si 2*p* core-hole on the ground state spectrum, the measured excited state spectrum can be more accurately interpreted in terms of the photoexcited carrier and phonon distributions. The amplitudes and energies of the L_1 and Δ_1 critical points are otherwise incorrectly assigned in the ground state XUV absorption; a discrepancy which would prevent an accurate interpretation of the excited state XUV spectrum.

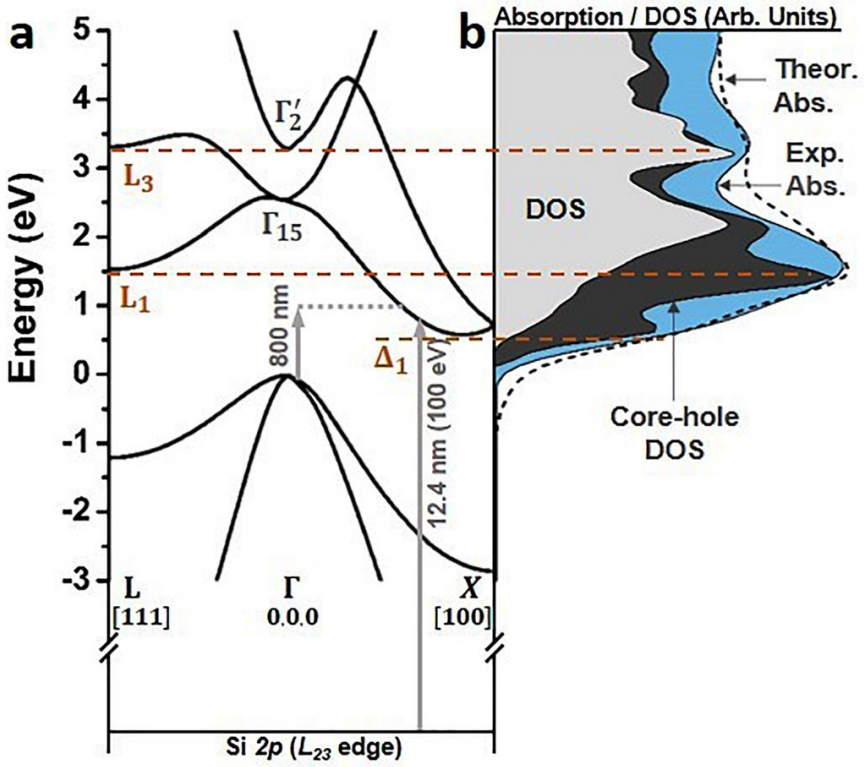

Figure 4-1: Critical points and core-hole modification of the spectrum of the Si 2p $L_{2,3}$ edge. (a) Band structure of silicon along the L-Γ-X path, highlighting the Δ_1, L_1, and L_3 critical points. The k-space directions are marked. Note L is at $\frac{1}{2}, \frac{1}{2}, \frac{1}{2}$ and Δ is at ~0.8,0,0 in the Brillouin zone. The excitation wavelength and an example core level transition are marked as arrows. The arrow length is adjusted for the underestimation of the band gap in the DFT calculation. (b) Comparison of the *s* + *d* projected density of states (DOS, grey), core-hole modified DOS (dark grey), experimental absorption (blue), and theoretical absorption (dashed) predicted by the core-hole modified DOS broadened with a single plasmon pole model. The 2*p* core-hole exciton renormalizes the L_1 and Δ_1 *s*-*p* hybridized critical points, while having less effect on the higher lying, *d*-character L_3 critical point.

To facilitate comparison between the measured ground state XUV spectrum and the band structure of silicon, the measured XUV absorption spectrum is deconvoluted for spin-orbit splitting in Fig. 4-1 using two delta functions spaced by 0.6 eV.[36] The DFT predicted critical points of the band structure along the L-Γ-X path and the *s* + *d* projected density of states (DOS) relevant to the Si 2*p* $L_{2,3}$ transition are compared to the measured XUV absorption in Figs. 4-1(a) and 4-1(b). The oscillator strength for the *s* character states is assumed to be twice that of the *d* character states.[36] Figure 4-1(b) shows that the experimental ground state XUV absorption does not directly map onto the ground-state DOS calculated by DFT. In particular, the amplitude of the absorption near the L_1 and Δ_1 critical points is underestimated. This discrepancy occurs because the 2*p* core-hole excited by the XUV transition alters the valence potential, creating a core-hole exciton and modifying the DOS, especially for the *s*-*p* hybridized L_1 and Δ_1 critical points.[36,37]

The effects of the core-hole on the final DOS in the XUV transition can be calculated using the Bethe-Salpeter equation [dark grey area in Fig. 4-1(b)].[50,51] The BSE-DFT calculation

accurately predicts that the Si 2*p* core-hole distorts the projected *s* + *d* DOS, especially at the Δ_1 and L_1 points. The BSE-DFT calculation also uses projector augmented wave (PAW) dipole transition elements instead of the estimated *s* + *d* contribution of the DFT only calculation. Following the BSE-DFT calculation, the theoretical XUV absorption is calculated by broadening the core-hole modified DOS [dashed line in Fig. 1(b)]. The XUV broadening is treated as an energy-independent core-hole lifetime plus an energy-dependent lifetime that depends on the excited core-level electron's inelastic scattering.[50,51,55–57] The inelastic electron scattering can be modeled using an empirical model, such as the Seah-Dench formalism, or by using the imaginary part of the self-energy to calculate the electron's inelastic mean free path.[58–61] Here, the latter approach is taken to allow the effects of visible light photoexcitation on the core-level transition to be included when modeling the transient absorption data sets.

Specifically, the energy-dependent broadening is approximated using a Drude-Lindhard single-plasmon pole model, which can accurately represent the experimental Si electron energy loss function.[62,63] A Gaussian instrumental broadening of 0.2 eV and an energy-independent core-hole lifetime represented by an energy width of 15 meV are also included.[64] Silicon's valence electron density sets the plasmon pole in the electron energy loss function at ~16.8 eV above the Fermi level. The single plasmon pole model of the electron energy loss function is parameterized as[59]

$$Im\left[-\frac{1}{\epsilon(\Delta E,k)}\right]=\frac{A_1\gamma_1\Delta E}{\left(\left(\hbar\omega_{0,k}\right)^2-\Delta E^2\right)^2+\gamma_1^2\Delta E^2}*\Theta(\Delta E-Eg), \tag{4.11}$$

with

$$\hbar\omega_{0,k}=\hbar\omega_0+C*\frac{\hbar^2k^2}{2m}, \tag{4.12}$$

where ΔE is the energy difference between the Fermi level and the core-level excited electron, k is the momentum of the electron, Eg is the band gap, A_1 is the oscillator strength equal to 256.4 eV^2 , γ_1 is the damping coefficient equal to 3.8 eV, $\hbar\omega_0$ is the energy of the plasmon pole equal to 16.8 eV, m is the electron mass, and C, here taken as 0.5, is a factor used to approximate the parabolicity of the conduction bands. The core-level transition lifetime is then calculated in terms of the inelastic mean free path, λ, of the electron as[59]

$$\lambda^{-1}(E)=\frac{1}{\pi E}\int dE'\int dk\,\frac{1}{2mk}Im\left[-\frac{1}{\epsilon(E',k)}\right], \tag{4.5}$$

where the energy integral goes from 0 to $E-E_f$ and the momentum integral goes from $k_\pm=\sqrt{\frac{2mE}{\hbar^2}}\pm\sqrt{\frac{2mE}{\hbar^2}(E-E')}$. These bounds limit the scattering space possible for the core-level excited electron. The inelastic mean free path is converted into an energy dependent lifetime $\Gamma(E)$ using

$$\Gamma(E) = \frac{\hbar}{\lambda(E)}\sqrt{\frac{2E}{m}} + \Gamma_{CH} \tag{4.6}$$

where Γ_{CH} is the 15 meV core-hole lifetime.[64] The XUV absorption is then calculated by convolution of a Lorentzian with energy-dependent width given by Eq. (4.6) and the core-hole modified DOS calculated in Fig. 4-1(b).

Equation (4.5) represents the increasing loss channels of the photoexcited core-level electron with the increase in the energy. The absorption spectrum becomes broader with increasing energy because more loss channels are possible. The single plasmon pole model is an approximation, however, which neglects the more complicated valence loss channels near the conduction band edge. Further, the Drude-Lindhard approximation is only valid at small energy and momentum ranges above the Fermi level. These approximations lead to an over-estimation of the broadening a few eV above the Fermi level, which creates an under-estimation in depth for the above-edge minima in Fig. 4-1(b). The single plasmon pole model is used because it allows the change in the energy-dependent broadening to be estimated following visible light photoexcitation from the photoexcited carrier density. If a non-energy-dependent broadening is used, the fine features near the XUV edge and broad features above the XUV edge can neither be predicted in the ground state spectrum nor can the excited state broadening change be predicted from the photoexcited carrier density. The calculated absorption in Fig. 4-1(b) accurately predicts the measured static Si $L_{2,3}$ absorption within these approximations.

4.3.2 Electronic Contributions to the Excited State Absorption

An experimental differential absorption spectrum of the Si $L_{2,3}$ edge absorption versus time following photoexcitation with 800 nm light is shown in Fig. 4-2(a). The differential absorption is reported as the logarithm of the pump-on divided by the pump-off spectrum, and the major features of the spectrum align with the critical points of the ground state XUV absorption [Fig. 4-2(b)]. Similar to modeling the ground state absorption, the core-hole effects and energy-dependent broadening must be considered when interpreting the measured excited state spectrum. In the excited state spectrum, the change in carrier density following visible light photoexcitation results in both electronic and structural changes to the silicon [Fig. 4-2(c)]. The electronic effects can be categorized as state-blocking, broadening, and renormalization, all of which can be considered instantaneous within the 50 fs 800 nm pulse width. The structural changes can be categorized as lattice deformations and expansions resulting from carrier-phonon and phonon-phonon scattering. The different electronic and structural contributions are summarized in Fig. 4-2(c) for the 100 fs time slice and detailed in this subsection.

As noted, the electronic contributions can be summarized as photoinduced state-filling, broadening, and renormalization. First, the promotion of carriers from the valence to conduction band leads to changes in occupation of the band structure of silicon, modulating the absorption spectrum.[4,65] Here, this effect is referred to as state-filling, which describes the allowing or blocking of XUV transitions from the Si 2*p* core level to the valence or conduction band,

respectively, following the promotion of electrons by the 800 nm pump pulse [Fig. 4-2(c)]. For the Si $L_{2,3}$ edge, the transition edge lies at approximately 100 eV.[66] Specifically, the L_2 onset energy is taken as 99.8 eV following the spin-orbit deconvolution. Immediately following the excitation pulse, holes created in the valence band are expected to increase the XUV transition rate at energies lower than 98.7 eV or the edge onset energy minus the band gap energy.

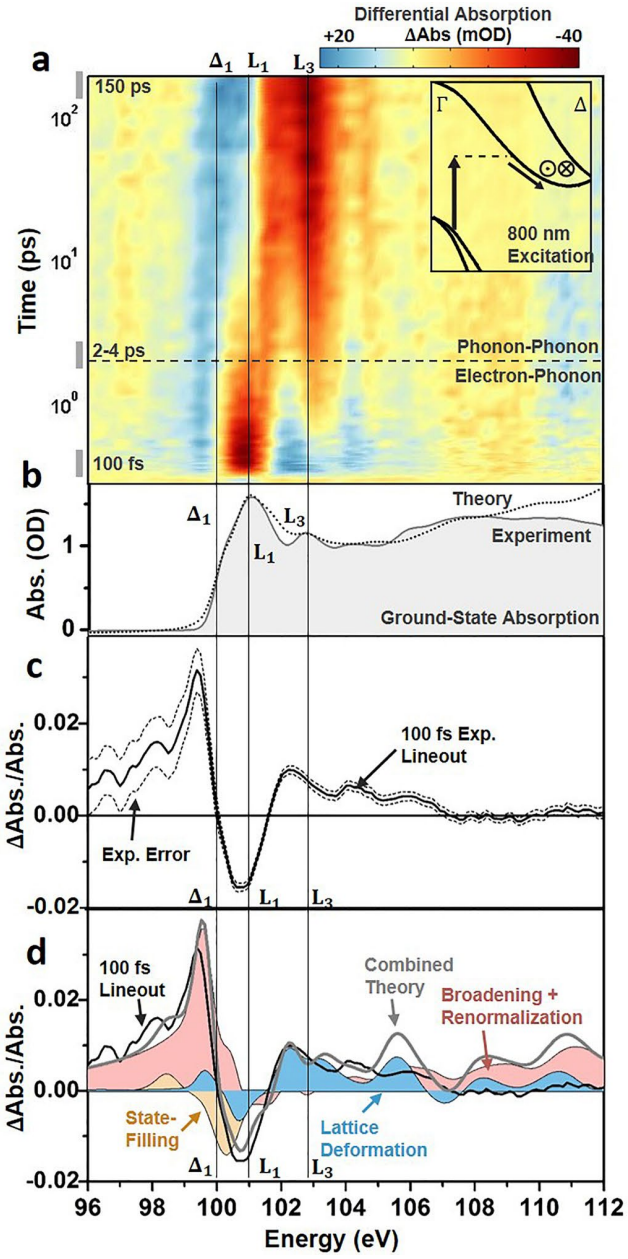

Figure 4-2: Differential absorption data following 800 nm excitation of the Si $L_{2,3}$ XUV edge. (a) The differential absorption data are shown as a color map on a logarithmic time scale up to 200 ps time delay following 800 nm excitation to the Δ_1 valley. The inset shows the excitation and scattering pathways for the excited electrons. The in and out of plane arrows indicate where inter-valley scattering between degenerate valleys is possible. The cross-over time between predominantly electron-phonon scattering or phonon-phonon scattering is also indicated by the dashed horizontal line. (b) The static ground state

experimental and theoretical absorption from Fig. 1(b) are shown for comparison to the differential absorption. (c) The experimental 100 fs differential absorption (black solid line). The dashed lines indicate the 95% confidence intervals of the measurement. (d) The theoretically predicted state-filling (light orange), broadening and renormalization (light pink), and lattice deformation (light blue) contributions for a $1.5 \times 10^{20}/cm^3$ photoexcited carrier density. The grey solid line indicates the combined theoretical contributions of the shaded areas.

Similarly, the optical promotion of electrons to the critical points in the conduction band is expected to decrease the absorption above 100 eV. Specifically, for the 800 nm excitation into the Δ_1 point, a decrease in absorption is expected at 100.25 eV, which is the valence band maximum at 98.7 eV plus the 1.55 eV pump energy.

The possible state-filling contributions are modeled to first order by first blocking (allowing) transitions in the core-hole modified DOS before broadening. The 0.2 eV experimental resolution is close to the 0.3 eV width of the excitation spectrum of the 800 nm pump, obscuring fine detail in the state-blocking spectrum. This allows a Gaussian distribution of carriers with 0.3 eV width to be used for both the initial non-thermal and final thermalized carrier distribution. The percentage of state-filling is normalized by the calculated DOS to account for Pauli-blocking near the CB and VB edge.[67] The XUV blocking percentage will depend on the orbital character of the band. Since the XUV transition occurs from the *p*-character core level, unequal differential absorption magnitudes exist for electrons in the mixed *s*-*p* character conduction band and holes in the mainly *p*-character valence band. The calculated state-filling percentage is also adjusted for the character of the probed DOS in the dipole-allowed XUV transitions.

Using the ground-state absorption model of Fig. 4-1 and a carrier density of 1.5×10^{20} carriers/cm^3, the photoexcited carriers are predicted to create an increased absorption below 100 eV [light blue region in Fig. 4-3(a)] and a decreased absorption above the Δ_1 critical point that is centered around 101 eV [light pink region in Fig. 4-3(a)]. The decreased absorption predicted in Fig. 4-3(a) does not energetically align with the experimentally measured decrease in absorption [black solid line in Fig. 4-3(a)]. This is because the excited state broadening, renormalization, and structural effects discussed in the following paragraphs partially cancel the change in absorption from the state-filling contribution [Fig. 4-3(b)]. It should be noted that the first 50 fs electron-electron scattering can energetically broaden but not relax the excited carrier distribution. The impact of this energetic redistribution on state-filling is not discernable within the 50 fs pulse-width and excited state and instrumental broadening.

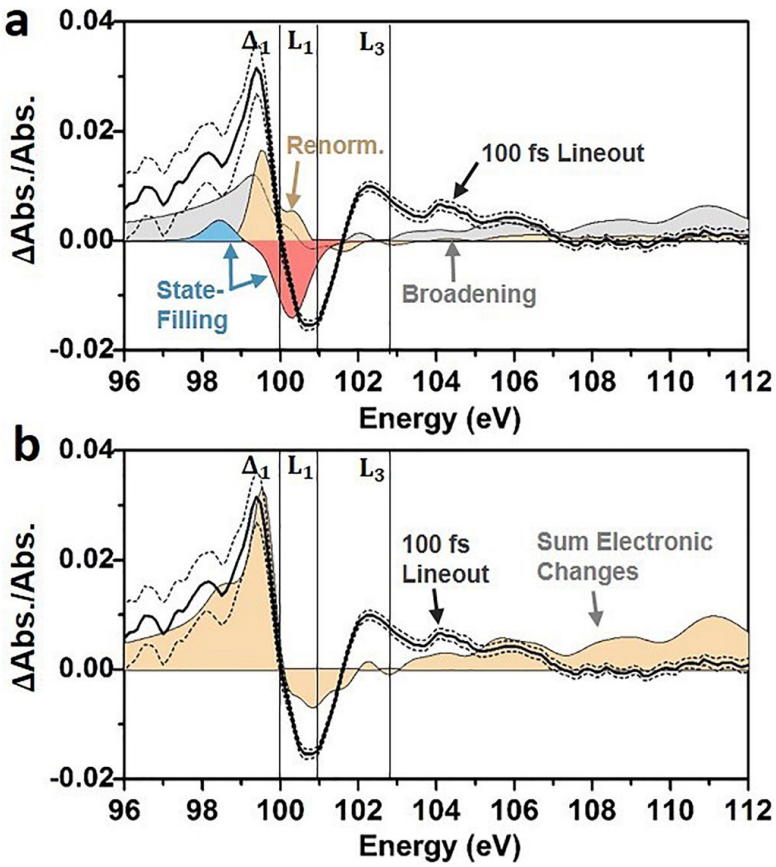

Figure 4-3: Electronic contributions to the excited state XUV absorption. (a) The theoretically predicted state-filling of holes (light blue) and electrons (light pink), broadening (grey), and renormalization (light orange) contributions for a $1.5 \times 10^{20}/\text{cm}^3$ photoexcited carrier density. The theoretical predictions are compared to the experimental 100 fs differential absorption (black solid line). The dashed lines indicate the 95% confidence intervals of the measurement. (b) The orange shaded area indicates the sum of the electronic contributions predicted in panel (a). The broadening, renormalization, and state-filling combine to accurately predict the increased absorption at energies below the Δ_1 point. The decreased absorption at the L_1 point is predicted at the correct energy, but the amplitude of the L_1 and the L_3 features are underestimated when only the electronic contributions are considered.

In addition to state-filling effects, the reduction in valence electron density and the increase in the conduction electron density will also change the excited state XUV broadening. The change in the ground state XUV broadening with photoexcitation is modeled to first order by changing the carrier density in Eq. (4-3). Specifically, the experimentally excited carrier density of 1.5×10^{20} carriers/cm^3 decreases the plasmon pole frequency by 0.16 eV through

$$\omega_0 = \sqrt{\frac{(n - \Delta N)q^2}{m\epsilon_0}}, \tag{4.7}$$

where n is the ground state valence carrier density, m is the mass of an electron, ϵ_0 is the permittivity of free space, q is the charge of an electron, and ΔN is the excited carrier density. Decreasing the valence plasmon by the photoexcited carrier density from 16.8 eV to 16.64 eV

increases the energy-dependent broadening following integration in Eq. (4.5). In the differential absorption spectrum, the increase in broadening [grey area in Fig. 4-3(a)] leads to an increase in absorption at energies above and below the L_1 critical point. As noted in 4.3.1, treating the broadening by this approach ignores the 800 nm photoexcited conduction band plasmon as well as modification of other valence loss channels.

Finally, changing the valence and conduction electron densities will change the screening of the electrons, creating a photoexcited renormalization of the band gap.[68–71] The magnitude of the band gap renormalization is over-estimated using only a plasmon-pole model,[72] so here the predicted cube root functional dependence of the carrier density is scaled to the experimentally reported values[73]

$$\Delta E_{CB}(\Delta N) = -D * \left(\frac{\Delta N}{N_0}\right)^{\frac{1}{3}}, \tag{4.8}$$

which gives a downward shift of the conduction bands (ΔE_{CB}) of ~60 meV at 1.5×10^{20}/cm^3. The valence band shifts by a similar amount, but valence band effects are not clearly observed in the experimental spectra. In Eq. (4.8), ΔN is the excess carrier density, while Δ and N_0 are fit parameters with values of 0.05 eV and 1×10^{20} cm^{-3}, respectively, for the carrier density range used in these experiments.

To completely describe the renormalization of the XUV absorption edge, the change in screening of the core-hole exciton must also be estimated to first order following Ref. 74 by

$$\Delta E_{core-hole}(\Delta N) = \frac{3q^2}{(4\pi)^2 \epsilon \epsilon_0} (3\pi^2 \Delta N)^{\frac{1}{3}}, \tag{4.9}$$

where ΔN is the excess carrier density, ϵ is the dielectric constant, ϵ_0 is the vacuum permittivity, and q is the charge of an electron. The renormalization of the band gap and core level transition are then approximated by uniformly shifting the core-hole adjusted DOS in the ground-state model by

$$\Delta \mathrm{E}(\Delta N) = \Delta E_{core-hole}(\Delta N) + \Delta E_{CB}(\Delta N), \tag{4.10}$$

The decrease in binding energy of the core-hole exciton [Eq. (4.9)] counteracts the band gap renormalization [Eq. (4.8)] to large extent, leading to a smaller overall renormalization of the XUV transition of <10 meV instead of 60 meV. The smaller renormalization of the Si $L_{2,3}$ edge compared to the band gap has been experimentally confirmed by doping studies.[75] The uniform shift of the conduction band structure is an approximation based on Ref. 76 where a many-body perturbative GW calculation was used to predict the excited state XUV spectrum to similar overall effect. In both cases, the renormalization primarily leads to an increase in absorption around the Δ_1 point [orange area in Fig. 4-3(a)].

It should be emphasized that Eqs. (4.7)–(4.10) are based on first order approximations of the many-body response to the photoexcited electron density as verified by visible light pump-probe

experiments, ignoring the possibility of a core-hole perturbation to the many body response. The x-ray probe excitation density is one million times less than the visible light pump, making this a plausible assumption. The validity of this assumption can be evaluated by comparison to other x-ray absorption measurements. In particular, identical to visible light experiments, attosecond x-ray absorption experiments confirm that the electronic response is complete within <20 fs.[76] During this time, the change in the differential absorption can be completely explained by electronic contributions. The structural response from photoexcited electrons was measured to only be significant on >30 fs timescales, at which time the spectral features match those in Fig. 4-2(a). The spectral features of this short time scale strain are further confirmed by comparison to steady-state x-ray absorption measurements of strained silicon membranes.[77] Similarly, the spectral features of the long time scale isotropic lattice expansion is confirmed by comparison to heated silicon.[78] While these experiments seem to confirm the use of these first order approximations, it still must be emphasized that these calculations are approximations, and the full many-body response of the valence to the photoexcited electrons and core hole needs to be further explored.

Overall, in the predicted XUV differential absorption, the electronic contributions sum to create a below-edge increase and an above-edge decrease in the XUV absorption [Fig. 4-3(b)]. The electronic components also contribute to the broad increase in absorption at energies greater than 103 eV. The combined renormalization and broadening contributions span the entire measured energy range, whereas state-filling contributions occur mainly near the transition edge. At the transition edge, the electronic contributions have similar amplitude but different signs, leading to cancellation. The cancellation between the different electronic contributions in Fig. 4-3 emphasizes the importance of modeling how the ground state band structure relates to the XUV absorption. Otherwise, the region of decreased absorption below 100 eV and increased absorption between 100 and 102 eV could incorrectly be assigned as state-filling from electrons and holes. The remaining discrepancy between the measured and predicted differential absorptions at energies above 100 eV suggests the presence of structural contributions, as discussed in the next subsection.

4.3.3 Structural Contributions to the Excited State Absorption

The first-order approximations of the electronic contributions following visible light photoexcitation only partially predict the measured changes in the ground state absorption [Fig. 4-3(b)]. The differential absorption above 100 eV is not replicated in the modeled spectrum. The above edge spectral features primarily relate to the local structural environment.[35,37] The incomplete modeling of higher energy features suggests that the dynamics of the local structural environment may also need to be considered. Excited state structural changes are possible by the anharmonicity of excited optical and acoustic phonon modes, as well as the screening of bonds by the photoexcited carrier density, creating lattice deformations and expansions. Depending on the axis of the lattice deformation or expansion, distinct changes will occur to the critical points of the Si $L_{2,3}$ edge as shown in Fig. 4-4.[77,79–81]

For example, a [100] lattice deformation redshifts the Δ, Γ, and L valleys with a magnitude dependent on their location in the Brillouin zone relative to the direction of the applied strain [Fig.

4-4(a)]. The [100] lattice deformation also splits the six degenerate Δ_1 valleys by approximately 150 meV for each 1% of expansion.[77,79–81] Together, these two effects result in a decreased (increased) absorption at energies below (above) the L_1 critical point in Fig. 4-4(a). Unlike the [100] lattice deformation, an isotropic expansion does not break degeneracy or introduce different relative shifts to the critical points in the XUV spectrum [Fig. 4-4(b)]. This results in a more uniform spectral redshift of the Si $L_{2,3}$ edge, leading to an increased (decreased) absorption at energies below (above) the L_1 critical point in Fig. 4-4(a).[78]

The electronic effects of subsection 4.3.2 are combined with a range of [100] lattice deformations and isotropic lattice expansions in Figs. 4-4(c) and 4-4(d), respectively. An isotropic lattice expansion is distinct from the differential absorption features of an anisotropic lattice deformation, as can be visualized by comparing the colored lines to the grey dashed line in Fig. 4-4(c).

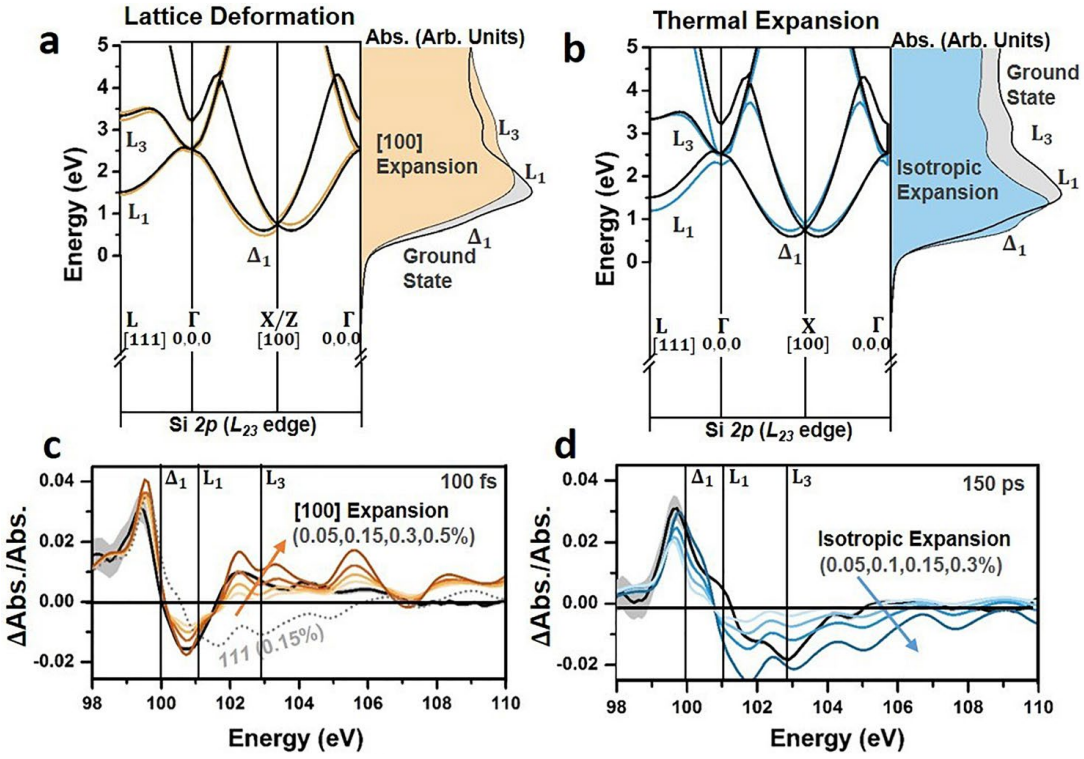

Figure 4-4: Structural contributions to the excited state XUV absorption. (a) The predicted effect of an expansion along the [100] direction (light orange) and (b) an isotropic lattice expansion (light blue) on the Si band structure, shown as the resulting change in the theoretically predicted absorption. In each case, a 3% expansion of the relevant axis is used. The k-space directions are marked. Note L is at $\frac{1}{2}, \frac{1}{2}, \frac{1}{2}$ and Δ is at ~0.8,0,0 in the Brillouin zone. The ground state silicon band structure (black line) and ground state absorption (grey area) are shown for reference to the [100] and isotropic expansion calculations (colored lines and colored areas). The top of the valence band is arbitrarily set to zero. Comparison of the experimental (solid black line) and theoretical (color-range or dashed line) differential absorption lineouts at (c) 100 fs and (d) 150 ps after 800 nm excitation. The theoretical differential absorption is calculated using a range of [100] expansions for the 100 fs time slice and a range of isotropic expansions for the 150

ps time slice. In each case, the carrier densities from Table 4-1 are used. An isotropic expansion is also shown for comparison for the 100 fs time slice as a grey dotted line. The grey shaded areas show the 95% confidence intervals on the experimental data.

The combined electronic and structural contributions seem to improve agreement between the modeled and measured differential absorption at both 100 fs and 150 ps. However, the time-dependent magnitude of the possible structural contributions will depend on the evolution of the initially excited carrier distribution. This means that, unlike the electronic effects discussed in subsection 4.3.2 which were complete within the pulse width, the magnitude of the structural effects cannot be easily estimated from the initial experimental excitation alone. A best-fit procedure is instead applied to determine the presence of any structural contributions at three different time scales following photoexcitation (Fig. 4-5). This approach assumes that an equilibrium lattice deformation can approximate any non-equilibrium effects. The excited carrier density, lattice deformation, and lattice expansion are assessed by a non-linear fit using a robust algorithm weighted by the experimental uncertainty. Other combinations of biaxial or triaxial strains could not fit the experimental differential absorption. The fit results are summarized in Table 4-1.

(a) 100 femtoseconds. In the first several hundred femtoseconds following 800 nm excitation, the electrons redistribute between the degenerate Δ valleys by inter-valley scattering with optical phonon modes.[82–85] As shown in the bottom panel of Fig. 4-5(b), a 100 fs differential absorption time slice is best fit by a [100] expansion of 0.3 ± 0.05%, no isotropic expansion at 0.0 ± 0.01%, and a carrier density of 1.5 ± 0.1 × 10^{20} carriers/cm^3. When combined with the electronic contributions, the [100] deformation accurately replicates the increased absorption at energies below the Δ_1 critical point, the decreased absorption at the L_1 critical point, and the increase in absorption above 102 eV. Discrepancies between the theoretical and experimental differential absorption are greatest at the critical points that are not accurately described in the ground state spectrum.

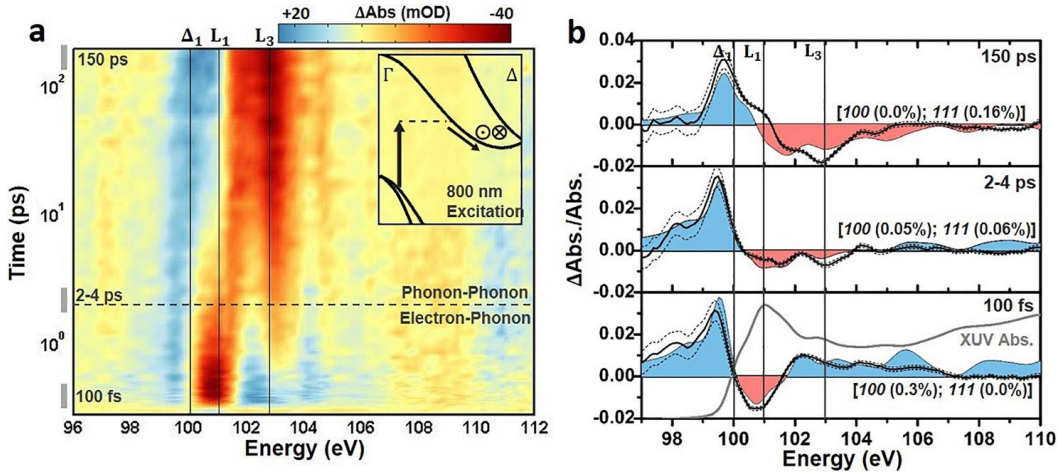

Figure 4-5: (a) Differential absorption of the Si $L_{2,3}$ edge and comparison to theory. The differential absorption is shown on a logarithmic time scale from 0 to 200 ps for 800 nm excitation to the Δ_1 valley. The inset represents some of the possible excitation and scattering pathways for the excited electrons. The

in and out of plane arrows indicate where inter-valley scattering between degenerate valleys is possible. The cross-over time between predominantly electron-phonon scattering or phonon-phonon scattering is also indicated by the dashed horizontal line. A time slice [times indicated by gray bars to the left of panel (a)] from these periods is shown in (b). (b) The theoretical predictions from the single plasmon pole and BSE-DFT calculation are shown as the red and blue colored shading. The color shading matches the increased and decreased absorption in (a). The best fit percentage expansion of the relevant lattice vectors is indicated. The best fit range covers 98–105 eV, above and below which the BSE-DFT calculation loses accuracy. In (b), the ΔAbs./Abs. scale is used to allow direct comparison of experiment (solid line) to theory (shaded area) without scaling of the results. The dashed lines indicate the 95% confidence intervals of the measurement. The log scale of time in (a) is offset by 100 fs for visualization. The lineouts in (b) are averaged over the four nearest time-points.

For 800 nm excitation polarized along the [110] axis, dipole selection rules for the indirect transition lead to the four parallel and two perpendicular Δ valleys being non-equally populated.[86–89] A similar imbalance exists for the hole populations left by photoexcitation along the Γ-X line.[90,91] The anisotropic electron and hole population can lead to an anisotropic screening of the valence potentials, deforming the lattice.[92,93] This has also been described as an anisotropic phonon bath deforming the lattice to distribute carriers between the degenerate but unequally occupied valleys.[94–96] The presence of the [100] lattice deformation could possibly correlate with the anharmonicity of the [100]-like optical phonon modes excited during *g*- and *f*-type inter-valley scattering.

		~100 fs	~2-4 ps	~150 ps
800 nm (Δ)	Carrier density ($\times 10^{20}$/cm^3)	1.5±0.1	1.5±0.1	0.6±0.1
	100 Expansion (%)	0.3±0.05	0.05±0.03	0.00±0.08
	111 Expansion (%)	0.0±0.01	0.06±0.01	0.16±0.02

Table 4-1: Non-linear fit carrier densities and lattice expansions. Fit quantities are for an average of four times around the time indicated. 100 expansion denotes an expansion along the [100] direction, while a [111] expansion denotes an isotropic expansion along each axis.

In the previous electron and x-ray diffraction measurements, the magnitude of the lattice deformation caused by the photoexcited carrier density has been approximated by an equilibrium stress $\left(\sigma_{DP,k}\right)$ using[24,92]

$$\sigma_{DP,k} = -\sum\nolimits_k \Delta N_k E_k \gamma_k = \sum\nolimits_k \Delta N_k \frac{dE_k}{d\eta}, \tag{4.11}$$

where ΔN_k is the number of excess carriers in a valley with momentum *k*, E_k is the energy of the band or electron at *k*, $\gamma_k = -\frac{1}{E_k}\frac{dE_k}{d\eta}$ is the Grüneisen coefficient, and $\frac{dE_k}{d\eta}$ is the electronic deformation potential for a valley with momentum k and g is the strain. For the thin silicon

membranes used here, the strain in a particular k direction after photoexcitation is approximated by

$$\eta_k = \frac{h_{100}}{B}\sigma_{DP,k}, \tag{4.12}$$

where $h_{100} = 1 + \frac{2C_{12}}{C_{11}} = 1.77$ is a correction for the one-dimensionality of the strain[97] and B is the bulk modulus of 97.6 GPa.[98] In Eqs. (4.11) and (4.12), a positive stress is taken as leading to a positive lattice expansion. From Ref. 99, the deformation potential for a [100] strain is $h_{100} = \frac{dE_k}{d\eta} = 4.5$ eV. A carrier density of 1–2 × 10^{20} cm^{-3} will therefore result in a lattice deformation of 0.1–0.3% expansion. According to the dipole selection rules for the indirect transition, the photoexcited carrier density is anisotropic along the [100] directions, and this would be the expected direction of the lattice deformation.[86,87] The predicted expansion range is intended to reflect the experimental uncertainty in the carrier density as well as the use of bulk quantities to represent the thin film membrane. While the estimated lattice deformation replicates the magnitude from the best fit of the data, Eq. (4.12) is an equilibrium estimate to a very nonequilibrium effect. This approximation, coupled with the first order approximation of the electronic effects, means the exact origin of the lattice deformation in the experimental spectrum still warrants further exploration.

(b) 2–4 picoseconds. An intermediate lineout at 2–4 ps is examined in the second to top panel of Fig. 4-5(b). At this intermediate time-scale, an isotropic lattice expansion could exist from the acoustic phonon modes excited by intra-valley carrier thermalization and the initial decay of phonons previously excited by inter-valley scattering. The carrier density is not yet reduced by Auger recombination, which occurs on a >10 ps time scale, however the carrier distribution should be equally distributed between degenerate valleys by electron-phonon scattering. Accordingly, the 2–4 ps lineout is found to be accurately predicted by the same carrier density as at 100 fs, 1.5 ± 0.1 × 10^{20}/cm^3, but by decreasing the lattice deformation to be 0.05 ± 0.03% along the [100] direction [notation 100 in Fig. 4-5(b)] and by adding a 0.06 ± 0.01% isotropic expansion of all axes [notation of 111 in Fig. 4-5(b) implies an equal isotropic expansion of 0.06% along each axis]. It should be noted that the absorption depth is large, ~10 μm for 800 nm excitation. This means that the carrier distribution is uniformly excited throughout the 200 nm membrane, and the subsequent stress and strain will also be uniform. The isotropic expansion dynamics therefore follow the frequency and anharmonicity of the excited phonons, as in a coherent phonon or non-thermal melting experiment. However, the fitting to both a volume expansion and deformation on this time scale, which is faster than the acoustic velocity, suggests a combined distortion without volume expansion.[100]

(c) 150 picoseconds. After the hot carrier and hot phonon baths are fully thermalized, a thermal isotropic lattice expansion should be the primary structural contribution to the differential absorption. The isotropic expansion results from the anharmonicity of acoustic phonon modes excited through intra-valley and phonon-phonon scattering, which is equivalent to heating the lattice.[82] Accordingly, the differential absorption at 150 ps [top panel in Fig. 4-5(b)] is best fit by no [100] lattice deformation (0.00 ± 0.08%), an isotropic expansion of 0.16 ± 0.02%, and a reduced carrier density of 0.6 ± 0.1 × 10^{20} carriers/cm^3 accounting for Auger recombination. A lattice thermalization accurately predicts the long-time scale increase (decrease) in absorption at energies

below (above) the dominant L_1 absorption peak. The increase in absorption around the Δ_1 critical point feature as well as the appearance of an L_3 critical point feature with increasing time delay are also accurately predicted.

Following the previous electron and x-ray diffraction measurements, the magnitude of the expected thermal lattice expansion can be estimated by summing over the effective Grüneisen parameters for the excited phonon modes in Eqs. (4.11) and (4.12).[24,92,101] Using $\Delta N_k E_k = C_k \Delta T_k$ and summing over all involved phonon modes gives an isotropic stress of

$$\sigma_{Th} = -\sum_k \Delta N_k E_k \gamma_k = \gamma_k C_k(T) \Delta T = 3B\beta_v(T)\Delta T, \tag{4.13}$$

where $\beta_v(T) \sim 3 \times 10^{-6}$ K^{-1} is the linear thermal expansion coefficient,[102] B is the bulk modulus, ΔT is the temperature change due to the thermalization of the photoexcited carrier density ΔN, $C_v(T)$ is the heat capacity per unit volume of the involved phonon modes, and γ_v is the sum over the relevant Grüneisen parameters.[103,104] The change in lattice temperature, ΔT, is estimated by

$$\Delta T = \Delta \mathrm{N} \frac{\hbar\omega}{C_v(T)}, \tag{4.14}$$

where ΔN is the excited carrier density, $\hbar\omega$ is the pump photon energy, and $C_v(T)$ is the heat capacity per unit volume, here calculated within the Debye model using a Debye temperature of 645 K.[103] At the carrier densities used, VB-CB Auger recombination is also significant on this time scale. During Auger recombination, already thermalized carriers are given additional energy by the three-body scattering process. This excess energy must be re-thermalized, leading to an additional heating of the lattice by 40–50 K on a 200 ps timescale.

Including the heating from re-thermalized VB-CB Auger excited carriers, Eqs. (4.13)–(4.15) predict a 0.06%-0.08% isotropic lattice expansion. The 0.1%–0.2% thermal expansion range from the best fit is larger than the expansion predicted using Eq. (4.13) by a factor of 2. The disagreement is most likely because of the equilibrium-approximation of Eq. (4.13), but may also originate in the ultra-thin membrane geometry of the experiment, which has been reported to increase the actual thermal stress by 2–3 times.[11,97,105] It should also be noted that an isotropic lattice contraction is not observed as previously reported. The strength of the isotropic deformation is given by $\eta = d_{eh}\Delta$N, where $d_{eh} = -1 \times 10^{-24}$ cm^3.[22,106] For the experimental conditions here, this predicts an isotropic contraction that is 1/10th the strength of the predicted thermal expansion, explaining the absence of this effect.

4.3.4 Quantifying Carrier and Phonon Dynamics

The results of Fig. 4-5 suggest that the modeled electronic and structural effects describe the excited state XUV spectrum within the 0.2 eV experimental spectral resolution and 5 mOD experimental noise limit of the data at three key time scales. The fit procedure can equally be used to quantify the carrier density, lattice deformation, and lattice expansion for all times following 800 nm photoexcitation (Fig. 4-6). The fit procedure should allow the kinetics of the photoexcited electrons, optical phonons, and acoustic phonons to be extracted accurately from the experimental XUV differential absorption. To validate that the fit kinetics match the previously measured kinetics of photoexcited silicon, the experimental fit values are compared to a three-temperature

model (3TM) in Fig. 4-6. [8,10,107–112] The solid lines show the 3TM predictions. The points refer to the experimentally extracted quantities, with error bars representing the standard error of the fit.

The 3TM is used to check the fit because it predicts the population averaged kinetics of the electrons, optical phonons, and acoustic phonons in photo-excited silicon, as well as the effects of thermal and carrier diffusion, Auger recombination, and the spatial dependence of the excited carrier distribution.[8,10,107–112] The 3TM is given as[108]

$$C_e \frac{\partial T_e}{\partial t} = \frac{D_a T_e}{n_e} \frac{\partial n_e}{\partial z} \frac{\partial T_e}{\partial z} - \frac{C_e}{\tau_{eo}} (T_e - T_o) - \frac{C_e}{\tau_{ea}} (T_e - T_a) + E_g \frac{n_e}{\tau_{Aug}(n_e)} + \left(\hbar\omega - E_g\right) * S(t,z), \tag{4.15}$$

$$C_o \frac{\partial T_o}{\partial t} = \frac{C_e}{\tau_{eo}} (T_e - T_o) - \frac{C_o}{\tau_{oa}} (T_o - T_a), \tag{4.16}$$

$$C_a \frac{\partial T_a}{\partial t} = \frac{\partial}{\partial z}\left(C_a D_t \frac{\partial T_e}{\partial z}\right) + \frac{C_e}{\tau_{eo}} (T_e - T_a) - \frac{C_o}{\tau_{oa}} (T_o - T_a), \tag{4.17}$$

$$\frac{\partial n_e}{\partial t} = \frac{\partial}{\partial z}\left(D_a \frac{\partial n_e}{\partial z}\right) - \frac{n_e}{\tau_{Aug}(n_e)} + S(t,z). \tag{4.18}$$

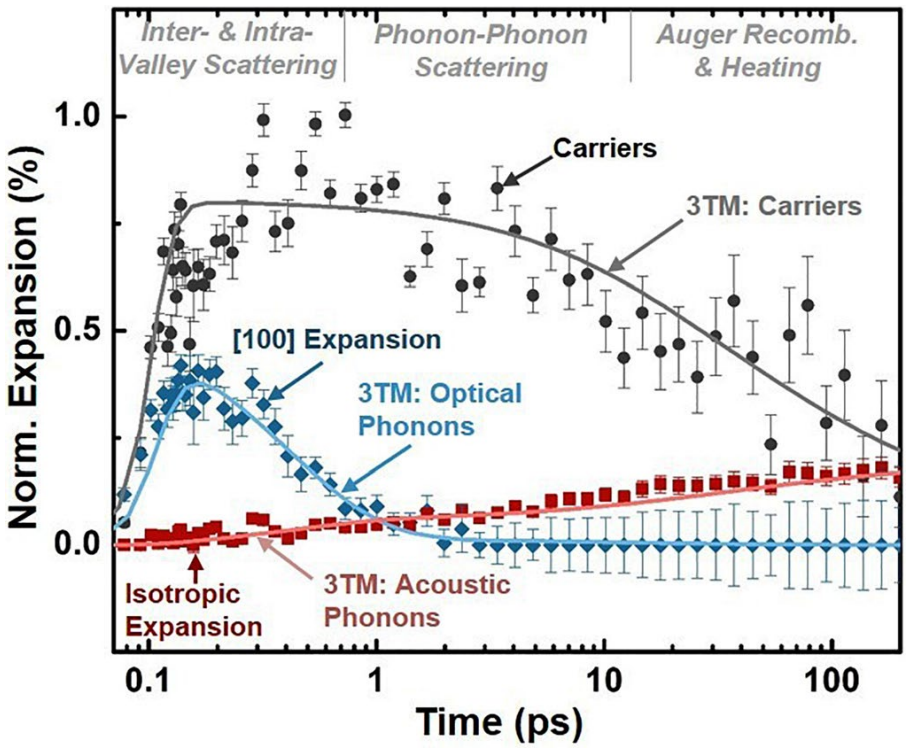

Figure 4-6: Time dependent carrier density, lattice deformation, and thermal lattice expansion as extracted from a non-linear fit of the measured excited state XUV absorption. The solid lines show the predictions of a three-temperature model (3TM) for the carrier density, optical phonons, and acoustic phonons. The points refer to the quantities extracted from the experimental data, with error bars representing the standard error of the fit to the experimental data. The non-linear fit is weighted by the experimental uncertainty. The scatter of the points is representative of the experimental noise. The lattice deformation is approximated as an equilibrium [100] expansion and the lattice heating is approximated as an isotropic lattice expansion. The log scale of time is offset by 100 fs for visualization.

In Eqs. (4.16)–(4.18), C_i and T_i refer to the heat capacity per unit volume and temperature, respectively, of the electron (e), optical phonon (o), and acoustic phonon (a) baths. The temperatures of the electron and optical-phonon baths represent non-equilibrium temperatures of the excited state populations, not to be confused with the equilibrated lattice temperature. The electron-phonon and phonon-phonon coupling times between these baths are τ_{ea}, τ_{eo}, and τ_{oa}. The electronic heat capacity is treated according to Ref. 112, but it can be approximated as $\frac{3}{2}k_b n_e$, where k_b is the Boltzmann constant. The temperature dependent heat capacity of the optical phonon modes is approximated by an Einstein model with an energy of 60 meV.[113] The temperature dependent heat capacity of the acoustic phonons is approximated using a Debye model with a Debye temperature of 645 K.103 D_a and D_t refer to the ambipolar electronic and thermal diffusion constants, taken as 15 cm^2/s and 0.88 cm^2/s from Refs. 114 and 115. D_a is approximated as a constant over the range of carrier densities present on the timescale of these experiments. n_e is the spatially dependent carrier density created by the source term $S(t,z)$ which has a spatial and temporal profile matching the absorption depth of the excitation wavelength ($\hbar\omega$) in silicon ($E_g = 1.12$ eV) and the pulse parameters reported in the Methods.

Using $(\hbar\omega - E_g) * S(t,x)$ as the source term of the 3TM implies that the kinetics are modeled only for thermalization to the band edge. If longer time scales are modeled up to when non-radiative recombination is present, Eq. (4.15) should be $(\hbar\omega) * S(t,x)$ to imply that all photoexcited energy goes into heating the lattice and a non-radiative heating term should be included in Eq. (4.17). Hot phonon bottleneck effects were not measured, so the optical and electronic temperatures are allowed to return to equilibrium independent of the acoustic phonon bath temperature. The Auger recombination time (τ_{Aug}) is parameterized by the Richter model.[116] Impact ionization was tested for using the parameterization of Ref. 112, but was not found to have a significant effect within the experimental noise limit of 5 mOD. Since the absorption depth and membrane thickness are smaller than the illuminated area, the spatial carrier and heating dynamics can be treated as one-dimensional.[24] Given that the thin silicon membrane is in vacuum and only radiative cooling is possible, the heat and carrier flux are treated as zero at both boundaries. The results from the 3TM are averaged over the XUV probe depth in the sample for comparison to experiment.

The 3TM prediction shown in Fig. 4-6 uses an excitation density of 1.5×10^{20} cm^{-3} and scattering times of τ_{eo}, τ_{ea}, and τ_{oa} equal to 30 fs, 500 fs, and 400 fs. These times are consistent with silicon's inter-valley scattering time of 20–60 fs,[82,83] electron-acoustic phonon scattering time of 500 fs,[107] and the 400 fs screened optical phonon lifetime at 10^{20} carriers/cm^3 excitation.[117] An inter-valley scattering time of 20–40 fs can reproduce the experimental rise time since the optical-phonon scattering time is within the excitation pulse width. The predicted carrier density from the 3TM rapidly rises within the pulse duration and then decays on a few ps time-scale due to Auger recombination, in agreement with the experimentally fit carrier density. For 800 nm excitation, the [100] wave-vector optical phonons take part in inter-valley and not intra-valley scattering.[6,84,85] Accordingly, the experimentally fit [100] lattice deformation mirrors the optical phonon kinetics predicted from the 3TM. The longer time scale isotropic lattice expansion kinetics are also accurately predicted by the lattice temperature from the 3TM.

The 3TM relates the average of the carrier and phonon scattering pathways between the initially excited carrier distribution and the final lattice temperature. The agreement between the fitted kinetics and the 3TM in Fig. 4-6 therefore suggests that the XUV spectrum can be used to quantify the average inter-valley, intra-valley, and phonon-phonon scattering in relation to the carrier density. Of course, it must be remembered that the 3TM only represents the previously measured kinetics in silicon, and is an approximate treatment of the momentum-dependent nonequilibrium carrier and phonon populations present after excitation.

4.4 Conclusions

In conclusion, the transient XUV signal of the silicon $2p$ $L_{2,3}$ edge was analyzed in terms of possible electronic and structural changes following excitation in the Δ valley. The initially excited carrier distribution leads to state-filling, broadening, and band-gap renormalization. In the silicon XUV spectrum, the broadening induced changes are strongest, masking the state-filling, while the band-gap renormalization is offset by the core-hole exciton. On time scales up to a few picoseconds, an anisotropic lattice deformation dominates the structural contributions to the differential spectrum. This deformation initiates and decays on the timescale of excited optical phonon modes, matching the inter-valley thermalization kinetics of carriers following 800 nm

excitation. On longer time scales, an isotropic lattice expansion corresponding to a lattice heating dominates the structural contributions to the differential XUV absorption. The kinetics of the lattice expansion match those of acoustic phonons involved in intra-valley thermalization and phonon-phonon scattering on a tens of picoseconds timescale. At >10 ps timescales, Auger recombination decreases the excited carrier density, decreasing the electronic contributions to the differential absorption but also further heating the lattice. By approximating these effects to first order using the BSE-DFT calculations of the ground state XUV absorption, the carrier and phonon dynamics following photoexcitation were quantified using a best-fit procedure. The fit kinetics agree well with previously measured photoexcited kinetics of silicon using a visible light probe. These experiments suggest that when the experimental XUV absorption can be accurately modeled in terms of the ground state properties of the material, transient XUV has potential for single-instrument determination of carrier and phonon scattering pathways in semiconductors.

4.4 Bibliography

1. Pop, E. Energy dissipation and transport in nanoscale devices. *Nano Res.* **3**, 147 (2010).

2. Minnich, A. J., Dresselhaus, M. S., Ren, Z. F. & Chen, G. Bulk nanostructured thermoelectric materials: Current research and future prospects. *Energy Environ. Sci.* **2**, 466 (2009).

3. Knig, D. *et al.* Hot carrier solar cells: Principles, materials and design. *Phys. E Low-Dimensional Syst. Nanostructures* **42**, 2862 (2010).

4. Shah, J. *Ultrafast Spectroscopy of Semiconductors and Semiconductor Nanostructures*. (Springer, 1999).

5. C. V. Shank, B. P. Z. *Spectroscopy of Nonequilibrium Electrons and Phonons*. (1992).

6. Reggiani, L. *Hot-Electron Transport in Semiconductors*. (Springer, 2014).

7. M. V. Fischetti, S. E. Laux, E. C. in *Hot Carriers in Semiconductors*. (ed. K. Hess, J.-P. Leburton, U. R.) 475 (Springer, 1996).

8. Waldecker, L., Bertoni, R., Ernstorfer, R. & Vorberger, J. Electron-phonon coupling and energy flow in a simple metal beyond the two-temperature approximation. *Phys. Rev. X* **6**, 021003 (2016).

9. Lindenberg, A. M. *et al.* Time-resolved X-ray diffraction from coherent phonons during a laser-induced phase transition. *Phys. Rev. Lett.* **84**, 111(2000).

10. Krasniqi, F. S. *et al.* Influence of lattice heating time on femtosecond laser-induced strain waves in InSb. *Phys. Rev. B - Condens. Matter Mater. Phys.* **78**, 174302 (2008).

11. Harb, M. *et al.* Excitation of longitudinal and transverse coherent acoustic phonons in nanometer free-standing films of (001) Si. *Phys. Rev. B - Condens. Matter Mater. Phys.* **79**, 094301 (2009).

12. Buschert, J. R., Colella, R., Lafayette, W. & Depart-, P. Photostriction Effect In Silicon Observed by Time-Resolved X-Ray Diffraction. **80**, 419 (1991).

13. Harb, M. *et al.* Carrier relaxation and lattice heating dynamics in silicon revealed by femtosecond electron diffraction. *J. Phys. Chem. B* **110**, 25308 (2006).

14. Harb, M. *et al.* Electronically driven structure changes of Si captured by femtosecond electron diffraction. *Phys. Rev. Lett.* **100**, 155504 (2008).

15. P. Stampfli, K. H. B. Time Dependence of the laser-induced femtosecond lattice instability of Si and GaAs: Role of Longitudinal Optical Distortions. *Phys. Rev. B* **49**, 7299 (1994).

16. Medvedev, N., Li, Z. & Ziaja, B. Thermal and nonthermal melting of silicon under femtosecond x-ray irradiation. *Phys. Rev. B - Condens. Matter Mater. Phys.* **91**, 054113 (2015).

17. Zier, T., Zijlstra, E. S., Kalitsov, A., Theodonis, I. & Garcia, M. E. Signatures of nonthermal melting. *Struct. Dyn.* **2**, 054101 (2015).

18. Zier, T., Zijlstra, E. S. & Garcia, M. E. Quasimomentum-space image for ultrafast melting of silicon. *Phys. Rev. Lett.* **116**, 153901 (2016).

19. Lian, C., Zhang, S. B. & Meng, S. Ab initio evidence for nonthermal characteristics in ultrafast laser melting. *Phys. Rev. B* **94**, 184310 (2016).

20. Ionin, A. A. *et al.* Preablation electron and lattice dynamics on the silicon surface excited by a femtosecond laser pulse. *J. Exp. Theor. Phys.* **121**, 737 (2015).

21. Stampfli, P. & Bennemann, K. H. Dynamical theory of the laser-induced lattice instability of silicon. *Phys. Rev. B* **46**, 10686 (1992).

22. W. B. Gauster, D. H. H. Electronic Volume Effect in Silicon. *Phys. Rev. Lett.* **18**, 1058 (1967).

23. Wright, O. B., Matsuda, O., Perrin, B. & Gusev, V. E. Ultrafast carrier diffusion in gallium arsenide probed with picosecond acoustic pulses. *Phys. Rev. B - Condens. Matter Mater. Phys.* **64**, 081202 (2001).

24. C. Thomsen, H. T. Grahn, H. J. Maris, J. T. Surface Generation and Detection of Phonons by Picosecond Light Pulses. *Phys. Rev. B* **34**, 4129 (1986).

25. Pezeril, T. *et al.* Generation and detection of plane coherent shear picosecond acoustic pulses by lasers: Experiment and theory. *Phys. Rev. B - Condens. Matter Mater. Phys.* **75**, 174307 (2007).

26. Matsuda, O., Wright, O. B., Hurley, D. H., Gusev, V. E. & Shimizu, K. Coherent shear phonon generation and detection with ultrashort optical pulses. *Phys. Rev. Lett.* **93**, 095501 (2004).

27. Hase, M., Kitajima, M. & Constantinescu, A. M. 2003 The birth of a quasiparticle in silicon observed in time–frequency space.pdf. **128**, 51 (2003).

28. Ishioka, K., Rustagi, A., Höfer, U., Petek, H. & Stanton, C. J. Intrinsic coherent acoustic phonons in the indirect band gap semiconductors Si and GaP. *Phys. Rev. B* **95**, 035205 (2017).

29. Öström, H. *et al.* Probing the transition state region in catalytic CO oxidation on Ru. *Science.* **347**, 978 (2015).

30. Katz, J. E. *et al.* Electron Small Polarons and Their Mobility in Iron (Oxyhydr)oxide Nanoparticles. *Science.* **337**, 1200 (2012).

31. Kachel, T. *et al.* Transient electronic and magnetic structures of nickel heated by ultrafast laser pulses. *Phys. Rev. B - Condens. Matter Mater. Phys.* **80**, 092404 (2009).

32. Brabec, T. & Krausz, F. Intense Few-Cycle Laser Fields: Frontiers of Nonlinear Optics. **72**, 545 (2000).

33. Chen, L. X. & Zhang, X. Photochemical Processes Revealed by X-ray Transient Absorption Spectroscopy. *J. Phys. Chem. Lett.* **4**, 4000 (2013).

34. Chen, L. X. in *X-Ray Absorption and X-Ray Emission Spectroscopy*. (ed. J. A. V. Bokhoven, C. L.) 213 (John Wiley & Sons, Ltd, 2016).

35. De Groot, F. & Kotani, A. *Core level spectroscopy of solids*. (CRC Press, Florida, 2008).

36. Weng, X., Rez, P., Batson, P. E. & Heights, Y. Single Electron Calculations for the Si L2,3 Near Edge Structure. *Solid State Commun.* **74**, 1013 (1990).

37. Weijs, P. J. W. *et al.* Core-hole effects in the x-ray-absorption spectra of transition-metal silicides. *Phys. Rev. B* **41**, 11899 (1990).

38. Goulielmakis, E. *et al.* Real-time observation of valence electron motion. *Nature* **466**, 739 (2010).

39. Hosler, E. R. & Leone, S. R. Characterization of vibrational wave packets by core-level high-harmonic transient absorption spectroscopy. *Phys. Rev. A - At. Mol. Opt. Phys.* **88**, 023420 (2013).

40. Krüger, P. Multichannel multiple scattering calculation of L2,3 -edge spectra of TiO2 and SrTiO3: Importance of multiplet coupling and band structure. *Phys. Rev. B - Condens. Matter Mater. Phys.* **81**, 125121 (2010).

41. Campbell, L., Hedin, L., Rehr, J. J. & Bardyszewski, W. Interference between extrinsic and intrinsic losses in x-ray absorption fine structure. *Phys. Rev. B - Condens. Matter Mater. Phys.* **65**, 0641071 (2002).

42. Rehr, J. J. Failure of the quasiparticle picture of x-ray absorption? *Found. Phys.* **33**, 1735 (2003).

43. Zhang, Q. *et al.* Suppression of driving laser in high harmonic generation with a microchannel plate. *Opt. Lett.* **39**, 3670 (2014).

44. Asche, M. & Sarbei, O. G. Electron–Phonon Interaction in n-Si. *Phys. Status Solidi* **103**, 11 (1981).

45. Green, M. A. Self-consistent optical parameters of intrinsic silicon at 300 K including temperature coefficients. *Sol. Energy Mater. Sol. Cells* **92**, 1305 (2008).

46. Sokolowski-Tinten, K. & von der Linde, D. Generation of dense electron-hole plasmas in

silicon. *Phys. Rev. B - Condens. Matter Mater. Phys.* **61**, 2643 (2000).

47. Sjodin, T., Petek, H. & Dai, H. Ultrafast Carrier Dynamics in Silicon: A Two-Color Transient Reflection Grating Study on a (111) Surface. *Phys. Rev. Lett.* **81**, 5664 (1998).

48. Bristow, A. D., Rotenberg, N. & Van Driel, H. M. Two-photon absorption and Kerr coefficients of silicon for 850-2200 nm. *Appl. Phys. Lett.* **90**, 191104 (2007).

49. Cheng, J. L., Rioux, J. & Sipe, J. E. Full band structure calculation of two-photon indirect absorption in bulk silicon. *Appl. Phys. Lett.* **98**, 131101 (2011).

50. Vinson, J., Rehr, J. J., Kas, J. J. & Shirley, E. L. Bethe-Salpeter equation calculations of core excitation spectra. *Phys. Rev. B - Condens. Matter Mater. Phys.* **83**, 115106 (2011).

51. Gilmore, K. *et al.* Efficient implementation of core-excitation Bethe-Salpeter equation calculations. *Comput. Phys. Commun.* **197**, 109 (2015).

52. Giannozzi, P. *et al.* QUANTUM ESPRESSO: A modular and open-source software project for quantum simulations of materials. *J. Phys. Condens. Matter* **21**, 395502 (2009).

53. Shirley, E. L. Local screening of a core hole: A real-space approach applied to hafnium oxide. *Ultramicroscopy* **106**, 986 (2006).

54. Z. H. Levine, S. G. L. New Model Dielectric and Exchange-Correlation Potential for Semiconductors and Insulators. *Phys. Rev. B* **25**, 6310 (1982).

55. Müller, J. E., Jepsen, O. & Wilkins, J. W. X-ray absorption spectra: K-edges of 3d transition metals, L-edges of 3d and 4d metals, and M-edges of palladium. *Solid State Commun.* **42**, 365 (1982).

56. Bunău, O. & Joly, Y. Self-consistent aspects of x-ray absorption calculations. *J. Phys. Condens. Matter* **21**, 345501 (2009).

57. Klementev, K. V. Deconvolution problems in x-ray absorption fine structure spectroscopy. *J. Phys. D. Appl. Phys.* **34**, 2241 (2001).

58. Kas, J. J. *et al.* Many-pole model of inelastic losses in x-ray absorption spectra. *Phys. Rev. B - Condens. Matter Mater. Phys.* **76**, 195116 (2007).

59. G. G. Fuentes, E. Elizalde, F. Yubero, J. M. S. Electron inelastic mean free path for Ti, TiC, TiN and TiO2 as determined by quantitative reflection electron energy-loss spectroscopy. *Surf. Interface Anal.* **33**, 230 (2002).

60. Bourke, J. D. & Chantler, C. T. Momentum-dependent lifetime broadening of electron energy loss spectra: A self-consistent coupled-plasmon model. *J. Phys. Chem. Lett.* **6**, 314 (2015).

61. Chantler, C. T. & Bourke, J. D. Momentum-dependent lifetime broadening of electron

energy loss spectra: Sum rule constraints and an asymmetric rectangle toy model. *Phys. Rev. B - Condens. Matter Mater. Phys.* **90**, 174306 (2014).

62. Yubero, F., Tougaard, S., Elizalde, E. & Sanz, J. M. Dielectric loss function of Si and SiO2 from quantitative analysis of REELS spectra. *Surf. Interface Anal.* **20**, 719 (1993).

63. Ding, Z. J. Self-energy in surface electron spectroscopy: I. Plasmons on a free-electron-material surface. *J. Phys. Condens. Matter* **10**, 1733 (1998).

64. Krause, M. O. & Oliver, J. H. Natural widths of atomic K and L levels, Kα X-ray lines and several KLL Auger lines. *J. Phys. Chem. Ref. Data* **8**, 329 (1979).

65. Bennett, B. R., Soref, R. A. & Del Alamo, J. A. Carrier-Induced Change in Refractive Index of InP, GaAs, and InGaAsP. *IEEE J. Quantum Electron.* **26**, 113 (1990).

66. B. L. Henke, E. M. Gullikson, J. C. D. X-Ray Interactions: Photoabsorption, Scattering, Transmission, and Reflection at E = 50-30,000, Z = 1-92. *At. Data Nucl. Data Tables* **54**, 181 (1993).

67. Sangalli, D., Dal Conte, S., Manzoni, C., Cerullo, G. & Marini, A. Nonequilibrium optical properties in semiconductors from first principles: A combined theoretical and experimental study of bulk silicon. *Phys. Rev. B* **93**, 195205 (2016).

68. Wolff, P. A. Theory of the Band Structure of Very Degenerate Semiconductors. *Phys. Rev.* **126**, 405 (1962).

69. Berggren, K. F. & Sernelius, B. E. Band-gap narrowing in heavily doped many-valley semiconductors. *Phys. Rev. B* **24**, 1971 (1981).

70. A. Abram, G. N. Childs, P. A. S. Band gap narrowing due to many-body effects in silicon and gallium arsenide and gallium arsenide. *J. Phys. C Solid State Phys.* **17**, 6105 (1984).

71. Oschlies, A., Godby, R. W. & Needs, R. J. GW self-energy calculations of carrier-induced band-gap narrowing in n-type silicon. *Phys. Rev. B* **51**, 1527 (1995).

72. Larson, P., Dvorak, M. & Wu, Z. Role of the plasmon-pole model in the GW approximation. *Phys. Rev. B - Condens. Matter Mater. Phys.* **88**, 42 (2013).

73. Wagner, J. & Del Alamo, J. A. Band-gap narrowing in heavily doped silicon: A comparison of optical and electrical data. *J. Appl. Phys.* **63**, 425 (1988).

74. Feneberg, M. *et al.* Band gap renormalization and Burstein-Moss effect in silicon- and germanium-doped wurtzite GaN up to 1020 cm-3. *Phys. Rev. B - Condens. Matter Mater. Phys.* **90**, 075203 (2014).

75. Brown, F. C., Bachrach, R. Z. & Skibowski, M. L2,3 threshold spectra of doped silicon and silicon compounds. *Phys. Rev. B* **15**, 4781 (1977).

76. Schultze, M. *et al.* Attosecond Band-Gap Dynamics in Silicon. *Science* **346**, 1348 (2014).

77. Euaruksakul, C. *et al.* Influence of strain on the conduction band structure of strained silicon nanomembranes. *Phys. Rev. Lett.* **101**, 147403 (2008).

78. Harp, G. R., Han, Z. & Tonner, B. P. Spatially-Resolved X-Ray Absorption Near-Edge Spectroscopy of Silicon in Thin Silicon-Oxide Films. *Phys. Scr.* **31**, 23 (1990).

79. Rideau, D. *et al.* Strained Si, Ge, and Si1-x Gex alloys modeled with a first-principles-optimized full-zone kp method. *Phys. Rev. B - Condens. Matter Mater. Phys.* **74**, 195208 (2006).

80. Batson, P. E. Atomic and electronic structure of a dissociated 60° misfit dislocation in GexSi(1-x). *Phys. Rev. Lett.* **83**, 4409 (1999).

81. Euaruksakul, C. *et al.* Relationships between strain and band structure in Si(001) and Si(110) nanomembranes. *Phys. Rev. B - Condens. Matter Mater. Phys.* **80**, 115323 (2009).

82. J. R. Goldman, J. A. P. Ultrafast Dynamics of Laser-Excited Electron Distributions in Silicon. *Phys. Rev. Lett.* **72**, 1364 (1994).

83. Sabbah, A. J. & Riffe, D. M. Femtosecond pump-probe reflectivity study of silicon carrier dynamics. *Phys. Rev. B - Condens. Matter Mater. Phys.* **66**, 165217 (2002).

84. Long, D. Scattering of conduction electrons by lattice vibrations in silicon. *Phys. Rev.* **120**, 2024 (1960).

85. Lax, M. & Hopfield, J. J. Selection rules connecting different points in the brillouin zone. *Phys. Rev.* **124**, 115 (1961).

86. Doni, E. & Parravicini, G. P. Selection rules for indirect transitions and effect of time-reversal symmetry. II. Full-group procedure. *J. Phys. C Solid State Phys.* **7**, 1786 (1974).

87. Cheng, J. L., Rioux, J., Fabian, J. & Sipe, J. E. Theory of optical spin orientation in silicon. *Phys. Rev. B - Condens. Matter Mater. Phys.* **83**, 165211 (2011).

88. W. Eberhardt, F. J. H. Dipole Selection Rules for Optical Transitions in the fcc bcc Lattices. *Phys. Rev. B* **21**, 5572 (1980).

89. Sangalli, D. & Marini, A. Ultra-fast carriers relaxation in bulk silicon following photo-excitation with a short and polarized laser pulse. *Epl* **110**, 47004 (2015).

90. A. Smirl, T. Boggess, B. Wherrett, G. Perryman, A. M. Picosecond Transient Orientational Concentration Gratings in Germanium. *IEEE J. Quantum Electron.* **19**, 690 (1983).

91. J. L. Oudar, A. Migus, D. Hulin, G. Grillon, J. Etchepare, A. A. Femtosecond Orientational Relaxation of Photoexcited Carriers in GaAs. *Phys. Rev. Lett.* **53**, 384 (1984).

92. Ruello, P. & Gusev, V. E. Physical mechanisms of coherent acoustic phonons generation by ultrafast laser action. *Ultrasonics* **56**, 21 (2015).

93. Keyes, R. W. The electronic contribution to the elastic properties of germanium. *IBM J. Res. Dev.* **5**, 266 (1961).

94. Cerdeira, F. & Cardona, M. Effect of carrier concentration on the raman frequencies of Si and Ge. *Phys. Rev. B* **5**, 1440 (1972).

95. Fjeldly, T. A., Cerdeira, F. & Cardona, M. Effects of free carriers on zone-center vibrational modes in heavily doped p-type Si. I. Acoustical modes. *Phys. Rev. B* **8**, 4723 (1973).

96. Zollner, S., Gopalan, S. & Cardona, M. Short-range deformation-potential interaction and its application to ultrafast processes in semiconductors. *Semicond. Sci. Technol.* **7**, B137 (1992).

97. Larson, B. C., Tischler, J. Z. & Mills, D. M. Nanosecond resolution time-resolved x-ray study of silicon during pulsed-laser irradiation. *J. Mater. Res.* **1**, 144 (1986).

98. Hopcroft, M. A., Nix, W. D. & Kenny, T. W. What is the Young's modulus of silicon? *J. Microelectromechanical Syst.* **19**, 229 (2010).

99. Goroff, I. & Kleinman, L. Deformation potentials in silicon. III. Effects of a general strain on conduction and valence levels. *Phys. Rev.* **132**, 1080 (1963).

100. Nicoul, M., Shymanovich, U., Tarasevitch, A., Von Der Linde, D. & Sokolowski-Tinten, K. Picosecond acoustic response of a laser-heated gold-film studied with time-resolved x-ray diffraction. *Appl. Phys. Lett.* **98**, 2009 (2011).

101. Cardona, M. Electron-phonon interaction in tetrahedral semiconductors. *Solid State Commun.* **133**, 3 (2005).

102. Okada, Y. & Tokumaru, Y. Precise determination of lattice parameter and thermal expansion coefficient of silicon between 300 and 1500 K. *J. Appl. Phys.* **56**, 314 (1984).

103. O. Madelung, M. Schulz, U. R. *Group IV Elements, IV-IV and III-V Compounds. Part B-Electronic, Transport, Optical and Other Properties*. (Springer, 2002).

104. Wei, S., Li, C. & Chou, M. Y. Ab initio calculation of thermodynamic properties of silicon. *Phys. Rev. B* **50**, 14587 (1994).

105. Berry, B. S. & Pritchet, W. C. Stress and thermal expansion of boron-doped silicon membranes on silicon substrates. *J. Vac. Sci. Technol. A Vacuum, Surfaces Film.* **9**, 2231 (1991).

106. Gauster, W. B. Electronic Dilation in Germanium and Silicon. *Phys. Rev.* **187**, 1035 (1969).

107. Lee, S. H. Nonequilibrium heat transfer characteristics during ultrafast pulse laser heating of a silicon microstructure. *J. Mech. Sci. Technol.* **19**, 1378 (2005).

108. Shin, T., Teitelbaum, S. W., Wolfson, J., Kandyla, M. & Nelson, K. A. Extended two-temperature model for ultrafast thermal response of band gap materials upon impulsive optical

excitation. *J. Chem. Phys.* **143**, 194705 (2015).

109. Derrien, T. J. Y. *et al.* Rippled area formed by surface plasmon polaritons upon femtosecond laser double-pulse irradiation of silicon: the role of carrier generation and relaxation processes. *Opt. Express.* **21**, 29643 (2013).

110. Chen, J. K., Tzou, D. Y. & Beraun, J. E. A semiclassical two-temperature model for ultrafast laser heating. *Int. J. Heat Mass Transf.* **49**, 307 (2006).

111. Perner, M. *et al.* Observation of hot-electron pressure in the vibration dynamics of metal nanoparticles. *Phys. Rev. Lett.* **85**, 792 (2000).

112. Driel, H. M. Van. Kinetics of High-Density Plasmas Generated in Si by 1.06- and 0.53-um Picosecond Laser Pulses. **35**, 8166 (1987).

113. P. Giannozzi, S. de G. Ab initio calculation of phonon dispersions in semiconductors. *Phys. R* **43**, 7231 (1991).

114. Li, C. M., Sjodin, T. & Dai, H. L. Photoexcited carrier diffusion near a Si(111) surface: Non-negligible consequence of carrier-carrier scattering. *Phys. Rev. B - Condens. Matter Mater. Phys.* **56**, 15252 (1997).

115. H. R. Shanks, P. D. Maycock, P. H. Sidles, G. C. D. Thermal Conductivity of Silicon from 300 to 1400 K. *Phys. Rev.* **130**, 1743 (1963).

116. Richter, A., Glunz, S. W., Werner, F., Schmidt, J. & Cuevas, A. Improved quantitative description of Auger recombination in crystalline silicon. *Phys. Rev. B - Condens. Matter Mater. Phys.* **86**, 165202 (2012).

117. Letcher, J. J., Kang, K., Cahill, D. G. & Dlott, D. D. Effects of high carrier densities on phonon and carrier lifetimes in Si by time-resolved anti-Stokes Raman scattering. *Appl. Phys. Lett.* **90**, 252104 (2007).